

University of Warwick institutional repository: <http://go.warwick.ac.uk/wrap>

A Thesis Submitted for the Degree of PhD at the University of Warwick

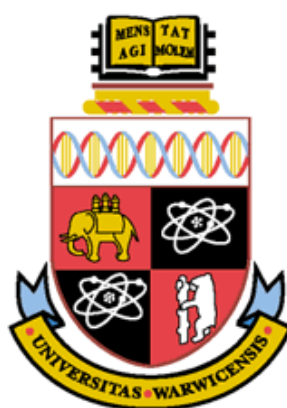
<http://go.warwick.ac.uk/wrap/3735>

This thesis is made available online and is protected by original copyright.

Please scroll down to view the document itself.

Please refer to the repository record for this item for information to help you to cite it. Our policy information is available from the repository home page.

Towards Understanding the Photochemistry of Tyrosine



Azhar Iqbal

Submitted for the Qualification of Doctor of Philosophy

University of Warwick

Department of Chemistry

June 2010

Contents

Contents page -----	2
List of abbreviations -----	8
List of Figures -----	11
List of Tables -----	19
Acknowledgments -----	20
Declaration -----	21
Publications -----	22
Abstract -----	23
1. Introduction -----	25
1.1. Brief History Chemical Reaction Dynamics.....	26
1.1.1. The Arrhenius Concept of Reaction Dynamics.....	26
1.1.2. London, Eyring and Polanyi’s Reaction Dynamics.....	28
1.2. Photochemistry and Reaction Dynamics.....	29
1.2.1. Construction of Potential Energy Surfaces.....	29
1.2.2. Photophysical and Photochemical Processes.....	33
1.2.2.1. Phosphorescence and Intersystem Crossing.....	34
1.2.2.2. Fluorescence and its Timescales.....	36
1.2.2.3. Quenching of Fluorescence.....	38
1.2.2.4. Internal Conversion and Predissociation.....	39
1.2.2.5. Non-Crossing Rule, Adiabatic and Non-adiabatic PES.....	41
1.2.2.6. Conical Intersections.....	44
1.2.2.7. Franck-Condon Principle.....	46

1.3. Femtochemistry.....	49
1.3.1. Time-energy Uncertainty Principle.....	51
1.3.2. The Chemical Change and its Timescales.....	52
1.3.3. Ti:apphire Lasers.....	56
1.4. Gas-phase Photodissociation Dynamics.....	57
1.5. Techniques to Study Gas-phase Dynamics.....	58
1.5.1. Molecular Beams.....	59
1.5.2. Laser Induced Fluorescence.....	61
1.5.3. Photoelectron Spectroscopy.....	62
1.5.4. Resonance Enhanced Multiphoton Ionization.....	63
1.5.4.1. Photofragment Translational Spectroscopy.....	66
1.5.4.2. Multi-mass Ion Imaging.....	67
1.6. Spectral Broadening.....	68
1.6.1. Doppler Broadening.....	69
1.6.2. Lifetime Broadening.....	69
1.7. Photostability of Aromatic Amino Acids and Gas-phase Photodissociation Dynamics.....	71
1.7.1. Gas-phase Photodynamics of Chromophores.....	72
1.7.2 Gas-phase Photodynamics of Tyrosine and its Sub-units.....	74
1.8. Aims and Outlines.....	75
1.9. References.....	77
2. Experimental Techniques-----	84
2.1. Pump-probe Setup.....	84
2.1.1. Generation of Pump and Probe Pulses.....	86

2.1.2. Nonlinear Optical Harmonics Generation.....	87
2.1.3. Temporal Overlap of Pump-probe Pulses.....	90
2.2. Vacuum Chamber.....	91
2.2.1. Even-Lavie Valve and Molecular Beam.....	93
2.2.1.1. Molecular Beam of Phenol, Indole and p-Ethylphenol.....	94
2.2.1.2. Molecular Beam of Tyramine.....	96
2.2.1.3. Molecular Beam of Tyrosine.....	97
2.3. Time-of-flight Mass Spectroscopy.....	99
2.3.1. Calibration of Time-of-flight Mass Spectrum.....	100
2.4. Instrument Response Function and Time Zero.....	102
2.4.1. Fitting the H ⁺ Transient.....	105
2.4.2. Fitting the Parent Ion Transient.....	107
2.5. Velocity Map Ion Imaging.....	108
2.5.1. Anisotropy Measurement of Photo-products.....	111
2.5.2. Time-resolved VMI of H ⁺ Ions.....	113
2.5.3. Calibration of Velocity Map Ion Imaging.....	116
2.5.4. Image Processing.....	119
2.6. References.....	121
 3. Direct versus Indirect H-atom Elimination from Photoexcited Phenol	
Molecules -----	123
3.1. Prologue.....	124
3.1.1. Potential Energy Profiles along the O-H Coordinate of Phenol.....	124
3.1.2. H-atom Transfer in Phenol-ammonia Clusters.....	126
3.1.3. H-atom Elimination Measurements in Phenol.....	126

3.1.4. Time-resolved H-atom Elimination Studies.....	127
3.2. The Experiment.....	128
3.3. Time-of-flight Mass-spectrum.....	130
3.4. H-atom Elimination via the $^1\pi\sigma^*$ State.....	132
3.4.1. Direct Pathway of H-atom Elimination.....	133
3.4.2. Indirect H-atom Elimination.....	135
3.4.2.1. Discussion.....	135
3.5. Dynamics of Parent Phenol Molecules.....	138
3.6. Epilogue.....	141
3.7. References.....	142
4. Exploring the Timescales of H-atom Detachment from Photoexcited	
Phenol-h6 and Phenol-d5: Statistical vs Nonstatistical Decay-----	144
4.1. Prologue.....	145
4.1.1. Disentangling Statistical and Nonstatistical Relaxation Routes.....	146
4.1.2. Multimass Ion-imaging of H-atoms.....	147
4.1.3. Total Kinetic Energy Released by H-atoms.....	147
4.1.4. H-atom Elimination in an Energy and Time-resolved Fashion.....	148
4.2. The Experiment.....	149
4.3. The Raw Images of H^+	150
4.3.1. Kinetic Energy Spectrum of H-atoms.....	152
4.3.2. Timescales of O-H Bond Photolysis in Phenol-d5.....	156
4.3.3. Anisotropy displayed by H-atoms.....	159
4.3.3.1. Discussion.....	161
4.4. Epilogue.....	165

4.5. References.....	168
5. Exploring the Timescales of H-atom Elimination from Photoexcited	
Indole -----	171
5.1. Prologue.....	172
5.1.1. Potential Energy Profiles of Indole along N-H Coordinate.....	172
5.1.2. Photoinduced N-H Bond Cleavage in Indole and its Timescales.....	174
5.1.3. A Brief Overview of N-H bond Dissociation Dynamics in Indole.....	175
5.2. The Experiment.....	177
5.3. Time-of-flight Mass Spectrum.....	178
5.4. The Raw Images of H ⁺ After N-H Bond Cleavage.....	179
5.4.1. Kinetic Energy Spectrum of H-atoms.....	182
5.4.2. Timescales of N-H Bond Photolysis.....	183
5.4.2.1. Discussion.....	186
5.5. Epilogue.....	189
5.6. References.....	190
6. Active Participation of ¹πσ* States in the Photodissociation of Tyrosine	
and Sub-units -----	193
6.1. Prologue.....	194
6.1.1. Fluorescence Quantum Yields of Tyrosine and its Chromophore.....	195
6.1.2. Substituted and Unsubstituted Phenols and O-H Bond Photolysis.....	196
6.1.3. H-atom Abstraction via the O-H Coordinate.....	196
6.2. The Experiment.....	197
6.3. Time-of-flight Mass Spectrum of Tyramine and p-Ethylphenol.....	198
6.4. Time-of-flight Mass Spectrum of Tyrosine.....	200

Contents

6.5. Raw Images and Kinetic Energy Spectrum of H-atoms.....	201
6.5.1. Timescales of H-atom Elimination from p-Ethylphenol.....	203
6.5.2. Timescales of H-atom Elimination from Tyramine.....	205
6.5.3. Timescales of H-atom Elimination from Tyrosine.....	207
6.5.3.1. Discussion.....	209
6.6. Epilogue.....	212
6.7. References.....	213
7. Conclusions -----	215

List of Abbreviations

UV	Ultra-violet
fs	Femtosecond
ps	Picosecond
ns	Nanosecond
μ s	Microsecond
PES	Potential Energy Surface
PESs	Potential Energy Surfaces
CI	Conical Intersection
CIs	Conical Intersections
Ph	Phenol
PE	Potential Energy
H	Hydrogen
RRKM	Rice-Ramsperger-Kassel-Markus
LCAOs	Linear Combination of Atomic Orbitals
DFT	Density Functional Theory
IVR	Intramolecular Vibrational Energy Redistribution
IC	Internal Conversion
Ti:sapphire	Titanium Doped Sapphire
IRMPD	Infra-red Multiphoton Dissociation
LIF	Laser-induced Fluorescence
MPI	Multi-photon Ionization
ESHT	Excited State Hydrogen Transfer

List of Abbreviations

TKER	Total Kinetic Energy Release
REMPI	Resonance-enhanced Multiphoton Ionization
PTS	Photofragment Translational Spectroscopy
VUV	Vacuum Ultra-violet
2D	2-Dimensional
3D	3-Dimensional
POP	Polar Onion Peeling
CW	Continuous-wave
CCD	Charge-coupled Device
DS	Delay-stage
SHG	Second Harmonic Generation
THG	Third Harmonic Generation
FHG	Fourth Harmonic Generation
IR	Infrared
OPA	Optical Parametric Amplifier
BBO	Beta Barium Borate (β -BaB ₂ O ₄)
KDP	Potassium Dihydrogen Phosphate
MCP	Microchannel Plate Detector
VMI	Velocity Map Ion Imaging
TOF	Time-of-flight
TOF-MS	Time-of-flight Mass Spectroscopy
FWHM	Full Width Half Maximum
Tyr	Tyrosine
BMP	Bitmap

List of Abbreviations

DG	Delay Generator
GPIB	General Purpose Interface Bus
Phenol-h6	C ₆ H ₅ -OH
Phenol-d5	C ₆ D ₅ -OH
CI _{pref}	Prefulvenic Conical Intersection
B3LYP	Becke 3-Parameter (Exchange Functional) Lee, Yang and Parr
TDDFT	Time-dependent Density Functional Theory
CASSCF	Complete-active-space Self-consistent-field
CASPT2	Complete-active-space with Second-order Perturbation Theory

List of Figures

- 1.1** The schematic display of intersystem crossing and phosphorescence, where the excited singlet state mixes with an excited triplet state through spin-orbit coupling. The triplet state acts as a slowly radiating reservoir because the return to the ground state is spin forbidden.....**36**
- 1.2** Pictorial representation of fluorescence. Following absorption, the upper electronic state undergoes radiationless decay to its lowest vibrational level. A radiative transition then occurs from the upper electronic state to the lower electronic state.....**37**
- 1.3** Diagram representing the predissociation mechanism.....**40**
- 1.4** An avoided crossing between two diabatic functions ϕ_1 and ϕ_2**43**
- 1.5** Schematic representation of a conical intersection between two PESs.....**45**
- 1.6** Diagrammatic representation of the Franck-Condon principle showing the vibronic coupling between two states of a molecule.....**47**
- 1.7** Pictorial representation of the femtochemistry of the NaI reaction, adapted from Zewail et al.²⁵ The wavepacket created by the laser excitation on the NaI PES moves between the ionic surface and covalent surface, and the out-put signal exhibits oscillations, when the wavepacket switches between ionic and covalent surfaces (see text for details).....**51**
- 1.8** Pictorial representation of preparation of a localized vibrational state following excitation of a diatomic molecule using an ultrashort laser pulse...**55**
- 1.9** Pictorial representation of a continuous free-jet expansion from a nozzle. The zone of silence is the region of expansion where the Mach number (M) $\gg 1$

and this is the collision free region. The regions where $M < 1$ are not collision free, the blue lines are the outer limits of zone of silence and separate this region from the barrel-shock region that contains pressure shock waves.....**61**

1.10 Pictorial representations of multiphoton ionization schemes.....**66**

1.11 Aromatic amino acids.....**72**

2.1 Schematic of laser setup (LHS) in conjunction with molecular beam (RHS). DS represents a motorised delay stage that moves to and fro as shown by double headed arrow to delay the probe beam with respect to the pump beam. SHG, THG and FHG represent the 2nd, 3rd and 4th harmonic generating crystals, respectively. The source and interaction chambers house the Even-Lavie valve and VMI setup (for illustration see figure 2.9) respectively.....**85**

2.2 (2 + 1) REMPI mechanism of H-atom. Two photons of 243.1 nm excites the H-atom to its 2s state and third photon ionizes it, thus generating H⁺ ion.¹...**86**

2.3 The vacuum chamber comprises of source and interaction chambers. The source chamber holds the Even-Lavie valve and the interaction chamber contains the TOF-MS and VMI setup. The MCP at the terminus of the flight tube can be replaced by the VMI detector (MCPs coupled with a phosphor screen) according to the measurements needed.....**93**

2.4 Measured pulse width ~60 μ s, with a backing pressure of 2 bar of He.....**94**

2.5 Pictorial presentations of (a) valve's cartridge assembly and (b) quartz pipette type tube to hold the tyramine sample.....**97**

2.6 Pictures of brass holder and borosilicate cell, (a) both brass holder and glass cell are attached in front of the valve nozzle (b) when both are demounted, (c)

- represents, the unused tyrosine sample and (d) shows the picture of used tyrosine sample.....**99**
- 2.7** TOF-MS setup. As the collinearly aligned laser beams intercept the molecular beam, ions are generated. The ions are then accelerated towards the detector.....**102**
- 2.8** (a) CH₃OH, (b) ¹²⁹Xe and (c) NH₃ ion signal as a function of pump-probe delay. The Gaussian fit to the CH₃OH and NH₃ ion signal suggest that the instrument response function is ~160 fs. A step in ¹²⁹Xe ion signal corresponds to a very long lived state.....**104**
- 2.9** VMI setup for H⁺ ion detection, indicating H⁺ ions (red circles) are generated between repeller and accelerator electrodes, are accelerated through the drift tube and then hit the MCP/phosphor screen (Green). Directly behind is a CCD camera that captures the fluorescence signal from the phosphor screen. The laser polarization is parallel to the plane of the detector.....**109**
- 2.10** Pictorial illustration of angular distribution of photo-products following absorption of linearly polarized light of electric field ϵ , for two extreme parallel and perpendicular transitions assuming very fast dissociation process.¹³**113**
- 2.11** A flow sheet diagrammatic representation of triggering scheme used to detect H⁺ ions during the experiments. Please note that two additional home-built digital delay generators are used in conjunction with the MCP's and deflector plates to generate the delays of 1.98ms (not shown).....**115**
- 2.12** Pictorial representation of the calibration of VMI, (a) represents the raw H⁺ image that is taken at a pump (200 nm)-probe (243.1 nm) delay of 2 ps, the

- bold double headed arrow gives the polarization of 200 nm that is parallel to the plane of the paper (b) gives the H^+ signal as a function of pixel radius (c) presents the H^+ signal as a function of kinetic energy and, (d) shows a plot of kinetic energy vs. pixel radius squared suggesting a calibration factor 0.4538 (see text for details).....**118**
- 2.13** Pictorial representation of photo-product of (a) Newton sphere $f(r, \theta, \Phi)$ displaying a cylindrical symmetry about the laser polarization z-axis, (b) 2D distribution $g(R, \alpha)$ produced by mapping onto xz-plane parallel to z-axis. Top figure gives conversion of a Cartesian pixel (square) into a polar pixel (tilted array).....**120**
- 3.1** Potential energy surfaces along R_{O-H} for the ground (S_0) and the first three excited singlet (two $^1\pi\pi^*$ and one $^1\pi\sigma^*$) states of phenol. These potential energy profiles are adapted from Ashfold et al.⁹ and redrawn for illustrative purposes.....**125**
- 3.2** One and two-colour mass spectra recorded with femtosecond laser-pulses at 200 nm (a) and 200 nm + 243.1 nm (b) respectively. The delay between 200 nm and 243.1 nm was fixed at 1.5 ps. The intensity of the 200 nm was reduced to avoid other fragmentation pathways.....**131**
- 3.3** Two-colour, multiphoton ionization of H-atoms as a function of wavelength. As the wavelength is tuned on resonance with the $2s \leftarrow 1s$ transition ($\lambda \sim 243$ nm) there is a considerable rise in the integrated H^+ signal as expected.....**133**

-
- 3.4** H^+ transient as a function of pump-probe delay. At negative time delays ($t < 0$), there is no appreciable H^+ signal. At positive delays, the H^+ signal rises sharply and plateaus beyond 400 fs.....**134**
- 3.5** H^+ signal versus extended pump-probe delays.....**135**
- 3.6** Excitation of phenol molecules at different wavelengths and probing with 800 nm. The time constants are extracted with the help of black solid line that is the best fit to the experimental data (blue circles) and is obtained by convolution of a Gaussian of 160 fs FWHM with the sum of two single-exponential decay functions, as explained in chapter 2. On the right hand side of the figure the extracted lifetimes are presented along with excitation and probing wavelengths.....**139**
- 3.7** Excited state dynamics of phenol exciting at 200 nm and probing with 243 nm.....**140**
- 4.1** Raw images for H^+ following photodissociation at 200 nm and probing with 243.1 nm. Only half of each image is shown for illustrative purposes where (a) and (b) correspond to phenol-h6 and phenol-d5, respectively. In both figures, the 243.1 nm probe was preceded by the pump by delay of 2 ps.....**151**
- 4.2** H^+ transient as a function of H-atom kinetic energy (dashed and solid lines correspond to pump-probe delays (t) of 0 and 2 ps respectively) for (a) Phenol-h6 and (b) Phenol-d5 molecules. At $t < 0$ there is no appreciable H^+ signal and therefore these transients are excluded for clarity.....**153**
-

-
- 4.3** H^+ transient as a function of H-atom kinetic energy. Dashed and solid lines correspond to a pump (200 nm) followed by a delayed probe (2 ps) centred at 238 nm and 243.1 nm respectively, (a) phenol-h6 and (b) phenol-d5 molecules. Note that the spectra recorded at 238 nm and 243.1 nm have not been normalized.....**155**
- 4.4** H^+ transients as a function of pump (200 nm)-probe (243.1 nm) delay for the low kinetic energy (a) and high kinetic energy (b) H-atoms in phenol-d5. At negative time delays ($t < 0$), there is no appreciable H^+ signal. At positive delays, the H^+ signal rises sharply and plateaus beyond 500 fs.....**157**
- 4.5** H^+ transient as a function of pump (200 nm)-probe (243.1 nm) at extended delays for phenol-d5. The black trace with circles indicates the integral at high kinetic energy maximum (11600 cm^{-1}) and the red trace with squares represents the integral at low kinetic energy maximum (2700 cm^{-1}).....**158**
- 4.6** Anisotropy parameter (β_2) as a function of kinetic energy of H-atom fragment. The pump (200 nm)-probe (243.1 nm) delay was set at 2 ps for these measurements. At the highest kinetic energies, $\beta_2 \approx 0.4$ while at lower kinetic energies, a positive, non-limiting β_2 still persists but with decreased signal-to-noise (see text for details).....**160**
- 5.1** Potential energy profiles of the lowest $^1\pi\pi^*$ (S_1), $^1\pi\sigma^*$ (S_2) and the electronic ground state (S_0) as a function of N-H stretch reaction coordinate of indole. These PESs have been adapted from Sobolewski et al.¹¹ and redrawn to scale for illustrative purposes.....**173**
-

5.2	One- and two-colour TOF-MS recorded at (a) pump (200 nm) and (b) pump + probe (200 nm + 243.1 nm), respectively. The delay between the pump and probe was set at 2 ps.....	179
5.3	Raw H ⁺ images following photodissociation at 200 nm and probing with 243.1 nm. Only half of each image is shown for illustrative purposes for pump-probe delays (t) of -0.5 ps and +2.0 ps, (a) and (b) respectively.....	180
5.4	H ⁺ transients as a function of H-atom kinetic energy. The dotted, dashed and solid lines correspond to pump (200 nm)-probe (243.1 nm) delays (t) of -0.5, 0 and 2 ps respectively.....	183
5.5	H ⁺ transients as a function of pump (200 nm)-probe (243.1 nm) delay for the low kinetic energy (a) and high kinetic energy (b) H-atoms in indole together with corresponding fits.....	184
5.6	N-H bond dissociation as a function of H-atom kinetic energy of H-atoms, following excitation of indole at 200 nm and probing H-atoms via (2 + 1) REMPI at 243.1 nm.....	185
6.1	Structures of, (a) p-ethylphenol, (b) tyramine and (c) tyrosine highlighting O-H bond containing labile H-atom.....	197
6.2	Two-colour TOF-MS of (a) tyramine and (b) p-ethylphenol at a pump (200 nm)-probe (243.1 nm) delay of 2 ps.....	199
6.3	(a) Two-colour TOF-MS of tyrosine at a pump (200 nm)-probe (243.1 nm) delay of 2 ps, (b) REMPI of H-atom as a function of wavelength. As the wavelength is tuned on resonance with the 2s ← 1s transition (λ = 243.1 nm) a sudden rise in the H ⁺ signal is observed as expected.....	201

- 6.4** Raw H^+ images (right) and deconvoluted H^+ signal as a function of H-atom kinetic energy (left) after O-H bond photolysis of (a) p-ethylphenol, (b) tyramine and (c) tyrosine. Each image and hence the corresponding kinetic energy spectrum is collected by setting the probe (243.1 nm) delay at 2 ps with respect to the pump (200 nm). For further details please see text.....**202**
- 6.5** H^+ transient as a function of pump (200 nm)-probe (243.1 nm) delay for the low kinetic energy feature, (a) and high kinetic energy, (b) for p-ethylphenol. The error bars correspond to two standard deviation of the mean representing a 95 % confidence limit.....**204**
- 6.6** H^+ transient as a function of pump (200 nm)-probe (243.1 nm) delay for the low kinetic energy feature, (a) and high kinetic energy, (b) for tyramine....**206**
- 6.7** H^+ transient as a function of H-atom kinetic energy. The black, pink and red lines represent the kinetic energy of H-atoms at pump (200 nm)-probe (243.1 nm) delays of 2, 1 and 0 ps, respectively, (b) parent tyrosine ion signal as a function of pump (200 nm)-probe (243.1 nm) delay.....**208**

List of Tables

- 1.1** Timescales for fast and ultrafast motions. On the left are the periods of intramolecular motions that are relevant to chemistry. On the right are the different perturbations that can result in a physical or chemical change. The duration of a chemical reaction spans over a wide range.....**53**
- 2.1** Crystal types generating various harmonics and their respective polarizations.....**89**
- 2.2** Presents the melting points, boiling points and molecular weights of biomolecules of interest.....**95**

Acknowledgments

First of all, I would like to express my sincere gratitude, thanks and appreciation to my able and learned supervisor Dr. Vasilios Stavros for his regular, gracious valuable suggestions, encouraging discussions and excellent guidance during the course of my PhD research work.

Special thanks goes to everyone I have had the pleasure working with at Warwick, amongst those are; Mr. Kym Wells for entertaining and enlightening discussions and also Mr. Dave Hadden and Mr. Craig Williams. I also want to thank Ms. Lara Pegg, Ms. Michelle Cheung and Mr. Jeremy Brown for their experimental assistance. I want to express my gratitude to Dr. Jan Verlet and Mr. Gareth Roberts for providing me with the POP program and for helpful discussions. I would like to thank Prof. Mike Ashfold for valuable discussions and Dr. Mike Nix for his contributions with both the phenol and indole work. Countless thanks and regards to Prof. Julie Macpherson and Prof. Tim Jones for their enlightening discussion during my end of year vivas (years 1 and 2) and their encouraging feedback.

I want to thank and acknowledge Mr. Lee Butcher, Mr. Marcus Grant, Mr. Kirk Harris, Mr. Peter Brindley and Mr. Jason Noone for their help during construction of experimental equipments and troubleshooting. I would also like to thank to all my colleagues with whom I shared office for their nice company.

Finally, I want to express my gratitude and huge thanks to my loving mother, *late* father, brothers, sisters and friends whose support and encouragement has been a huge factor in helping me to achieve my goals so far and whom, without their financial and moral help this thesis would not be.

Declaration

To the best of the author's knowledge, this thesis represents the original material. The work presented in this thesis is solely that of author, except where due credit is given in the text. This thesis has not been submitted for the award of any degree to any institute other than the University of Warwick.

Azhar Iqbal

Publications

The following publications have resulted from the work described in this thesis:

1. Iqbal, A.; Pegg, L.-J.; Stavros, V. G. Direct versus Indirect H-atom Elimination from Photoexcited Phenol Molecules. *J. Phys. Chem. A* **2008**, *112*, 9531-9534.
2. Iqbal, A.; Cheung, M. S. Y.; Nix, M. G. D.; Stavros, V. G. Exploring the Timescales of H-atom Detachment from Photoexcited Phenol-h6 and Phenol-d5: Statistical vs Nostatistical Decay. *J. Phys. Chem. A* **2009**, *113*, 8157-8163.
3. Iqbal, A.; Stavros, V. G. Exploring the Timescales of H-atom Elimination from Photoexcited Indole. *J. Phys. Chem. A* **2010**, *114*, 68-72
4. Iqbal, A.; Stavros, V. G. Active Participation of $^1\pi\sigma^*$ States in the Photodissociation of Tyrosine and Sub-units. *J. Phys. Chem. Lett.* **2010**, *1*, 2274-2278.

Abstract

The H-atom detachment driven through the $^1\pi\sigma^*$ states of biological chromophores containing an X-H bond (where X = N or O) upon UV absorption is ubiquitous in nature. Understanding the role of this dissociative state in the chromophores and their respective amino acids following UV excitation would enable a step change towards establishing a better understanding of the mechanisms of photostability of larger peptides in the gas-phase. The work presented in this thesis focuses on the H-atom elimination of phenol and indole, the chromophores of the amino acids tyrosine and tryptophan, respectively. The H-atom elimination has also been carried out in tyrosine and its sub-units p-ethylphenol and tyramine upon excitation at 200 nm. In all these systems the O-H bond fission on the phenol ring results in a range of H-atoms kinetic energy release.

Using a combination of femtosecond pump-probe spectroscopy, time-of-flight mass spectroscopy (TOF-MS) and velocity map ion imaging (VMI) reveals that H-atom elimination in all these systems occurs on an ultrafast timescale (~ 200 fs) for both fast and slow H-atoms. This casts considerable doubt over the previously assigned statistical origin of the slow H-atoms and suggests direct pathways to their formation. The H-atom kinetic energy spectrum in tyrosine also implies that H-atom elimination is occurring through the same coordinate i.e. O-H bond as exhibited by its phenol chromophore, thus confirming the active participation of the $^1\pi\sigma^*$ states from the chromophore of the amino acid to the amino acid itself. These findings are of great importance enabling one to compare these results with existing calculations on the chromophores which often model the system in an isolated environment.

These results also provide ground work for more complex calculation to be carried out, in particular on the amino acids and the di/tri peptides.

Chapter 1

Introduction

This thesis presents the relaxation mechanisms of the aromatic amino acids tyrosine and tryptophan and their chromophores following absorption of ultraviolet radiation. One of the key factors which play a prominent role in the photoresistivity of these systems, is the active involvement of the optically dark $^1\pi\sigma^*$ state. This state exhibits conical intersections (CIs) with the lowest electronically excited $^1\pi\pi^*$ state and with the electronic ground state (S_0), thus transferring population from the electronically excited $^1\pi\pi^*$ state to the ground state before any irreversible harmful reactions take place. This imparts the photostability to these important biomolecules. To develop a better understanding of the role of the $^1\pi\sigma^*$ state, namely to probe the evolution of this excited state in time and to pinpoint which factors control such nonadiabatic processes in phenol, indole and tyrosine in the gas-phase, femtosecond time-resolved spectroscopy, time-of-flight mass spectroscopy (TOF-MS) and velocity map ion imaging (VMI) techniques are employed.

The introduction starts with a brief history of reaction dynamics, which explains how collisions in the gas-phase help to overcome the barrier (transition state) for the reaction to occur. Later on, it describes how light can help overcome this barrier; following absorption of light it excites the molecule to a particular potential energy surface (PES). If the photon energy is sufficient it can also overcome the barrier. It also deals with the various intramolecular energy transfer

processes and their times scales. The work presented in this thesis is wholly based on experimental results; nevertheless, a light mathematical description has been given to explain certain intramolecular energy transfer processes and techniques. The real aim of this project is to study the gas-phase photodynamics of the amino acids and their chromophores. It also contains the flavour of various techniques that help to study the photodissociation dynamics in the gas-phase of biomolecules.

1.1. Brief History of Chemical Reaction Dynamics

1.1.1. The Arrhenius Concept of Reaction Dynamics

Chemical reactions are accomplished by bond breaking and bond forming. Chemical bonding dynamics is a basic requirement to understand the behaviour and the properties of materials and molecules. In the 20th century, chemists were trying to understand how the chemical reactions proceeded and how their kinetics was determined. In 1889 Svante Arrhenius proposed a seminal equation,¹ for two reactants where he related the rate constant k to temperature and energy of activation E_a by the following expression,

$$k = Ae^{-\frac{E_a}{RT}} \quad (1.1)$$

T is temperature, A is frequency factor, E_a is different from the thermodynamic net energy change between reactants and products and R is the universal gas constant. If the reactant B has a certain probability to collide with C, then the rate of the reaction is the collision frequency times the fraction of successful collisions with energy

equal to or more than E_a . The energy of activation can simply be calculated by an alternative form of the Arrhenius equation.

$$\ln k = \ln A - \frac{E_a}{RT} \quad (1.2)$$

A plot of $\ln k$ versus $1/T$ from equation (1.2) is used to calculate E_a . Arrhenius proposed a hypothetical body which later on was named activated complex, a central idea in the theory of reaction rates. According to this concept the reaction can proceed, for instance by collision only if it can overcome the barrier whose energy is equal to the activated complex.²

After a few years in 1894 Bodenstein published a paper on the system of hydrogen and iodine which played a very important role in understanding gas-phase kinetics and elementary mechanisms.² In the 20th century, Tolman³ (1920), Lindemann⁴ (1922) and Hinshelwood (1926) developed theories regarding unimolecular gas-phase reactions describing reaction mechanisms, chemical kinetics, energy redistribution and chemical rates. The Rice-Ramsperger-Kassel (RRK) theory was proposed in 1928 and later on Marcus in 1952 combined RRK with the transition state theory which accounts for the initial and transition-state vibrations, now known as the RRKM theory.^{2,5,6}

The rate constant $k(T)$ cannot provide the detailed picture of a molecular reaction because it relies on the change of equilibrium constant K with temperature T , over the course of the reaction according to van't Hoff's description. The rate constant measures the reactant-state to product-state over all possible encounters, for example relative velocities, orientations, vibrational and rotational phases and impact parameters. The actual goal of reaction dynamics is to measure quantitatively, how

the reactant molecules approach each other. After exchanging energy some bonds are broken and some are made through product formation.²

1.1.2. London, Eyring and Polanyi's Reaction Dynamics

Heitler and London presented a quantum mechanical treatment of the H₂ molecule in 1927 that dealt not only with the stable structure of the chemical bond but also with how two atoms can interact at different distances to one-another. One year later, London gave an approximate expression for the potential energy of triatomic H₃ using coulombic and exchange energies of the diatomic pairs. In 1931 Henry Eyring and Michael Polanyi calculated the PES for the reaction between H + H₂ using the London equation. This gave birth to “reaction dynamics” and one could relate the PES to the trajectories of the different dynamical processes.² Transition-state theory was formulated by Eyring⁷, Evans and Polanyi⁸. This theory was developed to describe chemical reaction rates and it contains the expression for the Arrhenius pre-exponential factor. The mathematical form of this equation is as follows,

$$k = \frac{k_B T}{h} K^\ddagger = \left(\frac{k_B T}{h} \right) \left(\frac{Q^\ddagger}{Q_A Q_B} \right) e^{-\frac{E_0}{kT}} \quad (1.3)$$

where k_B is Boltzmann's constant, h is Planck's constant and Q is the partition function. According to transition-state theory the fastest reaction was given by the frequency factor “ $k_B T/h$ ” for the passage through the transition state. At room temperature this value is $6 \times 10^{12} \text{ s}^{-1}$, corresponding to 170 femtoseconds (1 femtosecond (fs) = $1 \times 10^{-15} \text{ s}$) compared to molecular vibrations which occur in

typically 10-100 fs. These timescales are consistent with the speeds of nuclei and distances thereof involved in molecular reactions.²

1.2. Photochemistry and Reaction Dynamics

So far, the energy required to overcome the barrier for a chemical reaction to occur is brought about by collisions (kinetic energy exchange) between reactant molecules. Light can also provide this energy. Often, light is used to promote the system to an electronically excited state where the potential and the dynamics are different from ground electronic state. Photochemistry is not the only a way to drive chemical reactions but it offers a certain degree to controlling these reactions. This degree of control or selectivity can be obtained by manipulating the light to a certain wavelength that only allows accessing a particular excited state. In some cases, the manipulation of light leads to very short pulses (in time) and is used to study the dynamics of complex systems where the motions of nuclei are frozen. The experiments on a longer timescale than the lifetime of the transition-state not can furnish adequate information that is needed for this state.⁹ The ultimate goal of photochemistry is to access the transition-state either directly or indirectly by manipulating light. This can be achieved because the light can offer its services to access particular PESs.¹⁰

1.2.1. Construction of Potential Energy Surfaces

In order to understand how reactions are controlled or manipulated by light and how the intramolecular and intermolecular energy transfer processes are

monitored, one must understand certain characteristics of PESs such as topology. At this stage, it is important to establish some understanding about the construction of PESs. The PESs for a molecular system are defined as the potential energy of the atoms as a function of their relative position. For two atoms coming together to form a diatomic molecule, the potential energy is a function of one variable, the internuclear distance.¹¹ The PESs can be generated by using computational methods that are the approximate solutions to the electronic Schrödinger equation. The time independent Schrödinger equation can be expressed as,

$$\hat{H}\Psi_{r,R} = E\Psi_{r,R} \quad (1.4)$$

where \hat{H} is the Hamiltonian operator, E is the eigen value of this operator and represents the energy of the system and $\Psi_{r,R}$ is a wavefunction that depends on both electronic (r) and nuclear (R) coordinates, respectively. The wavefunction is a mathematical description of a particle and gives all the information about it, i.e., its position in space and the probability of finding this particle over a distance dx . The probability is proportional to the square of the wavefunction, which is normalised so that the integral of this is 1.

In molecular quantum mechanics if it is assumed that the nuclei and electrons are point masses and spin-orbit and other relativistic interactions are neglected, then the Hamiltonian can be written as,

$$\hat{H} = -\frac{\hbar^2}{2} \sum_{\alpha} \frac{1}{2m_{\alpha}} \nabla_{\alpha}^2 - \frac{\hbar^2}{2m_e} \sum_i \nabla_i^2 + \sum_{\alpha} \sum_{\beta > \alpha} \frac{Z_{\alpha} Z_{\beta} e'^2}{r_{\alpha\beta}} - \sum_{\alpha} \sum_i \frac{Z_{\alpha} e'^2}{r_{i\alpha}} + \sum_j \sum_{i > j} \frac{e'^2}{r_{ij}} \quad (1.5)$$

$$e' = \frac{e}{\sqrt{4\pi\epsilon_0}}, \text{ where } e \text{ is the elementary charge in Coulombs,}$$

α and β represents the nuclei and i and j represents the electrons. The 1st term in equation (1.5) is the kinetic energy operator for the nuclei. The 2nd term is the kinetic energy operator for the electrons. The 3rd term is the potential energy of repulsion between the nuclei, $r_{\alpha\beta}$ being the distance between nuclei α and β with atomic numbers Z_α and Z_β . The 4th term is the potential energy of attraction between the electrons and the nuclei, $r_{i\alpha}$ being the distance between electron i and nucleus α . The last term is the potential energy of repulsion between the electrons, r_{ij} being the distance between electrons i and j .

For two atoms to form a diatomic molecule, the potential energy is a function of one variable i.e. the internuclear distance. A plot of the potential energy as a function of internuclear distance gives a potential energy curve. But for non-linear polyatomic molecules, the Schrödinger equation has to be solved for $3N-6$ nuclear coordinates (for linear molecules the total number of degrees of freedom are $3N-5$) to view the full picture of the PES for the molecule, where N is the number of atoms in the molecule. This is not possible but PESs can be approximated by computing the Schrödinger equation based on the assumption that electronic and nuclear wavefunctions can be treated independently. This is known as the Born-Oppenheimer approximation and it relies on the basis that the electrons move rapidly with respect to the nuclear motion and the nuclear motion responds only to an effective potential generated by the averaged electron positions. This assumption simplifies equation (1.5) such that,

$$\hat{H}_{el} = \frac{\hbar^2}{2m_e} \sum_i \nabla_i^2 - \sum_\alpha \sum_i \frac{Z_\alpha e'^2}{r_{i\alpha}} + \sum_j \sum_{i>j} \frac{e'^2}{r_{ij}} \quad (1.6)$$

\hat{H}_{el} is the electronic Hamiltonian and its solution gives the electronic wave function Ψ_{el} that is a function of electronic coordinates and is only valid when the nuclear coordinates are fixed. The electronic Hamiltonian including nuclear repulsion is therefore $\hat{H}_{el} + V_{NN}$. The nuclear repulsion term is given by,

$$V_{NN} = \sum_\alpha \sum_{\beta>\alpha} \frac{Z_\alpha Z_\beta e'^2}{r_{\alpha\beta}} \quad (1.7)$$

The internuclear distance $r_{\alpha\beta}$ is not a variable but is fixed at some constant value. Of course, there is an infinite number of possible nuclear configurations and for each of these the electronic Schrödinger equation is solved to get the set of electronic wavefunctions (and corresponding electronic energies). When two eigenstates (corresponding electronic energies) of the electronic wavefunction undergo an avoided crossing at a given nuclear coordinate, when the nuclear motion directly affects the dynamics of the system and the Born-Oppenheimer approximation breaks down. Vibronic coupling effects such as intensity borrowing can not be modelled by this approximation because both the electronic and nuclear coordinates change simultaneously.

There are a number of sophisticated theoretical methods that not only give reasonable information about the shapes and energies of the molecular orbitals but also give adequate prediction and with reasonable accuracy the structure and reactivity of molecules. For instance, in *ab initio* methods a particular model is chosen for the electronic wavefunction and the calculations are performed at a particular level without any further approximations. The success of *ab initio*

calculations depend on the choice of appropriate model and the level at which the calculation is done. An alternative approach is the development of semi-empirical methods that are normally based on the formalism of *ab initio* methods. There are commercially available packages that are used for *ab initio* calculations. The problems are solved by evaluating thousands of integrals; this is greatly facilitated by expressing the atomic orbitals used in the linear combination of atomic orbitals (LCAOs) as linear combination of Gaussian orbitals. The advantage of Gaussian type orbitals ($e^{-\zeta r^2}$) over the hydrogenic orbitals ($e^{-\zeta r}$) is that the product of two Gaussian functions is itself a Gaussian function that lies between the centre of two contributing functions. Density functional theory (DFT) is another technique that is used to calculate the molecular structure and has been gaining considerable attention in recent years. The big advantage is that it demands less computational effort and leads to better agreement with experimental values than that obtained by *ab initio* methods. The main focus of DFT is that it deals with the electron density (ρ) rather than the wavefunction (ψ). The energy of the molecules is considered as function of electron density and is written as $E(\rho)$ and the electron density itself is a function of position of nuclei $\rho(r)$.^{12,13}

1.2.2. Photophysical and Photochemical Processes

Absorption of a photon by an atom or molecule can lead to production of an electronically excited state. Excited states exhibit different chemistry as compared to the parent ground state. There are number of ways in which the excited species can decay or lose its excess energy, some of the most important decay routes are as follows:

- Dissociation
- Charge transfer or direct reaction
- Isomerisation
- Intermolecular energy transfer
- Intramolecular energy transfer
- Luminescence (fluorescence or phosphorescence)
- Physical quenching
- Ionization

In excited molecules, the deactivation pathways compete with each other. Sometimes the intramolecular energy transfer becomes very important due to the fact that following excitation to a particular state, intramolecular energy transfer or indirect decay may populate another state that is inaccessible by direct absorption due to the selection rules for this process. One significant example of this mode of relaxation is population of a triplet state (T_1) after absorption from the ground state (S_0) to a singly excited state (S_1).¹¹ Therefore, it is of great importance to consider the timescales of intramolecular relaxation pathways as this in turn will help in understanding how PESs couple.

1.2.2.1. Phosphorescence and Intersystem Crossing

Phosphorescence is a radiative process in which the excited molecule discards its energy as a photon. Spontaneous emission in phosphorescence is much slower process as compared to fluorescence (see below) and sometimes emission persists for even hours. Phosphorescence times for large organic molecules typically range between $10^{-6} - 10^{-1}$ s.¹²

Phosphorescence is a forbidden luminescence process and in most of the organic molecules with a singlet ground state, the emitting species is a triplet state. Due to the long life time of a phosphorescent transition, collisional deactivation competes effectively with the triplet radiative pathway. Visible phosphorescence is normally not observed unless the collisional deactivation rate is reduced significantly. In rigid media the species cannot diffuse towards each other and the collisional deactivation is slow. The earliest investigations of phosphorescence were made on dyes of gelatin and subsequently in boric acids at room temperature. Phosphorescence was first observed in confined rigid glasses but this phenomenon soon appeared in other phases. Emission from biacetyl vapours is one of the most well known examples of gas-phase phosphorescence.¹¹

Figure 1.1 presents the sequence of events resulting in phosphorescence for a species with a singlet ground state. The first step is like normal luminescence (for example fluorescence) but the decisive role is played by the excited triplet state. At the point of intersection of PESs, the triplet and singlet excited states share a common geometry. As a result, if there is a mechanism of unpairing two electrons spins (for example the conversion $\uparrow\downarrow$ to $\uparrow\uparrow$), the molecules undergo intersystem crossing i.e., a nonradiative transition of different multiplicity and becomes a triplet state. In atoms, singlet-triplet transitions occur in the presence of spin-orbit coupling. The same is true for molecules and one can expect intersystem crossing to be more prominent when a molecule contains a fairly heavy atom because of large spin-orbit coupling.¹² Transition metal complexes contain a heavy transition metal as the central atom that mixes strongly the singlet and triplet states through spin-orbit coupling. As a result the triplet emission becomes large.¹⁴

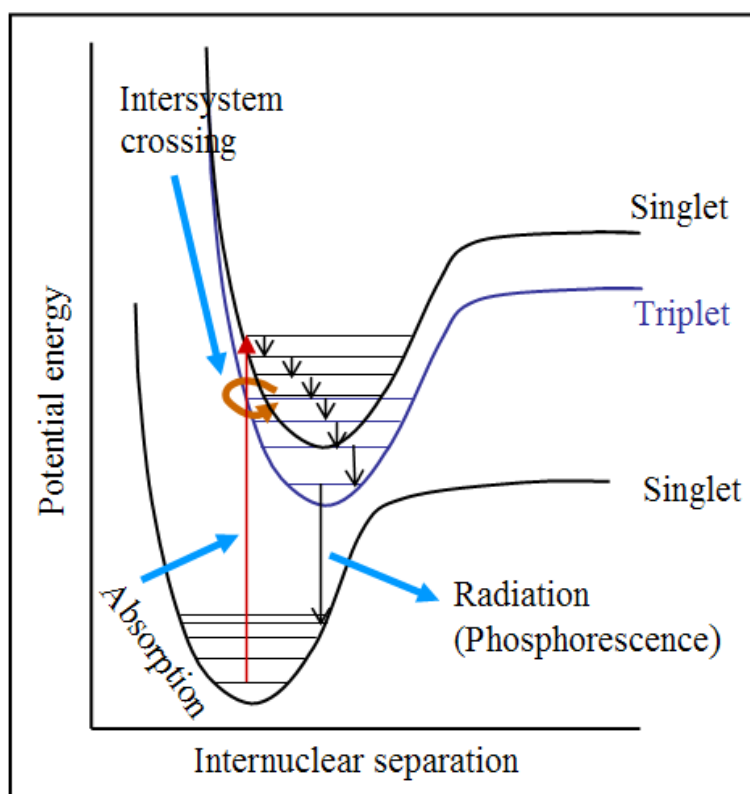


Figure 1.1 The schematic display of intersystem crossing and phosphorescence, where the excited singlet state mixes with an excited triplet state through spin-orbit coupling. The triplet state acts as a slowly radiating reservoir because the return to the ground state is spin forbidden.

1.2.2.2. Fluorescence and its Timescales

Electronic transitions occur within $10^{-16} - 10^{-15}$ s following absorption of an ultraviolet (UV) photon. Fluorescence is a radiative process; it is slower than absorption but faster than phosphorescence. The typical life time of fluorescence ranges from $10^{-12} - 10^{-6}$ s.¹² The excited singlet species can trigger ultrafast (femtosecond (10^{-15} s) to picosecond (10^{-12} s) timescales) photochemical reactions. Examples of these are the ultrafast reactions exhibited by the singlet excited states of biomolecules and will be discussed in forthcoming paragraphs and chapters.

The true picture of fluorescence can be seen whether the system is excited in the condensed phase or the gas-phase. In the condensed-phase the excited molecules are subjected to collisions with the surrounding molecules giving up energy nonradiatively whilst moving down to lower vibrational levels until reaching the lowest vibrational level of the electronically excited state, as manifested in figure 1.2.

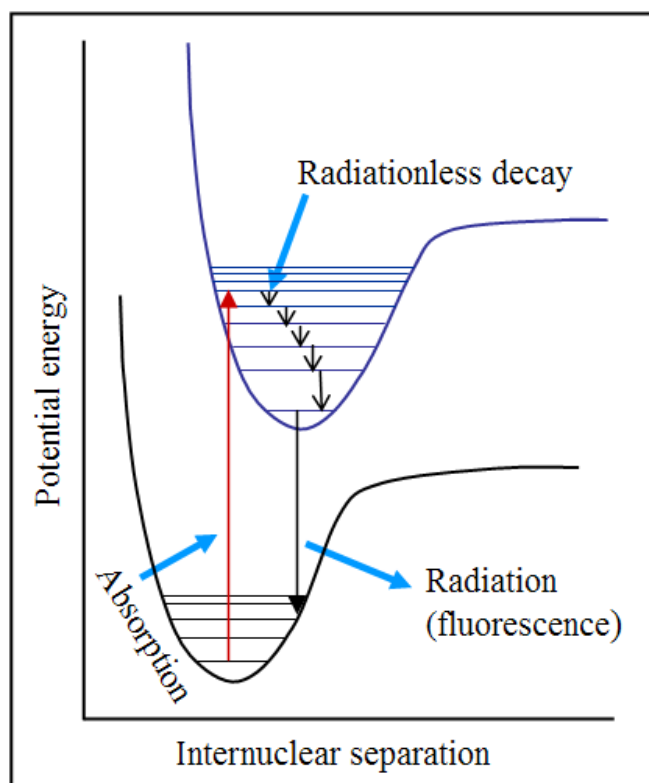


Figure 1.2 Pictorial representation of fluorescence. Following absorption, the upper electronic state undergoes radiationless decay to its lowest vibrational level. A radiative transition then occurs from the upper electronic state to the lower electronic state.

In the gas-phase at low pressures, this stepping down the vibrational ladder is obtained via intramolecular vibrational energy redistribution (IVR). At the lowest vibrational level of the excited state, the surrounding molecules in the condensed-phase and IVR in gas-phase might now be unable to accept the large energy

difference that will accompany the transition to the ground electronic state. If this situation persists long enough, the excited state undergoes spontaneous emission and emits the excess energy in the form of a photon. The upward and downward electronic transitions are vertical (according to the Franck-Condon principle that will be discussed later). An absorption spectrum displays the vibrational structure characteristic of the excited upper state and the emission spectrum exhibits the vibrational structure characteristic of the lower electronic state.¹²

1.2.2.3. Quenching of Fluorescence

Fluorescence is exhibited from an excited electronic state of an isolated atom. The system will typically fluoresce on a nanosecond (ns) timescale for an allowed transition. Shortening of the lifetime of the excited state is termed quenching. In larger polyatomic molecules, internal conversion from one excited state to another excited state that is dissociative along a certain bond coordinate can also quench the fluorescence. Examples of such systems are phenol and indole that are the chromophores of amino acids tyrosine and tryptophan respectively, and are extensively studied and detailed in this thesis. Fluorescence quenching can either be a desired process, for example energy or electron transfer or an undesired side reaction or process (rupture of chemical bond or collisional deactivation) that decreases the quantum yield of fluorescence. Consider a reaction, where the presence of a quencher Q, opens an additional channel for an excited species S^* to undergo relaxation,



v_Q and k_Q correspond to the rate of quenching and the quenching rate constant, respectively. Following some standard algebraic manipulation, one is able to derive the Stern-Volmer Equation presented below, which gives the relationship between fluorescence quantum yields $\phi_{f,0}$ and ϕ_f measured in the absence and presence of a quencher Q at molar concentration of [Q], respectively.

$$\frac{\phi_{f,0}}{\phi_f} = 1 + \tau_0 k_Q [Q] \quad (1.8)$$

This is a straight line equation with a gradient $\tau_0 k_Q$, which enables one to establish the rate constant for quenching (k_Q) and the fluorescence lifetime in the absence of quenching (τ_0). This method is also used to quench the phosphorescence.¹²

1.2.2.4. Internal Conversion and Predissociation

As discussed above, another relaxation pathway of an electronically excited molecule is through bond dissociation. If the absorbing photon carries enough energy to excite the molecule to a level where the vibrational structure becomes a continuum (see figure 1.3), this may cause the rupture of the bond. An indication for the onset of dissociation may be observed by monitoring the absorption spectrum, where the vibrational structure disappears or becomes structureless (i.e. continuous) above certain excitation energies. The absorption band becomes continuous due to the unquantized translational motion of the fragments.

In many cases the vibrational structure in the absorption spectrum disappears but it reappears at higher photon energies. This particular behaviour can be described

on the basis of molecular potential energy curves and is termed as predissociation. After excitation of a molecule to a certain vibrational level, the electrons may undergo redistribution that causes radiationless conversion to another state having the same multiplicity. This process is known as internal conversion (IC) and is illustrated in figure 1.3. At the point at which a bound excited state is intersected by a dissociative state, both PES share the common geometry and is termed as conical intersection (CI), a detailed discussion of which will be given shortly.

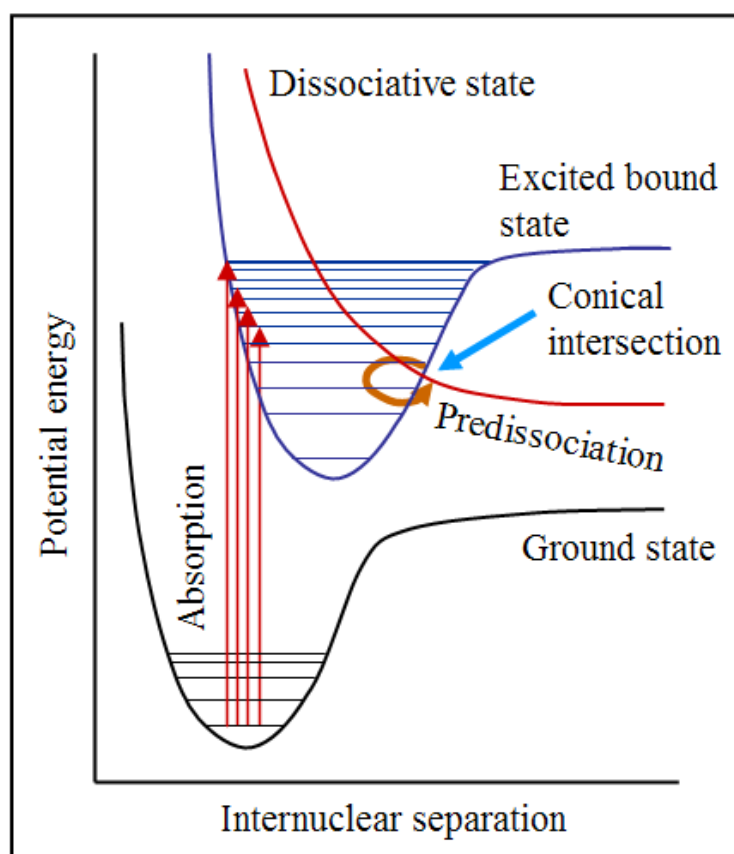


Figure 1.3 Diagram representing the predissociation mechanism.

As a result of the crossing of the PESs the absorption spectrum is blurred in the vicinity of a CI.¹² The dissociative state near the intersection point has a finite

lifetime and vibronic energies are not well defined. For instance in the later chapters, the timescales of one of the dissociative ${}^1\pi\sigma^*$ states will be reported, a state that is prevalent in biological systems. When the photon energy increases, the molecule may be excited to a vibrational level well above this point of intersection or to another electronic excited state where IC does not occur owing to the different geometries of the nuclei in different electronic states. As a result, the vibrational structure re-emerges.

1.2.2.5. Non-Crossing Rule, Adiabatic and Non-adiabatic PES

In a given molecule one can come across two PESs of the same spin and symmetry correlating to different dissociation limits. However, two states having the same spin multiplicity (S) and total angular momentum (Λ) interact repulsively and exhibit an avoided crossing. This leads to the non-crossing rule and suggests that in a diatomic molecule, assuming infinitely slow moving nuclei, as in the adiabatic Born-Oppenheimer approximation, two electronic states of the same spin and symmetry cannot cross. This rule is applied to adiabatic PESs and may be rephrased as: PESs of two electronic states with the same spin and multiplicity cannot cross each other. PESs which intersect are often known as diabatic or non-adiabatic PESs.

The avoided crossing can be explained by the following argument. Assuming that all the wavefunctions are known except two and if ϕ_1 and ϕ_2 are two mutually orthogonal functions which are also orthogonal to all the electronic wavefunctions for the other states, then the wavefunctions ψ_1 and ψ_2 for these two states can be written as linear combinations of ϕ_1 and ϕ_2 .

$$\begin{aligned}\psi_1 &= c_{11}\phi_1 + c_{12}\phi_2 \\ \psi_2 &= c_{21}\phi_1 + c_{22}\phi_2\end{aligned}\tag{1.8}$$

The energies E of the states and the wavefunctions can be obtained from a linear variational treatment giving the secular determinant

$$\begin{vmatrix} H_{11} - E & H_{12} \\ H_{12} & H_{22} - E \end{vmatrix} = 0\tag{1.9}$$

where H_{ij} represents the integral

$$\int \phi_i H \phi_j d\tau$$

in which H is the Hamiltonian operator. Equation (1.9) can be solved for E to give two roots.

$$E = \frac{1}{2}(H_{11} + H_{22}) \pm \frac{1}{2} \left[(H_{11} - H_{22})^2 + 4H_{12}^2 \right]^{\frac{1}{2}}\tag{1.10}$$

The potential curves can cross only if the two energies are equal. For this to be true it is required that $H_{11} = H_{22}$ and at the same time $H_{12} = 0$. The integral H_{12} can only be zero for all values of R (Internuclear separation) if ϕ_1 and ϕ_2 belong to different species, given that the spin-orbit coupling terms are absent from the Hamiltonian operator. If there is a value of R for which $H_{11} = H_{22}$ the potential curves will cross. However, ϕ_1 and ϕ_2 are of the same species then in general H_{12} will be non-zero and even if $H_{11} = H_{22}$ the potential curves will not cross. If to the left of the point of intersection ϕ_1 represents the lower state and ϕ_2 the upper state then it is expected

that to the right of the point of intersection ϕ_1 will describe the upper state and ϕ_2 the lower state, as illustrated in figure 1.4.

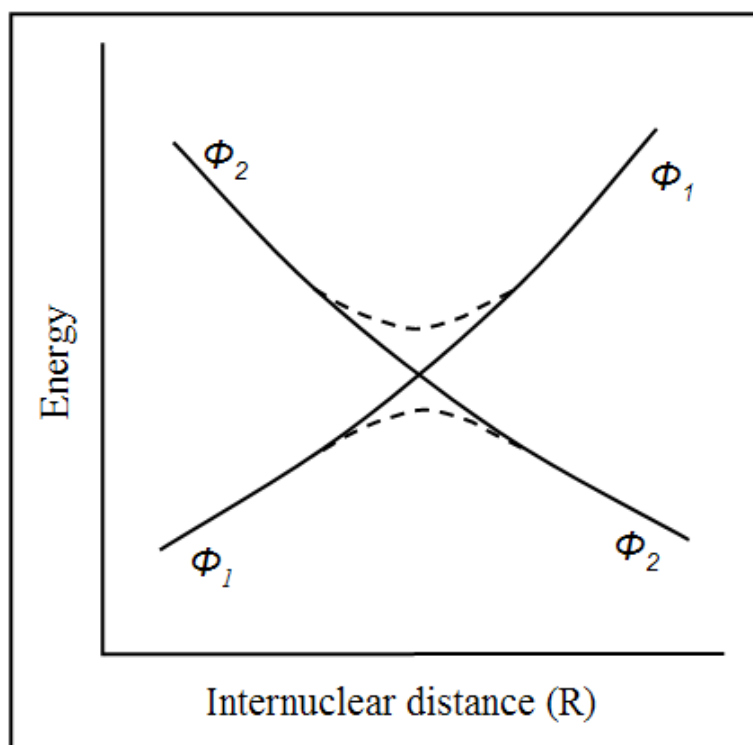


Figure 1.4 An avoided crossing between two diabatic functions ϕ_1 and ϕ_2 .¹⁵

As R increases in the region of avoided crossing the wavefunction changes from the lower state ϕ_1 to ϕ_2 . The functions ψ_1 and ψ_2 are the wavefunctions of the adiabatic PESs, and ϕ_1 and ϕ_2 are diabatic wavefunctions. Diabatic states (intersecting PESs or non-adiabatic PESs) can be represented by the variation of integrals H_{11} and H_{22} with R . The concept of diabatic states is not as clearly defined as the adiabatic case, the Born-Oppenheimer approximation becoming invalid in the region of narrowly avoided intersections and the coupling terms relating to the nuclear kinetic energy operator giving rise to transitions between adiabatic states.¹⁵

1.2.2.6. Conical Intersections

In a diatomic molecule there is only one geometrical parameter i.e. internuclear distance. Teller (1937) showed that in polyatomic molecules there are more degrees of freedom and two surfaces can cross if it is possible to vary two parameters, say x and y .¹⁶ If the point of intersection of two surfaces is taken as the origin at which $H_{11} = H_{22}$ and $H_{12} = 0$, the secular determinant can be rewritten, that is diagonal when $y = 0$,

$$\begin{vmatrix} W + h_1 x - E & ly \\ ly & W + h_2 x - E \end{vmatrix} = 0 \quad (1.11)$$

if we rewrite the diagonal elements in terms of $m = \frac{1}{2}(h_1 + h_2)$ and $k = \frac{1}{2}(h_1 - h_2)$, where h is the height of the cone, then this gives

$$\begin{vmatrix} W + (m+k)x - E & ly \\ ly & W + (m-k)x - E \end{vmatrix} = 0 \quad (1.12)$$

and its solution is

$$E = W + mx \pm \left(k^2 x^2 + l^2 y^2 \right)^{\frac{1}{2}} \quad (1.13)$$

This is the equation of a double cone with the common vertex at the origin $x = 0$ and $y = 0$, m and k are the number of variables in x and y directions, respectively, l is the interior of the cone and W is the separation of nuclei. The potential energy surfaces expressed as functions of x and y form a double cone and intersect at a single point known as the conical intersection (CI), an illustration of which is shown in figure 1.5.

Following this, Naqvi et al.¹⁷ showed that the non-crossing rule of potential surfaces as described above failed to describe the necessary conditions for crossing because it does not give special consideration to a value of R distinct from the crossing point, say R_0 . It has been suggested¹⁵ that the electronic wavefunction changes sign when the wavepacket (superposition of a few harmonic functions spread over a range of locations, details are given in section 1.3.2) goes once around the CI. In the case of polyatomic molecules the potential function will depend on more than two variables and the intersection between two surfaces will be a surface of dimension $m - 2$ where m is the number of variables in the potential energy function.

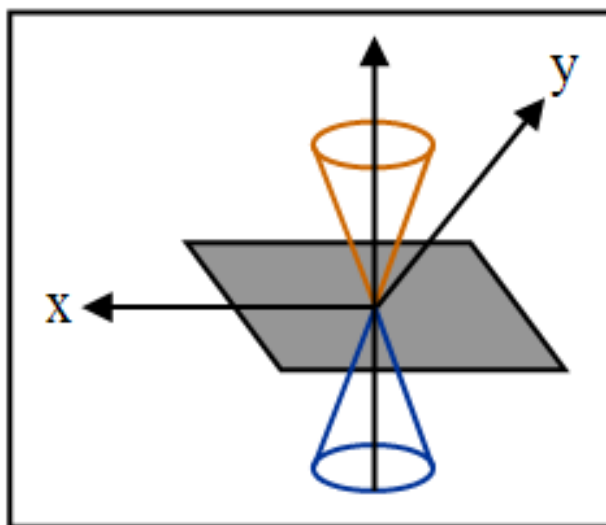


Figure 1.5 Schematic representation of a conical intersection between two PESs.

Adiabatic surfaces often are expected to exhibit avoided crossing, but distortions are observed at CIs due to the breakdown of the Born-Oppenheimer approximation. The main feature of a CI is its non-adiabatic nature and the breakdown of the Born-Oppenheimer approximation allows non-adiabatic transitions to take place. In the processes such as photodissociation, isomerisation, exchange collisions and energy

transfer, the CIs play a very important role. Ultrafast electron transfer is also mediated by CIs in biological systems.¹⁸

1.2.2.7. Franck-Condon Principle

According to the Born-Oppenheimer approximation, it is assumed that the electronic, vibrational and rotational energies are completely different due to the large differences in frequency between these three types of motions and can be dealt with separately to solve the Schrödinger equation. A further consequence of this approximation provides the basis of the Franck-Condon principle, which states that the nuclei of a molecule are assumed to be stationary during an electronic transition so that the transition can be represented as a vertical line on the potential energy diagram from a lower to an upper state, as indicated by the red vertical arrow in figure 1.6. Because of the rapid electronic transition, the stationary equilibrium separation of the nuclei in the initial electronic state becomes a stationary turning point in the final electronic state. This is the classical picture of Franck-Condon principle.^{10,11}

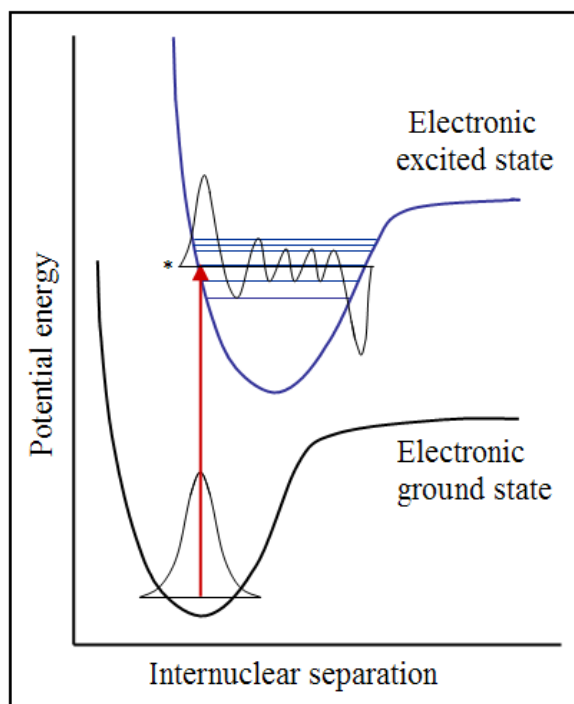


Figure 1.6 Diagrammatic representation of the Franck-Condon principle showing the vibronic coupling between two states of a molecule.

The quantum mechanical description of the Franck-Condon principle is necessary because the position and momenta of nuclei cannot be specified simultaneously. In quantum mechanics the vibrational motion of nuclei is described by a wavefunction whose square gives the probability of finding the nuclei at a certain position. According to de-Broglie, when the nuclei move the fastest, the wavelength of the wavefunction is the shortest and hence the wavefunction wiggles most but the amplitude of the wavefunction is the greatest when the classical motion is slowest i.e. at the turning points. The level marked as * in figure 1.6 corresponds to the position of the nuclei probably at the same initial separation R_e (equilibrium separation of nuclei), so this vibrational state is the most probable state for the termination of the transition. However, it is not the only accessible vibrational state, transitions can also occur to other vibrational states around R_e , but the most intense

corresponds to the state for which there is maximum overlap with the electronic ground state vibrational wavefunction (see below).

The quantitative description of the Franck-Condon principle can be expressed in the form of transition dipole moment, $\mu_{fi} = \langle f | \mu | i \rangle$ (i.e. transition dipole moment of the initial and final states i and f , respectively). In a molecule the dipole moment operator is taken as a sum of over all electrons and nuclei.

$$\hat{\mu} = -e \sum_i r_i + e \sum_I Z_I R_I \quad (1.14)$$

In this equation, the 1st term deals with the dipole moments of electrons and the 2nd term with the dipole moments of the nuclei, where r_i and R_I are the displacements from the centre of the charge of the molecule. The transition intensity is proportional to the square modulus of the magnitude of the transition dipole moment and this intensity is proportional to the square modulus of the overlap integral $S(v_f, v_i)$ between the vibrational states of initial and final electronic states.¹² This integral measures the overlap intensity between the vibrational wavefunctions in the upper and lower electronic states, for example for maximum overlap, S correspond to 1 and when there is minimal overlap, S corresponds to 0.

As intramolecular energy transfer processes mediated by CIs occur on femtosecond timescales, femtosecond time-resolution is needed to monitor these ultrafast processes. What follows is a brief description of various aspects of femtochemistry which are extensively used throughout this thesis work.

1.3. Femtochemistry

Femtochemistry deals with the act of molecular motion and brings chemistry down to femtosecond (10^{-15} second) timescales, in which chemical bonds are broken or formed. The advent of ultrafast lasers made it possible to record snapshots of chemical reactions with sub-angstrom resolution, where one angstrom $1 \text{ \AA} = 10^{-10} \text{ m}$. Prior to Femtochemistry, a combination of molecular beams (see later discussion) and picosecond lasers (1 picosecond (ps) = 1×10^{-12} s) led to the study of collision-free energy redistribution in molecules and state-to-state rates of chemical reactions.¹⁹⁻²⁵ But the time resolution was still poor in order to view the process of bond breaking and formation directly.

However, in the femtosecond (fs) time regime, it is now possible to observe chemistry happening at the transition-state between reactants and products. For instance, a 6 fs time resolution corresponds to a spatial window of $\sim 0.06 \text{ \AA}$ (assuming atoms move with a speed of $\sim 1000 \text{ m s}^{-1}$) through which atomic or fragment displacement along the reaction coordinate can be viewed.⁹

Experimentally, atomic-scale dynamics of molecular species and their reactions have now been observed and studied in all phases of matter. One unique example is the breaking and forming of the Na-I bond. At low enough excitation energies, the NaI system can be described by two PESs, one largely 'ionic' and other 'covalent' which cross at an internuclear distance of 693 picometers (10^{-12} m).

A short laser pulse (in time) is composed of a wide range of frequencies. As a result, excitation of NaI from the ground electronic state to the first excited electronic state populates a superposition of many vibrational states of NaI simultaneously. As a result, the electronically excited complex exists as a superposition of states, or a

localized wavepacket. The wavepacket oscillates periodically, exhibiting particle type behaviour during the course of the reaction between the covalent and ionic PESs. The ensemble of molecules behaves harmonically, showing single molecule motion. The initial wavepacket is highly localized at about 0.1 Å and remains intact for several periods of vibrations. The complex can also dissociate, if the wavepacket moves toward very long internuclear separation along the dissociative PES, as shown by arrows in the figure 1.7.

However, not each outward moving wavepacket leads to dissociation along the lower PES (covalent PES) because there is a probability that the trajectory of the wavepacket may remain on the upper PES (ionic). The dynamics of the systems can be probed by a second laser pulse whose frequency corresponds to the absorption frequency of the free Na product (on resonance with Na *D* lines at 589 nm) or to the frequency at which Na absorbs when it is the part of the complex.^{12,26-28} By probing the extent of the fluorescence from the excited Na atoms as a function of pump-probe delay, one is able to build up a real-time picture of the dissociating Na-I bond. The application of ultrafast laser pulses to study processes such as the above and many others led to the Nobel Prize being awarded to Professor Ahmed Zewail in 1999 for his contributions to Femtochemistry.

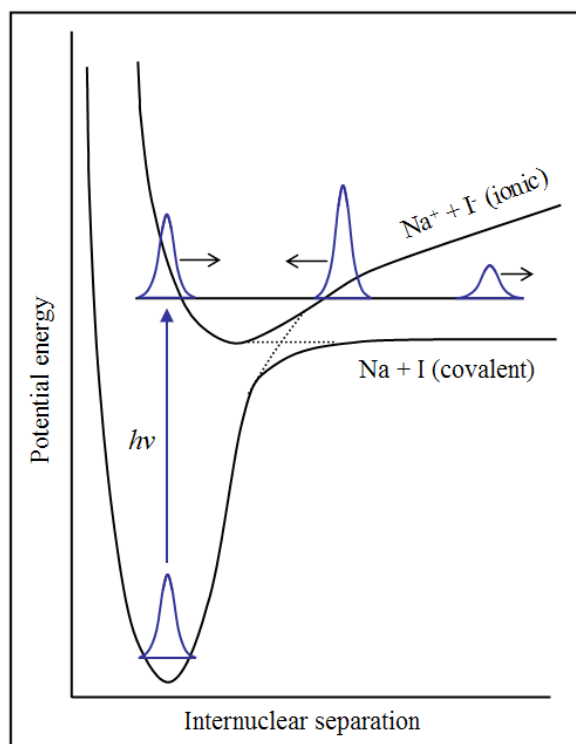


Figure 1.7 Pictorial representation of the femtochemistry of the NaI reaction, adapted from Zewail et al.²⁵ The wavepacket created by the laser excitation on the NaI PES moves between the ionic surface and covalent surface, and the out-put signal exhibits oscillations, when the wavepacket switches between ionic and covalent surfaces (see text for details).

1.3.1. Time-energy Uncertainty Principle

When the Schrödinger equation is solved for a system that changes with time, it suggests that it is impossible to specify the energy levels exactly. If on average a system stays in a state for a time τ , i.e. the life time of this state, then its energy levels are blurred to an extent δE . It follows that,

$$\tau \delta E \approx \hbar \quad (1.15)$$

This form of the uncertainty principle shows that the shorter the lifetime of the state (the shorter the time-constant τ for its decay), then the less precise its energy. When a state has a zero lifetime, nothing can be said about its energy, i.e. the energy is

infinite. On the other hand, the energy of a state can be specified exactly when its lifetime approaches infinity.¹⁹⁻²¹ This principle also suggests that to study the short-lived states the energy spread will be enhanced, but this problem can be dealt with by keeping in view the coherence principle which will be discussed in proceeding paragraphs.¹⁰

1.3.2. The Chemical Change and its Timescales

Femtochemistry centres on ones ability to record snapshots of molecules during the course of a chemical reaction. In other words one can view the motion of atoms during the course of a chemical reaction. Dynamic processes involved in chemistry and biology are followed by atomic motions in the course of transformations (e.g. isomerization, protein folding/unfolding). The atoms travel with a speed of approximately 1 km s^{-1} and hence the time required in probing the atomic-scale dynamics over a distance of 1 \AA is in the range of 100 fs. During such motions, as the reaction proceeds and passes through the transition state, the configuration between reactants and products cannot be isolated without resolution in both space and time on a femtosecond timescale.²¹ Atomic-scale or femtosecond resolution aims to examine the implications of Heisenberg's time-energy uncertainty principle. As stated above, this principle implies that if a system is probed over a very short time interval, the ability to know precisely the energy of the system is lost. The timescales of interest to chemists and biologists are presented in table 1.1.

Time (s)	Intramolecular time scales		Chemical time scales
atto 10^{-18}			
10^{-17}			
10^{-16}	Period of electronic motion in low n orbitals, Increases as n^3		
femto 10^{-15}	Vibrational motion; fast stretching motions, particularly in hydrides, slower for heavy atoms and/or shallow wells	Duration of reactions; fast for direct reactions or dissociation on a repulsive potential	Time between collisions in the liquid phase (pressure and viscosity dependent)
10^{-14}			
10^{-13}			
pico 10^{-12}	Rotational motion slower for large molecules with large moments of inertia	But slow to much slower for sticky collisions that proceed via an intermediate. Can be comparable to time between collisions	Intramolecular energy redistribution; faster at higher internal energies
10^{-11}			
10^{-10}			Time between collisions in the gas phase (decreases with increasing pressure)
nano 10^{-9}	Radiative decay from electronically excited states		

Table 1.1 Timescales for fast and ultrafast motions.¹⁰ On the left are the periods of intramolecular motions that are relevant to chemistry. On the right are the different perturbations that can result in a physical or chemical change. The duration of a chemical reaction spans over a wide range.

The uncertainty in energy is not only tolerable but due to the idea of coherence, it is also sufficient for the system to localize in space. The localization comes by combining the famous two uncertainty principles that is uncertainty in momentum ($\Delta x \Delta p \approx \hbar$) and in energy ($\Delta t \Delta E \approx \hbar$) resulting in the expression,

$$\Delta x = v\Delta t \quad (1.16)$$

where $v = p/m$ is the velocity of the particle. Equation (1.16) simply describes the relationship between the pulse duration (Δt) and the wavepacket spatial width (Δx) and suggests the requirements from the laser pulse to observe a given process. The pulse duration of the laser should be short enough such that one can localize the motion within the range of distances that is to be probed. In other words the laser pulse should be short compared to the intramolecular timescale of the motion that is to be followed. For example, when atoms are moving with a thermal velocity 3×10^4 cm s⁻¹, 100 fs is the time needed to travel a distance of 0.3 Å (typical distances involved with intramolecular motions). Achieving sub 100 fs pulses or pulses that are shorter in time than the vibrational period of the molecule will enable one to probe the bound intramolecular motions.^{2,10,21}

Probing the system over a very short time, say a time that is sufficient to probe electronic motion, according to the time-energy uncertainty principle this will result in a serious loss in energy resolution. As a result, there is a trade-off between time resolution and energy resolution. For example one can consider the electronic excitation of a diatomic molecule, as presented in figure 1.8.

The time-energy uncertainty principle dictates that the light pulse spans over a range of frequencies. The energy width of the laser pulse, as shown in figure 1.8, is small as compared to electronic excitation energy but is larger than a vibrational spacing. The pulse prepares the molecule in a definite excited electronic state but in a range of final vibrational states. The localized vibrational wavepacket formed in the excited state can be expressed as a linear combination of stationary (and delocalized) vibrational states. The contribution of each vibrational state is specified by its

amplitude, the amplitudes are chosen such that the initial wavepacket is localized and during motion on a harmonic potential well it remains localized as it evolves with the passage of time.¹⁰

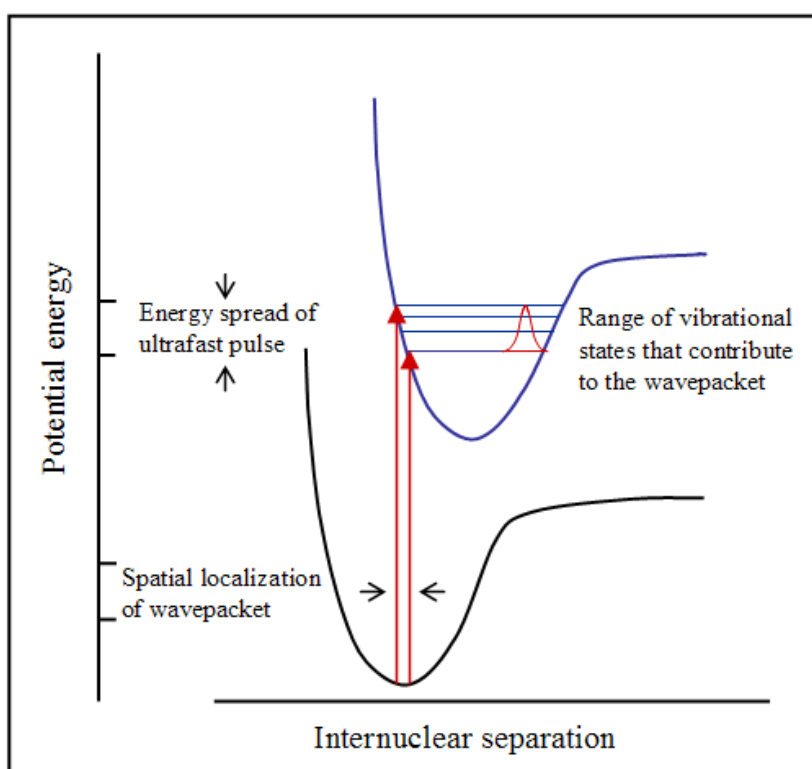


Figure 1.8 Pictorial representation of preparation of a localized vibrational state following excitation of a diatomic molecule using an ultrashort laser pulse.

The energy separation between the upper and lower well is $h\nu$ where ν is the vibrational frequency. The period of vibration corresponds to the inverse of the vibrational frequency. If the time resolution is better than a vibrational period, the energy resolution is inherently poorer than the spacing between the two adjacent vibrational levels of the upper state. Several vibrational levels will then contribute to the linear combination that creates the non-stationary state prepared by the short time pulse excitation, as presented in figure 1.8. Advantageously such a state is localized

within the potential well, unlike stationary vibrational states i.e. the states that are delocalised over the entire allowed region. Using ultrafast pump excitation a localized wavepacket is launched in the transition state region of a chemical reaction which one can then probe the temporal evolution toward the products.^{2,9,10,21,28,29} As discussed, Professor Ahmed Zewail was awarded the Noble prize in 1999 due to his key work in pioneering the area Femtochemistry. To study the reactions on femtosecond timescales, light sources are needed that can generate such short pulses. Ti:sapphire lasers are used widely in this regard and a discussion of fs lasers follows in the proceeding paragraphs.

1.3.3. Ti:sapphire Lasers

Titanium doped sapphire (Ti:sapphire) lasers are solid state lasers that are the most commonly used ultrafast lasers. These are commercially available ultrashort-pulse lasers and have played a key role in enabling the technology to be widely applied to study the photodynamics in gas³⁰⁻³² and condensed-phases^{33,34} of matter. Ti:sapphire lasers were first introduced in 1986 and after that they quickly replaced most dye lasers.³⁵ Dye lasers have been used in the past to generate short pulses down to ~30 fs, owing to the dyes large spectral bandwidth which is typically of the order of 20-30 nm. Under specific circumstances, organic dye based lasers have produced pulses as short as 6 fs.³⁶ Dye lasers however have several disadvantages, which includes instability, photochemical damage (of the dye), thermal effects and jet flow problems.³⁶

Ti:sapphire lasers contain Ti^{3+} ions at very low concentration in a host sapphire (Al_2O_3) crystal. The Ti^{3+} ions in the sapphire crystal exhibit a broad

absorption band centred at ~500 nm that results from vibronically allowed $d-d$ transitions of the Ti^{3+} ion (${}^2\text{E} \leftarrow {}^2\text{T}_2$ transitions) in the octahedral environment, provided by the sapphire host crystal through oxygen atoms. The emission spectrum of Ti^{3+} in sapphire spans over a wide range of wavelengths and provides a large gain bandwidth. In a Ti:sapphire laser, emission occurs from a very large number of closely spaced vibronic states of the medium. As a result, it is often called a vibronic laser.¹²

Passively mode locked Ti: sapphire lasers generate ultrashort pulses through Kerr lens mode-locking. Using this type of mode-locking method a pulse duration of about 100 fs is easily achievable and even pulse durations of 10 fs are possible for commercial devices. The shortest pulse durations of around 6 fs by using Kerr mode-locking was first demonstrated by Sutter *et al.*³⁷ and Morgner *et al.*³⁸ In addition to the ultrashort pulses, Ti:sapphire lasers provide a high saturation fluence around 1 J cm^{-2} , a property which allows the gain medium to be pumped at a high repetition rate that is essential for the amplification of laser pulses.³⁶ Broad wavelength tunability and hence production of ultrashort pulses justify the need of Ti:sapphire lasers in modern spectroscopy and photochemistry.

1.4. Gas-phase Photodissociation Dynamics

In modern photochemical research, lasers have provided the possibility of carrying out bond-selective or mode-specific dissociation of polyatomic molecules. There are two requirements that must be fulfilled to carry-out these kinds of studies. First it is necessary to put photon energy specifically into the bond that has to be broken. Secondly, the other pathways that destroy this specificity of excitation must

be slower as compared to the rate of dissociation. In the past, attempts have been focussed on the photochemical behaviour of predissociative excited electronic states of molecules via a specific vibrational mode. Predissociation gives a simple structured spectrum where the first requirement as described above is satisfied. But it has been found that energy redistribution occurs more rapidly as compared to dissociation, both in predissociation of excited electronic states³⁹⁻⁴⁷ and in infra-red multiphoton dissociation (IRMPD).^{48,49}

Such short times can be measured by performing a pump-probe experiment. In essence the first pulse, the pump, prepares the system in a particular state of the system and the second pulse, the probe, is delayed with respect to the pump to detect the outcome. A particular response to the probe pulse is monitored as a function of pump-probe delay. It is the time delay between these two pulses that needs to be shorter than the timescale of the event that we want to study. Each laser pulse on its own should typically be shorter than the process one wants to measure (although this can be overcome by careful data analysis and manipulation). This state-of-art technique is called pump-probe spectroscopy. Commercially available ultrashort pulse Ti:sapphire lasers have played a vital role in enabling the technology to be widely applied to study the photodynamics of reactions in the gas-phase in conjunction with molecular beams,^{2,10} that will be discussed in detail shortly.

1.5. Techniques to Study Gas-phase Dynamics

In the past two decades, lasers and their combination with molecular beam technologies have made great progress towards understanding the primary photophysical and photochemical processes. Better spectral and time resolution, in

addition to increasing laser powers (or pulse energies) and wavelength tunability have made it possible to excite the molecules selectively and with great efficiency. This has led to countless studies involving state-specific detection of dissociated products and their evolution in real time.

During the evolution between excitation and dissociation, various techniques can be used to determine the properties of the transition state (e.g. is it transition state linear or bent) such as measuring the product quantum-state distributions and/or the velocity and angular distributions of the fragments following dissociation.⁵⁰ Laser-induced fluorescence (LIF) and multi-photon ionization (MPI) provide extremely detailed information about the state-specific detection of fragments, and dynamics of photodissociated products.⁵¹⁻⁵⁴

1.5.1. Molecular Beams

Molecules in an isolated environment (collision free) can be studied with the help of molecular beam techniques. These techniques prepare molecules in significantly lower rovibrational states as compared to room temperature conditions, greatly reducing spectral congestion and thus simplifying spectral analysis. Free-jet expansions allow the expansion of a gas from a region of high pressure into a region of low pressure. If the pressure difference is large enough, supersonic speeds can be obtained by transferring the molecule's internal energy into translational energy, thus causing cooling of the gases. Typically for spectroscopic studies, the sample molecules are seeded in a carrier gas and their internal cooling is obtained by transferring their internal energy into translational energy of the carrier gas through soft collisions. A supersonic expansion provides the isolated molecular environment

to study intramolecular processes (e.g. photochemical) with large molecular densities of sample and with translational and rotational temperatures below a few Kelvin.^{55,56}

Using a noble gas as the carrier gas, one is able to predict qualitatively the velocity of the sample molecules of interest and the cooling that might be achieved. Skimmers allow selection of the core of the free-jet expansion (situated down-stream from the jet), generating a molecular beam with a narrow spread of velocities and therefore lower translational temperatures. To maintain a low pressure in the vacuum chamber pulsed valves are used. Pulsed valves allow a very small throughput of the gas into the interaction region of the vacuum chamber and hence the low pressure can be maintained with small vacuum pumps, thus reducing the price of pumping (a description of pulsed valves is given below). Figure 1.9 is adapted from G. Scoles, "Atomic and molecular beam methods vol. 1". This book gives a rigorous mathematical treatment behind these processes and provides an overview of the procedures and technologies in the production of molecular beams.⁵⁷

There have been further developments in this technology in order to produce supersonic expansions that produce the best cooling comparative to pumping requirements (i.e. cost). Solenoid-driven pulsed valves are one of these which are very easy to use and can be operated at repetition rates of up to 200 Hz.⁵⁸ Since ultrafast laser techniques have grown in popularity, and given that these lasers typically run at higher repetition rates than 200 Hz, the need for valves with higher repetition rates have grown. The Even-Lavie valve⁵⁹ is one such valve which runs at up to 1 kHz. This valve has been used throughout the work described in this thesis. Further details regarding the characteristics of this valve will be given in chapter 2.

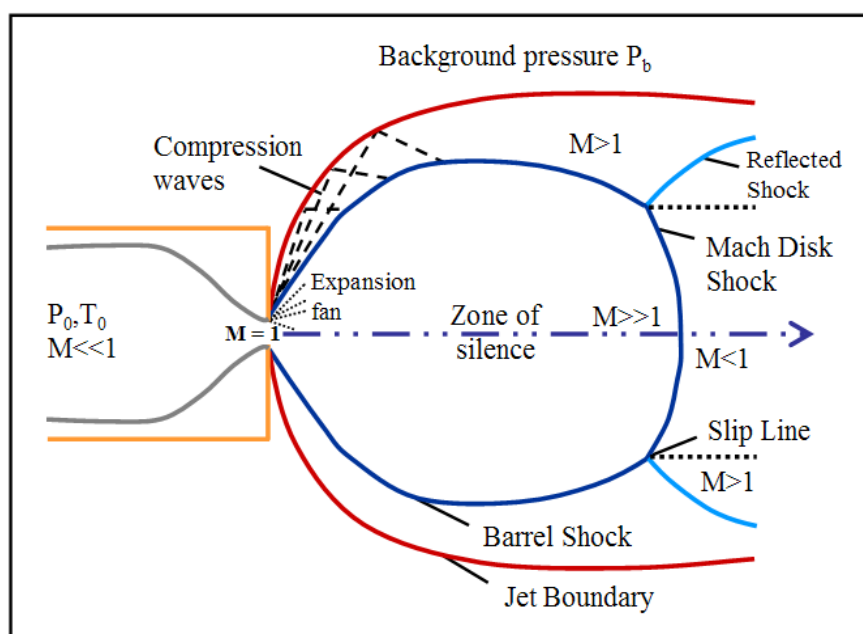


Figure 1.9 Pictorial representation of a continuous free-jet expansion from a nozzle. The zone of silence is the region of expansion where the Mach number (M) $\gg 1$ and this is the collision free region. The regions where $M < 1$ are not collision free. The blue lines are the outer limits of zone of silence and separate this region from the barrel-shock region that contains pressure shock waves.

1.5.2. Laser Induced Fluorescence

In laser induced fluorescence (LIF), the laser excites the molecule to an electronically excited state which then decays back to a lower lying state with the emission of a photon. Detection of photons can be used to obtain specific rotational-vibrational level information of products. Pump-probe LIF is used to monitor the reactions in such a way that a pump pulse excites the molecules to a certain PES covering a range of vibrational levels and the excited molecules evolve in real time towards products. The probe pulse is delayed in time with respect to the pump pulse and is tuned to either a transition of the reactants or the final products. As the delay is

varied the resulting fluorescence in the transient provides details relating to the dynamics of the process.⁶⁰⁻⁶⁵

1.5.3. Photoelectron Spectroscopy

Photoelectron spectroscopy deals with the measurement of kinetic energies of emitted electrons from different atomic or molecular orbitals following absorption of photons of an appropriate energy. The information in the kinetic energy of the ejected electrons is used to infer the energy of molecular orbitals. When a photon ionizes a system (atom or molecule), the conservation of energy means that the energy of the absorbed photon should equal to the sum of the ionization potential I of the system and the kinetic energy of the ejected photoelectron.

$$h\nu = \frac{1}{2} m_e v_e^2 + I \quad (1.17)$$

Equation (1.17) is analogous to the equation used for the photoelectric effect where the work function is now replaced by the ionisation potential. Following absorption of photons, photoelectrons are ejected from different orbitals each having a different ionization energy. As a result, the ejected photoelectrons will have differing kinetic energies. Thus, equation (1.17) must be modified to incorporate this and is now given by,

$$h\nu = \frac{1}{2} m_e v_e^2 + I_i \quad (1.18)$$

Where, I_i is the ionization energy of ejected electron from the i^{th} orbital. Kinetic energies of photoelectrons can be obtained by knowing v_e (velocity of ejected

electrons) and hence the ionization energies can be calculated. Koopmans theorem is used to interpret the photoelectron spectra, which states that the ionization energy I_i is equal to the orbital energy of the ejected electron and formally written as, $I_i = -\epsilon_i$.^{12,66} In other words, this theorem helps to identify the orbital from which the photoelectron has been ejected. This theorem assumes that the ionization is instantaneous and it occurs without any nuclear rearrangement. In gas-phase photoelectron spectroscopy, this has proven a powerful tool in resolving the photoelectron angular distributions of polyatomic molecules, mechanisms of intramolecular energy redistribution in excited states and in determining the ionization potentials of molecules.⁶⁷⁻⁷⁰ Photoelectron spectroscopy is also used to study analogously solid surfaces and is often called photoemission spectroscopy.¹²

1.5.4. Resonance Enhanced Multiphoton Ionization

Multiphoton ionization (MPI) techniques are a good alternative for the study of weakly fluorescing systems. MPI involves the absorption of several photons of light by a molecule that results in the ionization of the molecule, if the total energy of the absorbed photons is higher than the ionization potential. With the help of this technique, species-selective ions for analytical purposes can be produced, with lasers in the visible and UV region. There are several articles on this topic which cover the selected aspects of this topic.⁷¹⁻⁷⁶ In the case of studying reaction dynamics, MPI is used in which one of the laser pulses, typically the probe, ionizes one of the products of the reaction which is then detected using time-of-flight mass-spectroscopy (TOF-MS). A detailed description of TOF-MS will be given in chapter 2. By recording the

intensity of the product ion as a function of pump-probe delay, one is able to extract information regarding the dynamics of the process.

An important application of MPI is resonance-enhanced multi-photon ionization (REMPI),^{77,78} in which one or more photons excites the molecule to an intermediate state and then additional photons ionize it. The ionization/detection step can compete with other relaxation pathways which can lead, for example, to the study of the predissociation dynamics of the state-selective neutral species.⁷⁶ This application of MPI has emerged a powerful tool to study the ultrafast dynamics of biomolecules mediated by predissociative states.⁷⁹ Mathematically, one can show that for two photons the transition probability ($W^{(2)}$) is given by,⁸⁰

$$W^{(2)} \propto I^2 \left| \sum_m \frac{\langle n | \mu | m \rangle \langle m | \mu | a \rangle}{\Delta E_{ma} - \hbar \omega_r} \right|^2 \quad (1.19)$$

where I is the intensity of the laser, a , m and n are the initial, intermediate and final states respectively, ΔE_{ma} is the energy difference between the intermediate and initial states, μ is the dipole moment and ω_r the laser frequency. Expression (1.19) suggests that the two photon transition probability is directly proportional to the square of the laser intensity; generally, the n -photon transition probability is proportional to I^n . If no saturation occurs, then the formal intensity law for a multiphoton transition can be expressed as,

$$\ln W^{(n)} = n \ln I + C \quad (1.20)$$

where n represents the number of photons and C is a constant. When a species is subjected to a strong laser field i.e. a multiphoton excitation, this law deviates from linearity due the saturation effects in the population of relevant intermediate states.

Figure 1.10 (a) represents the situation in which the ionization occurs through a virtual state. For this process to be efficient the absorption of two photons should be instantaneous. A sudden increase in the absorption signal can be observed when the laser frequency is tuned to a real intermediate state as represented by figure 1.10 (b). This is termed a resonant two-photon transition. Equation (1.19) suggests that as the laser frequency moves from a non-resonant to a resonant condition, the denominator tends to zero and the equation no longer holds. For an allowed transition representing a resonant intermediate state, the excitation probability is considered proportional to the square of the overlap integral between the wavefunctions of initial and final states. The ion signal is considerably enhanced if the conditions are fulfilled for a resonant situation as compared to a non-resonant situation. To explain (2 + 1) REMPI as shown in figure 1.10 (c), the two-photon process is modelled using equation (1.19) which accesses the final resonant state followed by absorption of a subsequent third photon leading to the ion state. Resonant enhancement in the ion signal can also be observed, if two different radiation frequencies are spatially and temporally overlapped as is shown by figure 1.10 (d).

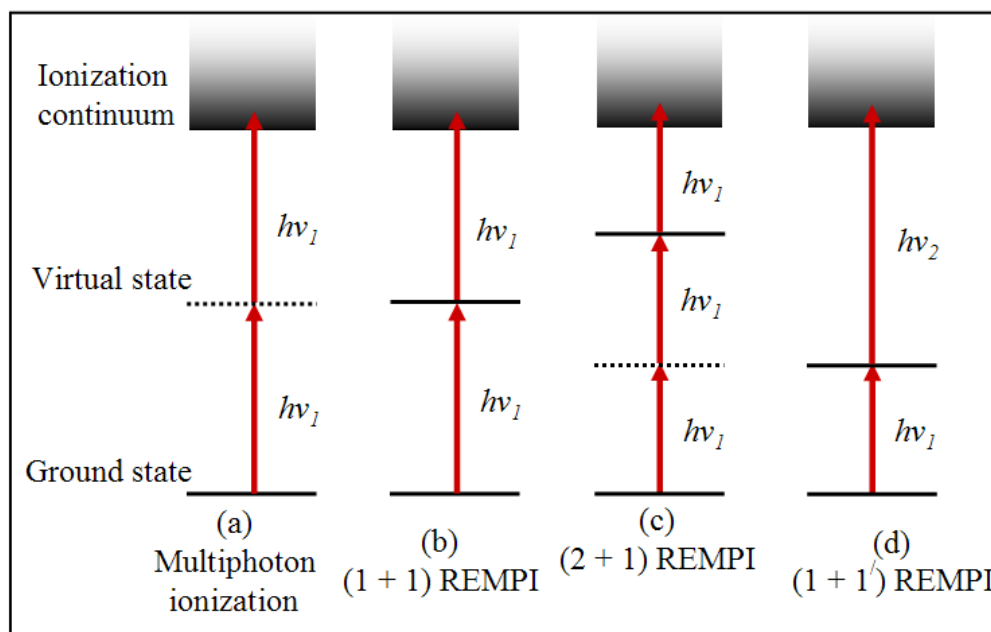


Figure 1.10 Pictorial representations of multiphoton ionization schemes.

1.5.4.1. Photofragment Translational Spectroscopy

Photofragment translational spectroscopy (PTS) provides a detailed insight into the dynamics of photofragmentation processes of molecules by measuring the translational energy distributions of the recoiling products. H Rydberg atom PTS is a technique used to study the gas-phase photodissociation dynamics of molecules which result in the elimination of a H-atom as one of the photo-products.⁸¹⁻⁹² The advantage of Rydberg tagging is that it prevents the blurring of the kinetic spectrum of the photofragment that occurs due to the direct ionization of recoiling fragments which repel one another when the molecular beam is intercepted by the ionizing laser beam. In order to avoid this problem, the photofragment product is excited to a high Rydberg state with a lifetime in the range of milliseconds (ms) that is just below the ionization energy. Following this, a small electric field is applied to these highly excited molecules to ionize them prior to detection.

The principle of this technique is based on the measurement of the velocity of the H-atom products with the help of time-of-flight (TOF). The conservation of energy and momentum is used to calculate the kinetic energy deposited in the H-atom fragments. The spread in the kinetic energy spectrum of H-atoms also reflects the internal energy and angular distribution of the partner-fragments. Consider the photodissociation of an H-X bond (where X is any partner fragment of H). Following photodissociation, the total kinetic energy released (TKER) in the dissociation can be expressed by,

$$TKER = \frac{1}{2} m_H \left(1 + \frac{m_H}{m_X} \right) \left(\frac{d}{t_H} \right)^2 \quad (1.21)$$

where m_H and m_X are the masses of H-atom ($m_H = 1.0079$ u) and the partner fragment (X), respectively, d is the length of the flight path and t_H is the measured H-atom TOF. As a result, by measuring only the TOF of the H-atom, the TKER can be extracted and in doing so can lead to important information pertaining to the internal energies of the photofragment X.

1.5.4.2. Multi-mass Ion Imaging

The multi-mass ion imaging technique consists of a molecular beam, a photolysis laser beam, a vacuum ultra-violet (VUV) probe laser beam, a constant momentum mass spectrometer and 2-dimensional (2D) ion detector.⁹³ A molecular beam of the target molecules is fired through a pulsed nozzle and is photodissociated by a laser pulse. The photo-products expand into a large sphere while travelling towards the ionization region due to the recoil and centre-of-mass velocity and are

ionized by a VUV (vacuum ultraviolet) laser pulse. Before the VUV probe laser pulse arrives the voltage on the extraction plates is adjusted such that the ions produced by the photolysis lasers are expelled, thus avoiding the ions produced by the multiphoton absorption of the photolysis pulse. Ensuring all the ions are expelled, the VUV laser pulse arrives to ionize the neutral fragments. It is also ensured that the VUV laser pulse passes through the centre that generates a line through the centre-of-mass of the dissociated products after photo-ionization. The length of the segment is directly related to photofragment recoil velocity multiplied by the delay between photolysis and ionization laser pulses. At the end of the mass spectrometer a 2D detector is used to monitor the position and intensity distribution of photoproducts. This 2D picture provides the information about the recoil velocity axis and the mass axis.^{94,95} By monitoring the recoiling velocity of the photo-products; this technique enables one to determine the various photodissociation pathways in the molecules.

1.6. Spectral Broadening

There are a number of effects which contribute to the widths of spectroscopic lines. Some of these contributions can be removed by changing the conditions and hence increase the spectral resolution. One example of this is when the transitions in a given molecule are very close in frequency such that their spectral shapes overlap due to Doppler broadening. In conventional spectroscopy Doppler-free methods are necessary to obtain better resolution of spectral lines.

1.6.1. Doppler Broadening

A photon of frequency ν absorbed by an atom/molecule travelling with a velocity V , relative to the light source (laser) will be different from that absorbed by the same molecule if stationary by an amount given by the relation given below,

$$\nu = \nu_0 \left(1 \pm \frac{V}{c} \right) \quad (1.22)$$

where, ν_0 is the frequency of photon absorbed by the molecule at rest. Consequently, to excite a transition in a molecule moving toward the source (laser), it is necessary to tune the laser frequency to slightly lower frequency and if the same molecule moves in the opposite direction then one needs to tune the frequency to slightly higher frequency. The spread of frequencies absorbed by the ensemble of molecules moving in different directions provide information about the kinetic energy of the photodissociated products.^{10,12}

1.6.2. Lifetime Broadening

Lifetime broadening is often termed uncertainty broadening. The energy spread is normally reported in wavenumbers via $\delta E = hc\delta\tilde{\nu}$ and by including the values for the various constants, the expression for lifetime broadening can be expressed,

$$\delta\tilde{\nu} = \frac{5.3\text{cm}^{-1}}{\tau / \text{ps}} \quad (1.23)$$

where τ is the lifetime of state and $\delta\tilde{\nu}$ represents the spread in energy. Since all the excited states are subjected to a finite lifetime, all the states experience a lifetime

broadening. The shorter the lifetime of a state involved in a transition, the broader the spectral line. One of the dominant factors that play a role for a finite lifetime of the excited state is the collisional deactivation. This collision could be with other molecules or with the walls of the surrounding container. The collisional lifetime can be expressed in terms of energy as, $\delta E \approx \hbar/\tau_{col}$. Since, $\tau_{col} = 1/Z$, where Z is the collisional frequency and as Z is proportional to pressure, the collisional linewidth is proportional to pressure. By working at low pressures, the collisional linewidth can be minimized.

The rate of spontaneous emission cannot be changed because it is the inherent property of a transition and the resulting lifetime broadening is the natural linewidth of the transition. The natural linewidths strongly depend on the transition frequency. For low frequency transitions, the natural linewidths are very small and are affected the most by collisional and Doppler line-broadening.

The natural lifetime of electronic transitions are very much shorter than the vibrational and rotational lifetimes and the linewidths are therefore much greater than the vibrational and rotational transitions. Relaxation of an electronically excited state typically occurs on the timescale of 10^{-8} s (~ 10 ns) that corresponds to a linewidth of approximately 5×10^{-4} cm^{-1} (15 MHz). On the other hand side a natural rotational lifetime is about 10^3 s with a linewidth of 5×10^{-15} cm^{-1} ($\sim 10^{-4}$ Hz).¹²

1.7. Photostability of Aromatic Amino Acids and Gas-phase Photodissociation Dynamics

The amino acids are one of the most important molecules in nature, because they exhibit many functions in metabolism. One of the key functions is the building blocks of proteins. Aromatic amino acids like tyrosine and tryptophan contain large rigid aromatic groups, namely phenol and indole, respectively. Tyrosine and tryptophan are the largest amino acids and their mutual hydrophobic interactions are of great importance for the correct folding of proteins, as these chromophores tend to be located inside the folded protein molecules.

The photochemistry and photophysics of tyrosine and tryptophan is very important because they both exhibit large UV absorption cross-sections, however their fluorescence quantum yields beyond a certain excitation threshold decreases. This suggests that there must be efficient non-radiative processes involved which effectively reduce the fluorescence.⁹⁶⁻⁹⁸ The non-radiative processes are supposed to occur on an ultrafast timescales. This converts the electronic energy into vibrational energy after IC, thus vibrationally excited molecules quickly dissipate their energy to surrounding molecules through intermolecular energy transfer, before harmful reactions take place. The ultrafast relaxation pathways impart photo stability to these important photoactive molecules.⁹⁹ Phenol and indole, which are the chromophores of the amino acids tyrosine and tryptophan respectively, show similar low fluorescence quantum yields.⁹⁶⁻⁹⁸ The aromatic amino acids tyrosine and tryptophan are illustrated in figure 1.11 with their corresponding chromophores highlighted (dashed line).

The knowledge of gas-phase properties of chromophores and their amino acids is of fundamental importance in order to develop an understanding of the complex electronic structure of polymers such as peptides, proteins and oligonucleosides. A combination of two-colour pump-probe spectroscopy, time-of-flight mass spectroscopy (TOF-MS) and velocity map ion imaging (VMI) in the isolated environment provide ideal conditions to extract detailed information about the ultrafast IC processes involved following excitation to a particular electronic state.

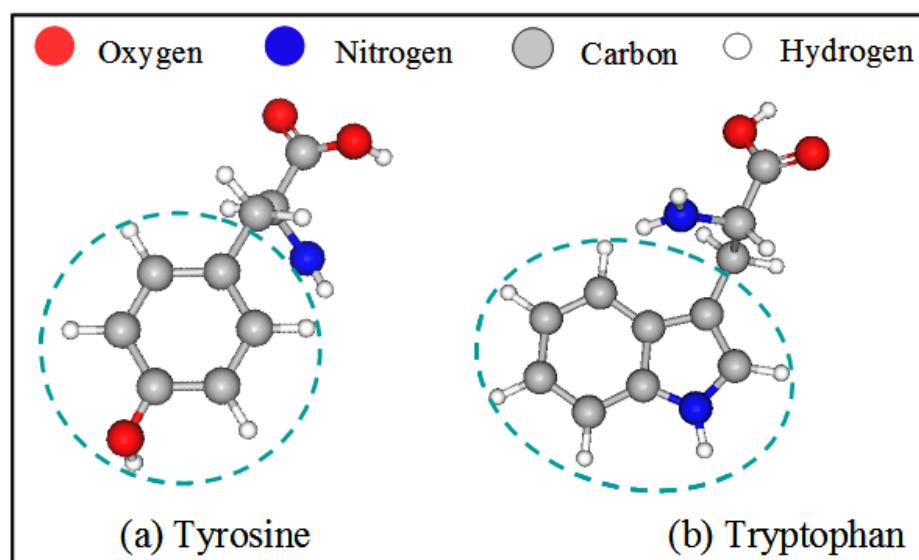


Figure 1.11 Aromatic amino acids.

1.7.1. Gas-phase Photodynamics of Chromophores

As phenol and indole are the chromophores of the amino acids tyrosine and tryptophan respectively, these molecules have been a prime focus of photochemical studies in recent years, being prototypical molecules for developing a better understanding of the electronic structure and photochemistry of other, larger hetero-

aromatic amino acids. Calculations by Sobolewski et. al¹⁰⁰ suggest that UV energy absorbed is localised at the O-H and N-H co-ordinates of these biomolecules, ultimately leading to H-atom elimination and proposed that the low fluorescence quantum yield of phenol and indole following excitation at the wavelength of interest here (200 nm in these experiments, whose results will be discussed in chapters 3-6) is primarily due to an excited singlet state of $^1\pi\sigma^*$ (S_2) character, which is dissociative with respect to the stretching coordinate of the O-H and N-H bond, respectively. This dissociative state intersects both the optically bright $^1\pi\pi^*$ (S_1) state and the ground state (S_0) through two successive conical intersections (CI, S_1/S_2 and S_0/S_2 , respectively), leading to elimination of neutral H-atoms. The figures of PESs and their labelling are presented in chapters 3 and 5.

The first experimental evidence of H-atom elimination of these systems in the gas-phase was reported by Ni et. al^{101,102} using the multi-mass ion imaging technique. Later, Nix et. al^{103,104} also reported H-atom elimination and gave it a more rigorous treatment with the help of the TKER technique suggesting various pathways of H-atom elimination. According to their observation, the high kinetic energy H-atoms observed in their measurements occurred through direct coupling of PESs whilst the low kinetic energy H-atoms detected resulted from statistical unimolecular decay of hot molecules following internal conversion from the electronically excited state to the ground state.

The timescales of H-atom elimination are of obvious importance. This provides the driving force to study H-atom elimination in a time-resolved fashion, in these systems. As mentioned above (section 1.3.2) the dissociation on a repulsive PES occurs on a femtosecond timescale. This has been clearly manifested in these

experiments. Following excitation at 200 nm and probing the H-atoms at 243.1 nm, time-resolved TOF-MS and VMI techniques revealed that the H-atoms detachment occurred on ultrafast timescales ~ 200 fs in both phenol and indole. These observations strongly suggests that one is able to rule out the relaxation to the ground state followed by statistical unimolecular decay as a competing route to H-atom abstraction.^{79,105,106} A detailed treatment of these pathways will be provided in the proceeding chapters.

1.7.2 Gas-phase Photodynamics of Tyrosine and

Sub-units

The involvement of the $^1\pi\sigma^*$ state has been clearly implicated in these studies, contributing to the dynamics of both the chromophores phenol and indole. Experiments have also been performed in tyrosine and derivatives such as p-ethylphenol and 4-(2-aminoethyl) phenol (tyramine) to see whether the $^1\pi\sigma^*$ state is operative and contributes to the H-atom elimination dynamics in bulkier systems.

To the best of our knowledge, H-atom elimination dynamics in p-ethylphenol have been studied by Tseng and co-workers⁹⁹ with the help of multi-mass ion imaging technique following excitation at 248 nm. The H-atom elimination followed the same trend as with the un-substituted phenol. They could not observe any H-atom elimination from tyramine at the same excitation energies.

It is always a challenge to introduce amino acids in the gas-phase with conventional valves due to decomposition upon heating. In our experiments this difficulty has been overcome by making slight changes to the Even-Lavie valve and

molecular beams of tyramine and tyrosine have been successfully generated. Time-resolved VMI measurements after excitation at 200 nm tend to suggest that ultrafast H-atoms elimination also occurs in these systems, which tends to suggest that the $^1\pi\sigma^*$ state is still operative in amino acids.

1.8. Aims and Outlines

As mentioned above, aromatic amino acids, like tyrosine and tryptophan, exhibit fairly low fluorescence quantum yields when the excitation energy exceeds a certain threshold. Tyrosine plays an important role in the catalysis of a variety of enzymes including photosystem II and the water oxidising enzyme¹⁰⁷ and tryptophan is considered an important fluorescence probe in proteins for many spectroscopic investigations.¹⁰⁸ In addition to the above, the processes which involve the absorption of light play a vital role in our daily lives. Our molecular building blocks (for example tyrosine and tryptophan) have been chosen carefully by nature, so that the harmful effects of ultraviolet radiation are by-passed. The chromophores of these building blocks absorb ultraviolet radiation very readily. However, once absorbed, this energy is efficiently diffused through harmless molecular relaxation pathways which reduce the risk of molecular breakdown and therefore photochemical damage. One such pathway involves repulsive $^1\pi\sigma^*$ states. This state exhibits CIs with lower-lying electronic states thus transferring population from the first electronically excited state to the ground state. This relaxation process either directly eliminates neutral H-atoms or leads to vibrationally hot ground state molecules, which diffuse their energy further by IVR or statistical unimolecular decay. In order to help develop our understanding of the role of the $^1\pi\sigma^*$ state, namely to probe the

evolution of this excited state in real-time, time resolved TOF-MS and VMI studies have been performed with these molecules.

State-of-art ultrafast pump-probe spectroscopy was combined with the molecular beams of target molecules, such as phenol, indole, p-ethylphenol, tyramine and tyrosine. Molecular beams of phenol, indole and p-ethylphenol are produced with the help of an Even-Lavie valve but for tyramine and tyrosine modifications have been made to this valve, in order to introduce them into the gas-phase and bypass thermal decomposition. This, along with a detailed description of the generation of ultrafast pump and probe pulses, construction of time-resolved VMI and data acquisition and analysis will be discussed in the following chapter. H-atom elimination in photoexcited phenol with a combination of time-resolved spectroscopy and TOF-MS will be discussed in chapter 3. The results show that the H-atom elimination from photoexcited phenol molecules occurs on a timescale of $103 \text{ fs} \pm 30 \text{ fs}$, confirming that the direct pathways of H-atom elimination is operative, thus implicating the role of a repulsive $\pi\sigma^*$ state.⁷⁹

In chapter 4 the results of time-resolved VMI will be presented. An extra dimension (energy) afforded by VMI enabled us to separate and pin point the various H-atom elimination pathways. The results demonstrate that H-atom elimination corresponding to all kinetic energy ranges (of H-atoms) occurs in $< 150 \text{ fs}$. Once again, this strongly suggests that indirect or statistical pathways of H-atom elimination are inactive.¹⁰⁵

H-atom abstraction from photoexcited (200 nm) indole molecules will be described in chapter 5. Once again, a combination of time-resolved spectroscopy and

VMI again suggests that the H-atom elimination occurs in < 200 fs, resulting in various ranges of H-atom kinetic energies.¹⁰⁶

Chapter 6 will deal with the time-resolved VMI of H-atom elimination from tyrosine and its sub-units, p-ethylphenol and tyramine. For the first time, the H-atom abstraction from tyramine and tyrosine in the gas-phase will be reported. Our results are suggestive of ultrafast H-atom elimination from these important biomolecules, confirming the active role of the $^1\pi\sigma^*$ state.

1.9 References

- (1) Arrhenius, S. *Z. Phys. Chem. (Leipzig)* **1889**, 4, 226.
- (2) Zewail, A. H. *Angew. Chem. Int. Ed.* **2000**, 39, 2586.
- (3) Tolman, R. C. *J. Am. Chem. Soc.* **1925**, 47, 2652.
- (4) Lindemann, F. A. *Trans. Faraday Soc.* **1922**, 17, 598.
- (5) Laidler, K. J. *Chemical Kinetics*, 3rd ed. Harper Collins, New York, **1987**.
- (6) Pross, A. *Theoretical and Physical Principles of Organic Reactivity*, Wiley, New York, **1995**.
- (7) Eyring, H. *J. Chem. Phys.* **1935**, 3, 107.
- (8) Evans, M. G.; Polanyi, M. *Trans. Faraday Soc.* **1937**, 33, 448.
- (9) Zewail, A. H. *Science*, **1988**, 242, 1645.
- (10) Levine, R. D. *Molecular Reaction Dynamics*, Cambridge University Press, **2005**.
- (11) Wayne, C. E.; Wayne, R.P. *Photochemistry*, Oxford University Press, **1996**.
- (12) Atkins, P.; de Paula, J. *Atkins' Physical Chemistry*, 8th ed. Oxford University Press, **2006**.

- (13) Levine, I. N. *Quantum Chemistry*, 4th Ed. Prentice-Hall of India Private Limited, **1995**.
- (14) Hedley, G. J.; Ruseckas, A.; Samuel, I. D. W. *J. Phys. Chem. A* **2009**, *113*, 2.
- (15) Hirst, D. M. *Potential Energy Surfaces: Molecular Structure and Reaction Dynamics*, Taylor and Francis Ltd. London, **1985**.
- (16) Teller, E. *J. Phys. Chem.* **1937**, *41*, 109.
- (17) Naqvi, K. R.; Brown, W. B. *Int. J. Quantum Chem.* **1972**, *6*, 271.
- (18) Worth, G. A.; Cederbaum, L. S. *Chem. Phys. Lett.* **2001**, *338*, 219.
- (19) Atkins, P; Friedman, R. *Molecular Quantum Mechanics*, 4th ed. Oxford University Press, **2007**.
- (20) Zewail, A. H. *J. Phys. Chem. A* **2000**, *104*, 5660.
- (21) Zewail, A. H. *Angew. Chem. Int. Ed.* **2001**, *40*, 4371.
- (22) Zewail, A. H. *Faraday Discuss. Chem. Soc.* **1983**, *75*, 315.
- (23) Khundkar, L. R.; Knee, J. L.; Zewail, A. H. *J. Chem. Phys.* **1987**, *87*, 77.
- (24) Felker, P. M.; Zewail, A. H. *Adv. Chem. Phys.* **1988**, *70*, 265.
- (25) Knee, J. L.; Zewail, A. H. *Spectroscopy* **1988**, *3*, 44.
- (26) Rose, T. S.; Rosker, M. J.; Zewail, A. H. *J. Chem. Phys.* **1988**, *88*, 6672.
- (27) Rose, T. S.; Rosker, M. J.; Zewail, A. H. *J. Chem. Phys.* **1989**, *91*, 7415.
- (28) Zewail, A. H. *Nature*, **2001**, *412*, 279.
- (29) Zewail A. H.; Bernstein R. B. *Chem. Eng. News* **1988**, *66*, 24.
- (30) de Nalda, R.; Durá, J.; García-Vela, A.; Izquierdo, J. G.; González-Vázquez, J; Bañares, L. *J. Chem. Phys.* **2008**, *128*, 244309.
- (31) Vredenburg, A.; Roeterdink, W. G; Janssen, M. H. J. *J. Chem. Phys.* **2008**, *128*, 204311.

- (32) Judith, V.; de Nalda, R.; Alvarez, J.; Izquierdo, J. G.; Amaral, G. A.; Bañares, L. *ChemPhysChem* **2008**, *9*, 1245.
- (33) Crowther, A. C.; Carrier, S. L.; Preston, T. J.; Crim, F. F. *J. Phys. Chem. A* **2008**, *112*, 12081.
- (34) Crowther, A. C.; Carrier, S. L.; Preston, T. J.; Crim, F. F. *J. Phys. Chem. A* **2009**, *113*, 3758.
- (35) Moulton, P. F. *J. Opt. Soc. Am. B* **1986**, *3*, 125.
- (36) Carley, R. E.; Heesel, E.; Fielding, H. H. *Chem. Soc. Rev.* **2005**, *34*, 949.
- (37) Sutter, D. H.; Steinmeyer, G.; Gallmann, L.; Matuscheck, N.; Morier-Genoud, F.; Keller, U.; Scheuer, V.; Angelow, G.; Tschudi, T. *Opt. Lett.* **1999**, *24*, 631.
- (38) Morgner, U.; Kartner, F. X.; Cho, S. H.; Chen, Y.; Haus, H. A.; Fujimoto, J. G.; Ippen, E. P.; Scheuer, V.; Angelow, G. Tschudi, T. *Opt. Lett.* **1999**, *24*, 411.
- (39) Avouris, P.; Gelbart, W. M.; El-sayed, M. A.; *Chem. Rev.* **1977**, *77*, 793.
- (40) Smalley, R. E. *Ann. Rev. Phys. Chem.* **1983**, *34*, 129.
- (41) Fitch, P. S.; Haynman, C. A.; Levy, D. H. *J. Chem. Phys.* **1980**, *73*, 1064.
- (42) Parmenter, C. S. *J. Phys. Chem.* **1982**, *86*, 1735.
- (43) Bondybey, V. E. *Ann. Rev. Phys. Chem.* **1984**, *35*, 591.
- (44) Stewart, G. M.; MacDonald, J. D. *J. Chem. Phys.* **1983**, *78*, 3907.
- (45) Smalley, R. E. *J. Phys. Chem.* **1982**, *86*, 3504.
- (46) Felker, P. M.; Zewail, A. H. *Chem. Phys. Lett.* **1983**, *102*, 113.
- (47) Van der Meer, B. J.; Jonkman, H. T.; Kommandeur, J.; Meerts, W. L.; Majewski, W. A. *Chem. Phys. Lett.* **1982**, *92*, 565.
- (48) Schultz, P. A.; Sudbo, A. S.; Krajnovich, D. J.; Kwok, H. S.; Shen, Y. R.; Lee, Y. T. *Ann. Rev. Phys. Chem.* **1979**, *30*, 379.

- (49) Ashfold M. N. R.; Baggott, J. E. *Advances in Gas-Phase Photochemistry and Kinetics: Molecular Photodissociation Dynamics*, The Royal Society of Chemistry, **1987**.
- (50) Imre, D.; Kinsey, J. L.; Sinha, A.; Krenos, J. J. *J. Phys. Chem.* **1984**, *88*, 3956.
- (51) Moore, C.B. *J. Chem. Phys.* **1985**, *83*, 4476.
- (52) Moore, C. B.; Weisshaar, J. C. *Ann. Rev. Phys. Chem.* **1983**, *34*, 525.
- (53) Bamford, D. J.; Filseth, S. V.; Foltz, M. F.; Hepburn, J. W.; Moore, C. B. *J. Chem. Phys.* **1985**, *82*, 3032.
- (54) Andresen, P.; Ondrey, G. S.; Titze, B.; Rothe, E. W. *J. Chem. Phys.* **1984**, *80*, 2546.
- (55) Levy, D. H. *Science* **1981**, *214*, 263.
- (56) Miller, T. A. *Science* **1984**, *223*, 545.
- (57) Scoles, G. *Atomic and Molecular Beam Methods*. Oxford University Press, **1988**.
- (58) Abad, L.; Bermejo, D.; Herrero, V. J.; Santos, J.; Tanarro, I. *Rev. Sci. Instrum.* **1995**, *66*, 3826.
- (59) Even, U.; Jortner, J.; Noy, D.; Lavie, N.; Cossart-Magos, C. *J. Chem. Phys.* **2000**, *112*, 8068.
- (60) Willberg, D. M.; Gutmann, M.; Breen, J. J.; Zewail, a. H. *J. Chem. Phys.* **1992**, *96*, 198.
- (61) Motzkus, M.; Pedersen, S.; Zewail, A. H. *J. Phys. Chem.* **1996**, *100*, 5620.
- (62) Rosker, M. J.; Dantus, M.; Zewail, A. H. *J. Chem. Phys.* **1988**, *89*, 6113.
- (63) Herek, J. L.; Pedersen, S.; Banares, L.; Zewail, A. H. *J. Chem. Phys.* **1992**, *97*, 9046.

- (64) Dantus, M.; Bowman, R. M.; Gruebele, M.; Zewail, A. H. *J. Chem. Phys.* **1989**, *91*, 7437.
- (65) Gardner, J. L.; Miller, S. M.; *J. Chem. Phys.* **2004**, *121*, 5920.
- (66) Koopmans, von T. *Physica (Elsevier)* **1934**, *1*, 104.
- (67) Hockett, P.; Staniforth, M.; Reid, K. L. *Phys. Rev. Lett.* **2009**, *102*, 253002.
- (68) Reid, K. L. *Int. Rev. Phys. Chem.* **2008**, *27*, 607.
- (69) Wang, X.-B.; Chi, C.; Zhou, M.; Kuvychko, I. V.; Seppelt, K.; Popov, A. A.; Strauss, S. H.; Boltina, O. V.; Wang, L.-S. *J. Phys. Chem. A* **2010**, *114*, 1756.
- (70) Copeland, G.; Lee, E. P. F.; Dyke, J. M.; Chow, W. K.; Mok, D. K. W.; Chau, F. T. *J. Phys. Chem. A* **2010**, *114*, 1816.
- (71) Johnson, P. M. *Appl. Opt.* **1980**, *19*, 3920.
- (72) van der Weil, M. *J. Chim. Phys. Phys.-Chim. Biol.* **1980**, *77*, 647.
- (73) Antonov, V. S.; Letokhov, V. S. *Appl. Phys.* **1981**, *24*, 89.
- (74) Schlag, E. W.; Neusser, H. J. *Acc. Chem. Res.* **1983**, *16*, 355.
- (75) Bernstein, R. B. *J. Phys. Chem.* **1982**, *86*, 1178.
- (76) Ashfold, M. N. R. *Mol. Phys.* **1986**, *58*, 1.
- (77) Johnson, P. M.; Otis, C. E. *Annu. Rev. Phys. Chem.* **1981**, *32*, 139.
- (78) Johnson, P. M. *Acc. Chem. Res.* **1980**, *13*, 20.
- (79) Iqbal, A.; Pegg, L.-J.; Stavros, V. G. *J. Phys. Chem. A* **2008**, *112*, 9531.
- (80) Lin, S. H.; Fujimura, Y.; Neusser, N. J.; Schlag, E. W. *Multiphoton Spectroscopy of Molecules*. Academic Press Inc., **1984**.
- (81) Reed, C. L.; Kono, M.; Langford, S. R.; Hancock, T. W. R.; Dixon, R. N.; Ashfold, M. N. R. *J. Chem. Phys.* **1997**, *106*, 6198.
- (82) Langford, S. R.; Batten, A. D.; Kono, M.; Ashfold, M. N. R. *J. Chem. Soc.*

- Faraday Trans.* **1997**, *93*, 3757.
- (83) Cook, P.A.; Langford, S. R.; Ashfold, M. N. R.; Dixon, R. N. *J. Chem. Phys.* **2000**, *113*, 994.
- (84) Cook, P.A.; Langford, S. R.; Dixon, R. N.; Ashfold, M. N. R. *J. Chem. Phys.* **2001**, *114*, 1672.
- (85) Qadiri, R. H.; Feltham, E. J.; Cottrill, E. E. H.; Taniguchi, N.; Ashfold, M. N. R. *J. Chem. Phys.* **2002**, *116*, 906.
- (86) Cook, P. A.; Jimeno, P.; Ashfold, M. N. R.; Balint-Kurti, G. G.; Dixon, R. N. *Phys. Chem. Chem. Phys.* **2002**, *4*, 1513.
- (87) Feltham, E. J.; Qadiri, R. H.; Cottrill, E. E. H.; Cook, P. A.; Cole, J. P.; Balint-Kurti, G. G.; Ashfold, M. N. R. *J. Chem. Phys.* **2003**, *119*, 6017.
- (88) Cronin, B.; Nix, M. G. D.; Qadiri, R. H.; Ashfold, M. N. R. *Phys. Chem. Chem. Phys.* **2004**, *6*, 5031.
- (89) Nix, M. G. D.; Devine, A. L.; Cronin, B.; Ashfold, M. N. R. *Phys. Chem. Chem. Phys.* **2006**, *8*, 2610.
- (90) Nix, M. G. D.; Devine, A. L.; Cronin, B.; Dixon, R. N.; Ashfold, M. N. R. *J. Chem. Phys.* **2006**, *125*, 133318.
- (91) Devine, A. L.; Cronin, B.; Nix, M. G. D.; Ashfold, M. N. R. *J. Chem. Phys.* **2006**, *125*, 184302.
- (92) Ashfold, M. N. R.; King, G. A.; Murdock, D.; Nix, M. G. D.; Oliver, T. A. A.; Sage, A. G. *Phys. Chem. Chem. Phys.* **2010**, *12*, 1218.
- (93) Lin, C.-K.; Huang, C.-L.; Jiang, J.-C.; Chang, A. H. H.; Lee, Y. T.; Lin, S. H.; Ni, C.-K. *J. Am. Chem. Soc.* **2002**, *124*, 4068.
- (94) Tsai, S.-T.; Lin, C.-K.; Lee, Y. T.; Ni, C.-K. *Rev. Sci. Instrum.* **2001**, *72*, 1963.

- (95) Tsai, S.-T.; Lin, C.-K.; Lee, Y. T.; Ni, C.-K. *J. Chem. Phys.* **2000**, *113*, 67.
- (96) Creed, D. *Photochem. Photobiol.* **1984**, *39*, 563.
- (97) Creed, D. *Photochem. Photobiol.* **1984**, *39*, 537.
- (98) Crespo-Hernández, C. E.; Cohen, B.; Hare, P. M.; Kohler, B. *Chem. Rev.* **2004**, *104*, 1977.
- (99) Tseng, C.-M.; Lee, Y. T.; Ni, C.-K.; Chang, J.-L. *J. Phys. Chem. A* **2007**, *111*, 6674.
- (100) Sobolewski, A. L.; Domcke, W.; Dedonder-Lardeux, C.; Jouvet, C. *Phys. Chem. Chem. Phys.* **2002**, *4*, 1093.
- (101) Tseng, C.-M.; Lee, Y. T.; Ni, C.-K.; *J. Chem. Phys.* **2004**, *121*, 2459.
- (102) Lin, M.-F.; Tseng, C.-M.; Lee, Y. T.; Ni, C.-K. *J. Chem. Phys.* **2005**, *123*, 124303.
- (103) Nix, M. G. D.; Devine, A. L.; Cronin, B.; Dixon, R. N.; Ashfold, M. N. R. *J. Chem. Phys.* **2006**, *125*, 133318.
- (104) Nix, M. G. D.; Devine, A. L.; Cronin, B.; Ashfold, M. N. R. *Phys. Chem. Chem. Phys.* **2006**, *8*, 2610.
- (105) Iqbal, A.; Cheung, M. S. Y.; Nix, M. G. D.; Stavros, V. G. *J. Phys. Chem. A* **2009**, *113*, 8157.
- (106) Iqbal, A.; Stavros, V. G. *J. Phys. Chem. A* **2010**, *114*, 68.
- (107) Barry, B. A.; Eldeeb, M. K.; Sandusky, P. O.; Babcock, G. T. *J. Biol. Chem.* **1990**, *265*, 20139.
- (108) Lakowicz, J. R. *Principles of Fluorescence Spectroscopy*, 2nd ed. Plenum, New York, **1999**.

Chapter 2

Experimental Techniques

The experimental section begins with a description of how the pump and probe pulses are generated which includes; how the fundamental 800 nm beam is frequency up-converted through a series of non-linear crystals to generate the correct pump/probe wavelengths; and how these two pulses are collinearly aligned to obtain temporal overlap (time zero) with the molecular beam. This section then describes molecular beam generation in phenol, indole, p-ethylphenol, tyramine and tyrosine. Calibration of the time-of-flight mass spectrometer (TOF-MS) and velocity map imaging (VMI) detector with a brief theoretical description of anisotropy related to the H^+ images is presented. In addition, in order to perform time-resolved VMI measurements details about synchronization amongst various parts of the experimental setup are given. The experimental chapter ends by describing the processing of raw images of H^+ with the help of a polar onion peeling (POP) programme developed by Dr. Jan Verlet's group at Durham University together with a description of the data acquisition using a homebuilt LabVIEW programme.

2.1. Pump-probe Setup

A Spectra-Physics Tsunami laser, based on a Kerr-lens mode-locked Ti:sapphire oscillator, produces pulses of approximately 5 nJ/pulse, centred at 800 nm

at a repetition rate of 80 MHz. A continuous-wave (CW) solid-state laser (Millenia Pro) is used to pump this oscillator with 4 W at 532 nm. The pulse train generated by the Tsunami are fed to a commercially available regenerative amplifier (Spectra-physics, Spitfire Pro XP). The amplifier produces 35 fs long pulses centred at 800 nm at a repetition rate of 1 kHz with an output power of 3 W (3 mJ/pulse). The optical bandwidth is $\sim 470 \text{ cm}^{-1}$. Figure 2.1 presents a simplified layout of the setup which includes the path of both the pump (200 nm) and probe (243.1 nm) pulses, coupled with the molecular beam. The molecular beam apparatus consists of a source chamber that houses the Even-Lavie valve and an interaction chamber that contains the ion optics and the VMI detector together with CCD camera and its detailed description will be given shortly.

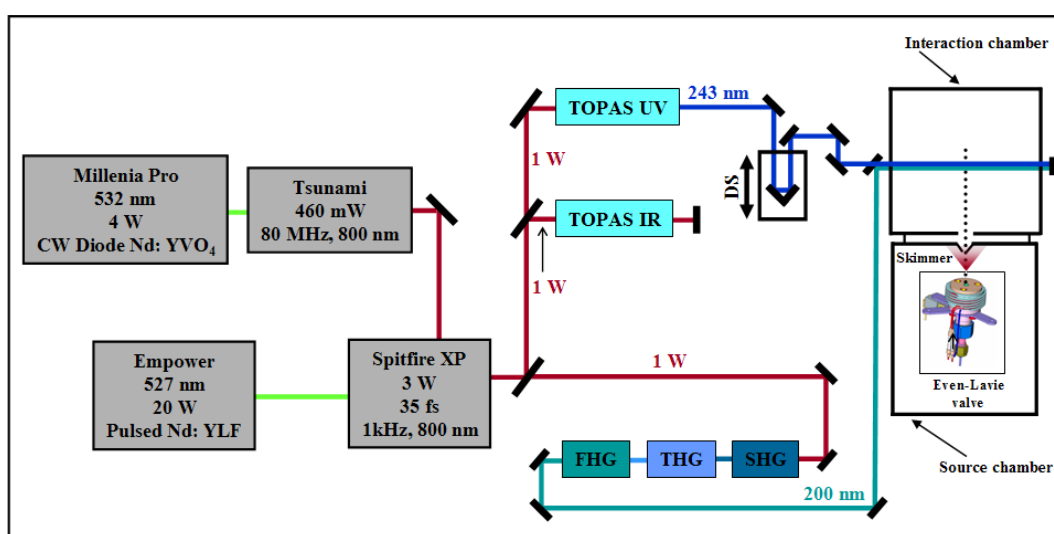


Figure 2.1 Schematic of laser setup (LHS) in conjunction with molecular beam (RHS). DS represents a motorised delay stage that moves to and fro as shown by double headed arrow to delay the probe beam with respect to the pump beam. SHG, THG and FHG represent the 2nd, 3rd and 4th harmonic generating crystals, respectively. The source and interaction chambers house the Even-Lavie valve and VMI setup (for illustration see figure 2.9) respectively.

2.1.1. Generation of Pump and Probe Pulses

The output from the amplifier is divided into three beams of equal intensity by using beam-splitters. Two optical parametric amplifiers (OPA, TOPAS C, light conversion) are pumped by two of these beams, each of 1 mJ/pulse, one of which is used to create pulses in the infrared (IR) and has not been used in the current experiments. The other produces pulses in the UV, typically set at 243.1 nm with pulse energies of 6-7 μJ /pulse. These probe pulses (243.1 nm) are used to ionize resonantly the H-atoms via (2 + 1) REMPI. As the full description of time-resolved H-atom elimination will be discussed in the proceeding paragraphs, for the sake of illustrative purposes, when the molecular beam of a target molecule is intercepted by the lasers pulses, H-atoms are eliminated and detected by probe pulses at 243.1 nm, as shown in figure 2.2.

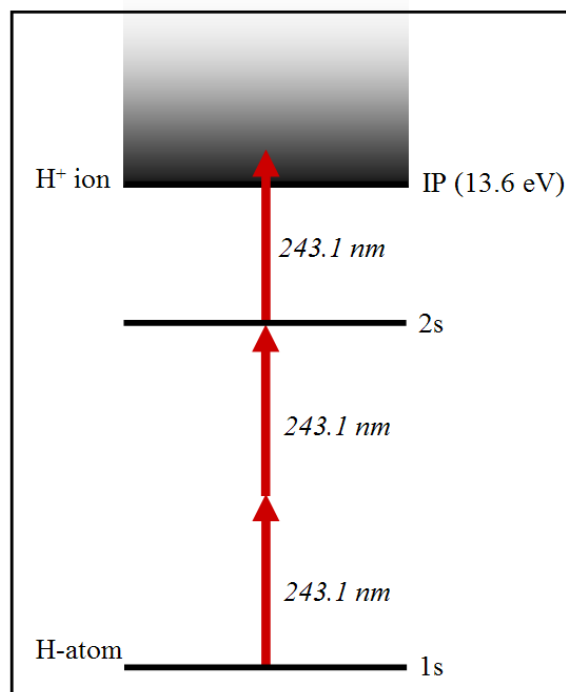


Figure 2.2 (2 + 1) REMPI mechanism of H-atom. Two photons of 243.1 nm excites the H-atom to its 2s state and third photon ionizes it, thus generating H⁺ ion.¹

The third part of the fundamental 800 nm beam is directed toward a series of non-linear, type-I, type-II and type-I BBO ((Beta Barium Borate (β -BaB₂O₄)) crystals. The 2nd harmonic (400 nm) is produced by frequency doubling the fundamental 800 nm with the help of a type I BBO crystal. The 3rd harmonic (266 nm) is generated by mixing the 400 nm with the residual 800 nm by a type II BBO crystal, and the 4th (200 nm, 1 μ J/pulse) harmonic is produced by mixing the 266 nm and residual 800 nm in a type I BBO crystal. By changing the temporal overlap between the 266 nm and 800 nm pulses using a manual translation stage included in the 800 nm beam path, one is able to optimize the 200 nm radiation. Both 266 nm and 200 nm are used as pump pulses in these experiments. The probe beam (243.1 nm) follows an optical path that includes a computer controlled delay stage (Physik-Instrumente), as shown in figure 2.1, to change the optical path length it traverses, thereby changing the temporal delay between the pump and probe pulses. This motor controlled delay stage is operated with the help of a program written in LabVIEW 8.6. A delay movement of 1 μ m corresponds to a temporal delay of \sim 6.67 fs.

2.1.2. Nonlinear Optical Harmonics Generation

As described above, when the fundamental 800 nm is passed through a BBO crystal it doubles in frequency. This is because of the fact that the electric field of light induces dielectric polarization in the medium. When a medium is subjected to a strong electric field of electromagnetic radiation, the nonlinear effects can be described by the following equation,

$$P = \varepsilon_0(\chi^{(1)}E + \chi^{(2)}E^2 + \dots) \quad (2.1)$$

P , ε_0 , χ and E are the dielectric polarization of the medium, electric permittivity of free space, nonlinear susceptibility of the medium and the electric field of electromagnetic radiation, respectively. If the electric field of electromagnetic radiation is represented by $E = E_0 \sin(\omega t)$, where ω is the frequency of oscillating electromagnetic radiation field, substituting this in equation (2.1) will result in the following equation.

$$P = \varepsilon_0 \chi^{(1)} E_0 \sin(\omega t) + \varepsilon_0 \chi^{(2)} E_0^2 \sin^2(\omega t) + \dots \quad (2.2)$$

Equation (2.2) can be further expanded to equation (2.3) by substituting the trigonometric relations. As can be seen by the second term in this expression, the incident frequency is doubled after passing through a birefringent material i.e. a BBO crystal.

$$P = \varepsilon_0 \chi^{(1)} E_0 \sin(\omega t) + \frac{1}{2} \varepsilon_0 \chi^{(2)} E_0^2 \{1 - \cos(2\omega t)\} + \dots \quad (2.3)$$

Birefringent materials of this type normally do not have an inversion centre, for example BBO and KDP (Potassium dihydrogen phosphate (KH_2PO_4)) crystals. When the electromagnetic waves interact with these crystals, it induces an electric dipole that oscillates with double the frequency as compared to the incident radiation, thus the emitted frequency is doubled and is represented by 2ω . At higher electric field strengths, the higher order terms in equation (2.3) increase, resulting in higher order harmonic generation.²

Nonlinear harmonic generation and nonlinear mixing with the help of type I and type II BBO crystals enables us to generate 400 nm, 266 nm and 200 nm. The purpose of frequency up-conversion here is to generate 266 nm and 200 nm pump pulses to study the dynamics of biomolecules of interest. Conventionally, the polarizations of these wavelengths are named as ordinary and extraordinary. Normally crystals have three axes, one or two of which have different refractive indices than the other. The uniaxial BBO crystal that has a preferred axis is called the extraordinary (e) axis, while the other two are called the ordinary (o) axes. The sum of the output light wave frequencies is equal to the input frequency. The two output frequencies are termed as “signal” and “idler”, where the output wave with the lower frequency is called the idler and the output wave with higher frequency is called the signal. If the signal and idler have the same polarizations, the crystal is termed a type I crystal and if their polarizations are perpendicular it is said to be a type II crystal. Table 2.1 represents the polarizations of various harmonics generated in the current setup.

Wavelength	Harmonic	Crystal Type	Polarization
800 nm	Fundamental	—	Ordinary
400 nm	2 nd	BBO Type I	Extraordinary
266 nm	3 rd	BBO Type II	Ordinary
200 nm	4 th	BBO Type I	Extraordinary

Table 2.1 Crystal types generating various harmonics and their respective polarizations.

2.1.3. Temporal Overlap of Pump-probe Pulses

Both the pump and probe pulses are focussed separately via 500 mm focal length lenses before entering the vacuum chamber. The output of the probe beam from the OPA has a diameter of 3 mm. Since probing the H-atom requires three photons to ionize it, the intensity of the probe needs to be as high as possible. As a result, tight focussing is needed. The diameter of the probe is therefore increased to 8 mm by using a Galilean telescope. Equation (2.4) establishes a relationship between initial beam diameter and the diameter of the beam at the focus,

$$d_F = \frac{4\lambda F}{\pi d_i} \quad (2.4)$$

d_F , λ , F and d_i are the beam diameter at the focal length, wavelength of the laser, focal length of the lens and the initial beam diameter at the lens, respectively. Equation (2.4) suggests an inverse relationship between the beam diameter at the focus and initial beam diameter.

Equation (2.5) gives the relationship between laser beam intensity and focal area and can be expressed as follows,

$$I = \frac{P}{A} \quad (2.5)$$

here I , P and A represents the laser beam intensity, measured laser power and focal area, respectively. In these experiments, the pump (200 nm) beam has an initial diameter of ~0.3 cm and then from equation (2.4) the diameter at the focus is ~4.246

$\times 10^{-3}$ cm and covers an area of $\sim 1.415 \times 10^{-5}$ cm². The probe (243.1 nm) beam has an initial diameter of ~ 1 cm; the diameter at the focus is $\sim 1.548 \times 10^{-3}$ cm and covers an area of $\sim 1.882 \times 10^{-6}$ cm². Accordingly, by assuming pulse durations ~ 100 fs the intensities of 200 nm (1 μ J/pulse) and 243.1 nm (6.5 μ J/pulse) can be calculated with the help of equation (2.5) and correspond to $\sim 7.067 \times 10^{11}$ Wcm⁻² and 3.454×10^{13} Wcm⁻² respectively.

Both the pump and probe beams are spatially overlapped using a dichroic beam splitter. Prior to entering the vacuum chamber, both beams are roughly aligned through a 50 μ m pinhole outside of the vacuum chamber with the help of a removable silver mirror directly in front of the entrance window of the chamber. Following this, the mirror is removed and the two beams enter the vacuum chamber. The pump pulse excites the target molecules that eliminate H-atoms and the probe pulse ionizes these and gives the H⁺ yield as function of pump-probe delay. The H⁺ transients are fit using a numerical procedure discussed shortly which enables timescales of the relevant processes involved in the dynamics to be extracted.

2.2. Vacuum Chamber

After spatially overlapping outside of vacuum, both the pump and probe pulses are sent into the vacuum chamber through a CaF₂ window, where they intercept a molecular beam of target molecules. The vacuum chamber is shown in figure 2.3. The source chamber holds the Even-Lavie valve that produces the molecular beam. This chamber is separated from the interaction chamber by a 2 mm skimmer. The interaction chamber houses the TOF ion optics to accelerate the ions that are generated by photo-ionization towards the microchannel plate (MCP)

detector that is situated at the end of the flight tube (approximately 50 cm). To detect the photo-products and their evolution in real time, two detection schemes are used. One is time-resolved time-of-flight mass spectroscopy (TOF-MS) and the other is time-resolved velocity map ion imaging (VMI). Both these techniques will be discussed in detail in the following paragraphs.

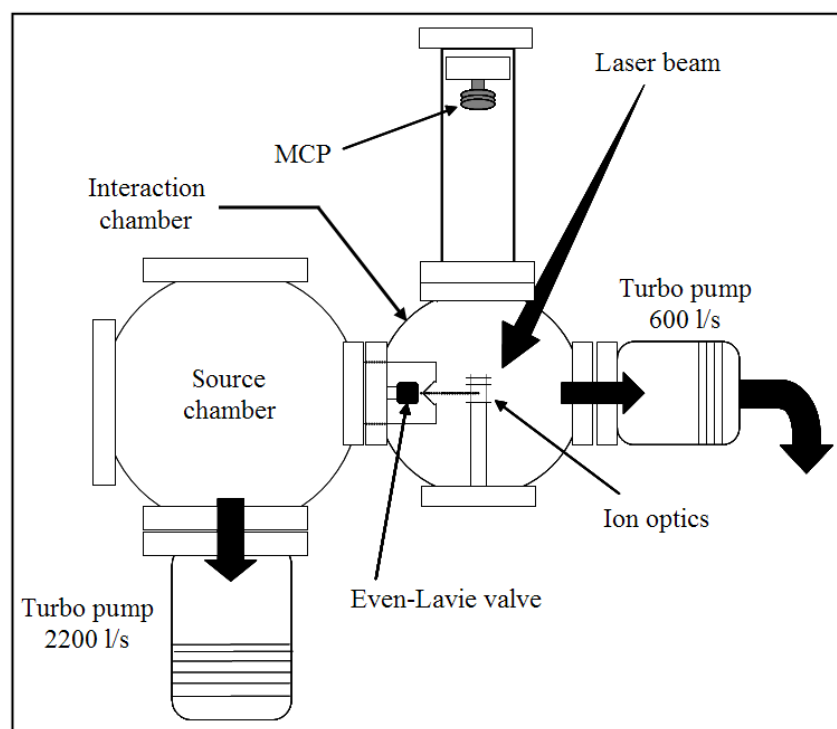


Figure 2.3 The vacuum chamber comprises of source and interaction chambers. The source chamber holds the Even-Lavie valve and the interaction chamber contains the TOF-MS and VMI setup. The MCP at the terminus of the flight tube can be replaced by the VMI detector (MCPs coupled with a phosphor screen) according to the measurements needed.

The source chamber is connected to a turbo pump (Leybold Vacuum Trivac, 2200 l/s) to pump the chamber. The interaction chamber is connected to a smaller turbo pump (Leybold Vacuum Trivac, 600 l/s). The interaction region is pumped by this small vacuum pump and provides a sufficient pressure difference between itself

and the source chamber such that the detector (either MCP or VMI) can operate safely. Typical pressures in the source and interaction chambers when the pulsed valve is off are in the range of 1×10^{-7} mbar and 1×10^{-8} mbar, respectively. During experiments, the pressure increase in the interaction chamber ranges from 2×10^{-7} - 5×10^{-7} mbar, while in the source region this increase ranges from 2×10^{-6} - 5×10^{-6} mbar.

2.2.1. Even-Lavie Valve and Molecular Beam

As mentioned above, the Even-Lavie valve³ is used to generate the molecular beam. The Even-Lavie valve is a solenoid valve and is operated by a high current pulse (500 A) that is discharged through an electrolytic 600 μ F capacitor. The capacitor is first charged to 100 V and then discharged in 20 μ s. A magnetic field of 2.5 T is created at the centre of the plunger due to the high current, pulling the plunger back with a force of ~ 10 N. This generates a backward acceleration covering a distance of 0.1 mm in 8 μ s, which is then returned to the sealing position with the help of spring. In this way, this valve can be operated constantly at a repetition rate of 1 kHz with backing pressures of up to 100 bars and an operating temperature up to 250 °C. The very short opening time of the front nozzle produces a very cold and intense molecular beam in the interaction region. The short packet of the gas pulse seeded in He is 15 mm long and can be detected within a laser timing ~ 1 μ s. The gas packet's velocity can be calculated directly by taking the difference of valve opening time and laser firing. For example for He at 37 °C this corresponds to 1780 ± 20 m/s.²

In these experiments, if the valve is operated synchronously with the laser system at a repetition rate of 1 kHz, with an opening time of 14 μs the measured FWHM is approximately 60 μs , as presented in figure 2.4. This figure shows the normalized phenol ion signal as a function of opening time (delay time) of the valve with respect to the laser pulse at a backing pressure of 2 bar of He, at 70 °C. The purpose of this figure is solely to show how the opening time of the valve was optimised with respect to the laser pulse to obtain the maximum ion signal.

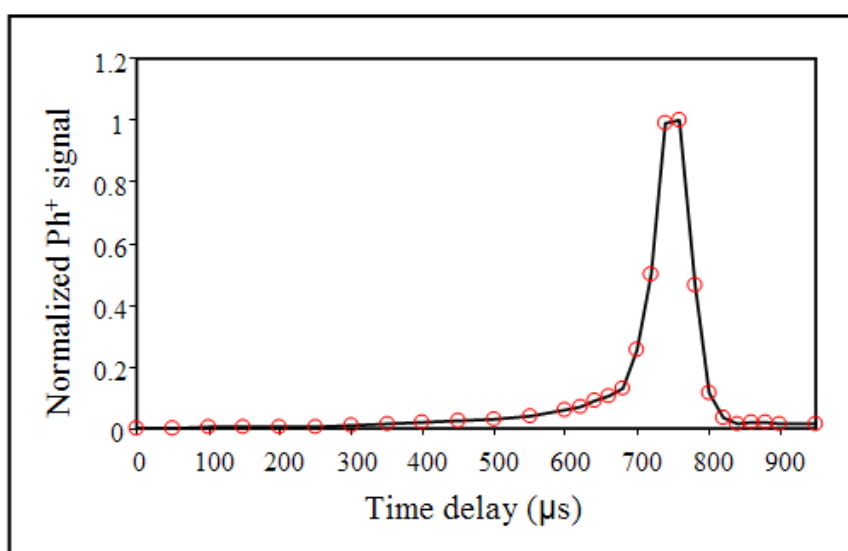


Figure 2.4 Measured pulse width $\sim 60 \mu\text{s}$, with a backing pressure of 2 bar of He.

2.2.1.1. Molecular Beam of Phenol, Indole and p-Ethylphenol

Phenol-h6 (Fluka, $\geq 99.5\%$), phenol-d5 (Sigma-Aldrich, Phenol-2, 3, 4, 5, 6-d5, 98 atom % D), indole (Sigma-Aldrich, indole $\geq 99\%$) and p-ethylphenol (Aldrich, 4-ethylphenol $\geq 99\%$) were purchased from Sigma-Aldrich and used without any further purification. The solid samples of these molecules were packed into the cartridge that is shown in figure 2.5 (a). After disassembling the cartridge

assembly a small piece of glass filter paper was placed directly behind the sintered filter at the exit gas feed. This prevents droplets of sample entering the mechanism of the valve through the front sinters. All these biomolecules (phenol, indole and p-ethylphenol) are low melting point solids and when the valve is operated at 14 μ s, it heats up to 70 $^{\circ}$ C due to the resistance across the coil. As a result, glass filter paper is used which can tolerate high temperatures. Typical operating hours for a sample weighing 4-5 mg is around 20-30 hours which translates to around two days of experimental time. Table 2.2 gives the information about the particular biomolecule's melting and boiling points together with their molecular weights. One interesting feature displayed by the table is that as the ethyl (p-ethylphenol) group is replaced by ethylamine (tyramine) at the para-position of the phenol chromophore, the difference between melting and boiling points drastically drops which may be indicative of decomposition at elevated temperatures.

Biomolecules	Melting point ($^{\circ}$ C)	Boiling point ($^{\circ}$ C)	Mol. weight (g/mole)
Phenol-h6	40-42	~182	94.11
Phenol-d5	40-42	~180	99.15
p-Ethylphenol	40-42	218-219	122.16
Indole	52-54	253-254	117.15
Tyramine	160-162	175-181	137.18
Tyrosine	~300	—	181.19

Table 2.2 Presents the melting points, boiling points and molecular weights of biomolecules of interest.

2.2.1.2. Molecular Beam of Tyramine

Tyramine (Aldrich, $\geq 99\%$) was also purchased from Sigma-Aldrich and used without further purification. The molecular beam of tyramine or 4-(2-aminoethyl) phenol was produced differently as compared to phenol, p-ethylphenol and indole. The amino acids and some of their derivatives which include amino groups are very fragile compounds and decompose by heating, especially when metal crucibles are used for heating. To avoid this problem a pipette type quartz tube was designed and fitted inside the cartridge, to hold the tyramine sample. Figure 2.5 (a) represents the cartridge assembly and figure 2.5 (b) presents the quartz pipette type tube.

After packing the sample in the quartz tube, it is fitted inside the cartridge and after mounting the cartridge assembly behind the valve, it is heated to $165\text{ }^{\circ}\text{C}$ in order to obtain enough vapour pressure of tyramine molecules inside the chamber. The valve opening time was again kept at $14\text{ }\mu\text{s}$, operating at 500 Hz synchronously with the laser. In this way the molecular beam of tyramine was generated. Interestingly, previous work by Tseng et al.⁴ on tyramine using multimass ion-imaging failed to observe H-atom elimination, following excitation at 248 nm . However, the experiments performed here adopting the above mentioned approach for the production of a molecular beam of tyramine, following excitation at 200 nm , shows that H-atom elimination is observed, the results of which will be reported in chapter 6.

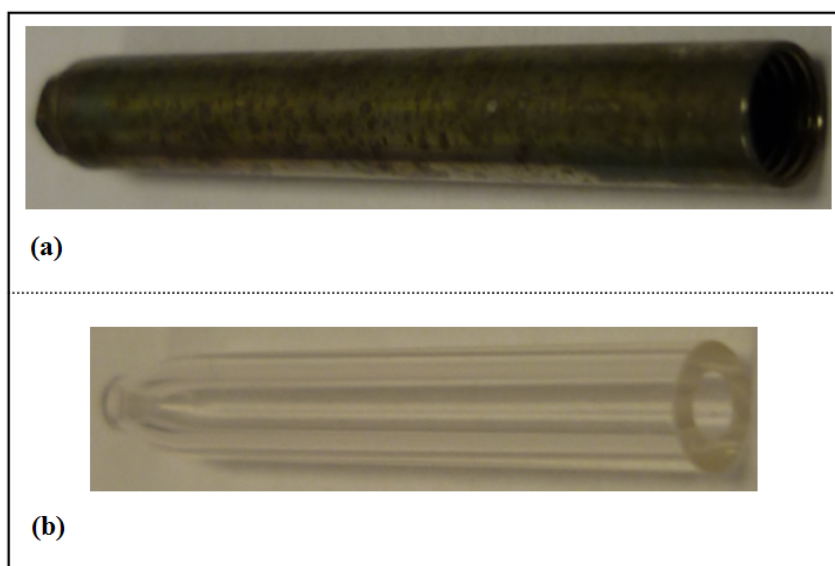


Figure 2.5 Pictorial presentations of (a) valve's cartridge assembly and (b) quartz pipette type tube to hold the tyramine sample.

2.2.1.3. Molecular Beam of Tyrosine

The ultimate target of this research project was to begin investigating H-atom elimination in the amino acid tyrosine. As such, it is very important to produce a molecular beam of tyrosine. Unfortunately, a molecular beam of tyrosine could not be produced as in phenol, indole and tyramine as this led to significant decomposition of the amino acid, as typified by the extensive fragmentation observed in the TOF-MS. An alternative approach was therefore sought. L-tyrosine (reagent grade, Aldrich, $\geq 98\%$) was purchased from Sigma-Aldrich and was used without any further treatment. To put tyrosine into the gas-phase, a brass holder was designed and attached to the front plate of the Even-Lavie valve. A borosilicate glass cell with small lips on both sides was fitted inside this brass holder. The purpose of the brass holder was to hold the glass cell in position and due to its high thermal conductivity to heat the glass cell to high enough temperatures and provide sufficient

vapour pressure of tyrosine to be picked up by the seed gas exiting the valve. A paste of tyrosine was obtained in methanol and pasted inside the walls of the glass cell. To evaporate off the methanol, the valve was heated up to 150 °C outside the vacuum chamber for 10 minutes. After evaporating the methanol the valve was reinserted inside the source chamber. The distance of the mounted glass cell and brass holder was approximately 2 cm from the skimmer. Figure 2.6 (a) shows the brass holder and the glass cell mounted in front of the valve. Figure 2.6 (b) shows both the brass holder and glass cell when dismantled. The length of the brass holder was approximately 18 mm and a glass cell was ~16 mm. The internal diameter of the brass holder was ~14 mm and corresponds to the outer diameter of glass cell providing a snug fit and ensuring maximum surface contact between the glass cell and the brass holder and hence heat transfer. The length of this assembly was kept as short as possible so that the pasted tyrosine sample inside the glass cell can be heated efficiently.

After placing the valve assembly back into vacuum, the valve was heated slowly in steps of 5 °C up to 250 °C. The opening time of the valve was 14 μ s. The backing pressure of He was increased to 5 bars. The delay between valve and laser was altered to maximise the parent tyrosine ion signal (Tyr^+). The data obtained with this modified setup will be presented in chapter 6. Figure 2.6 (c) and figure 2.6 (d) show pictures taken of a fresh sample of tyrosine and used sample of tyrosine taken from the glass cell after two days of experimental measurements at 250 °C, respectively. It is quite clear from figure 2.6 (d) that the tyrosine sample has not decomposed; its physical appearance looking very similar to the unused sample. This is in stark contrast to the earlier measurements in which tyrosine was packed directly

inside the cartridge without and even with the quartz tube (as with tyramine). In this case, the tyrosine had turned dark brown/black indicative of decomposition.

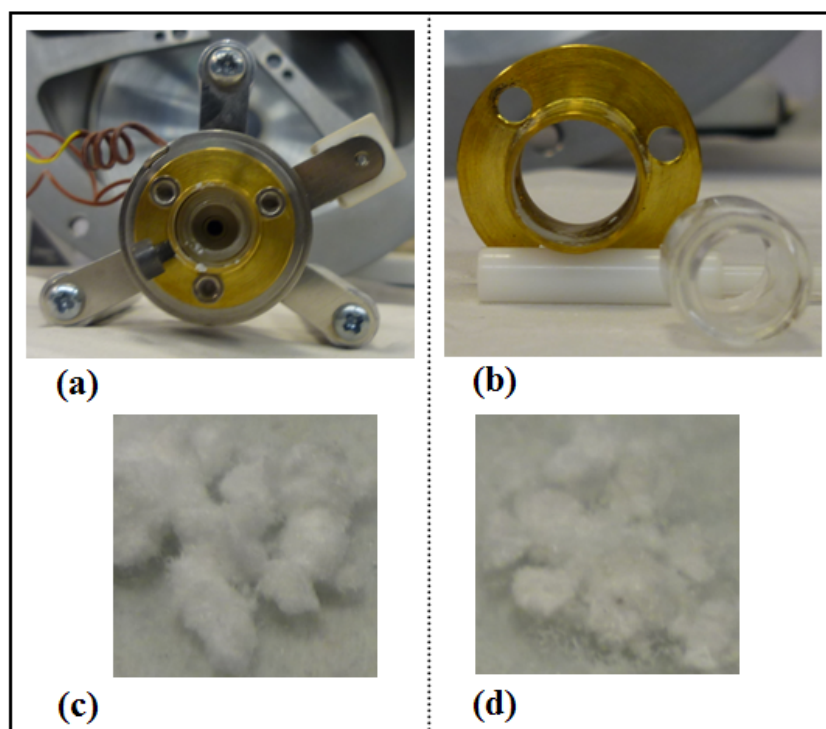


Figure 2.6 Pictures of brass holder and borosilicate cell, (a) both brass holder and glass cell are attached in front of the valve nozzle (b) when both are demounted, (c) represents the unused tyrosine sample and (d) shows the picture of used tyrosine sample.

2.3. Time-of-Flight Mass Spectroscopy

When the molecular beam is intercepted by the pump and probe laser pulses, a range of fragment ions (including the parent molecular ion) are generated either through resonant or non-resonant ionization. The ions are detected by TOF-MS. A detailed treatment of the theory behind this experimental technique is provided by Wiley and McLaren.^{5,6} In this technique a static electric field is used to accelerate the ions through a field free tube which are then detected by a detector (e.g. MCP). The

basic principle of this method is to measure the mass-to-charge number ratio (m/z) of all ions.

When a charged particle is subjected to an electro-static field with a voltage V , its potential energy is converted to kinetic energy as it enters the time-of-flight (TOF) tube. Mathematically this can be expressed as follows,

$$qV = \frac{1}{2}mv^2 \quad (2.6)$$

in equation (2.6), q and V represents the charge of the ion and the applied potential difference, respectively. Since the velocity of the ion can be calculated in the TOF tube having length l and as V depends on instrument settings and is a constant (applied voltages will be given in later paragraphs), equation (2.6) can be expressed as,

$$t = \alpha \sqrt{\frac{m}{q}} \quad (2.7)$$

α is related to the instrument settings and its characteristics (applied voltage (V) and length (l) of flight tube), while m and q are the mass and charge of the ion, respectively. For a singly charged ion its TOF is proportional to the square-root of its mass. In essence, different masses with the same charge are accelerated to different velocities under static electric field conditions, and travel with different times toward the detector.

2.3.1. Calibration of Time-of-Flight Mass Spectrum

Since the singly charged ions can be separated according to their mass, so TOF-MS can be calibrated by using a known mass to predict the unknown mass and

its arrival time at the particular voltages applied on the several plates of the TOF-MS setup and is shown in figure 2.7. The Ammonia ion signal (NH_3^+) is used for calibration because it is a gas and it is easy to put in vacuum with the help of the Even-Lavie valve. If the arrival time of NH_3 is measured, then the TOF of the molecular (or fragment) ion of interest can be calculated. The following equation is used to calculate the mass of an unknown ion.

$$m_2 = \left(\frac{t_2 - t_{laser}}{t_{ref} - t_{laser}} \right)^2 \cdot m_{ref} \quad (2.8)$$

In equation (2.8), m_2 , m_{ref} , t_2 , t_{ref} and t_{laser} are the molecular mass of unknown, molecular mass of reference (NH_3), TOF for unknown, TOF of reference and time of arrival of laser pulse. Figure 2.7 presents the assembly of the TOF optics specifying the voltages on different optics used. The voltages applied to the accelerator, repeller and ground electrodes are 5000 V, 2920 V and 0 V, respectively. To optimize and therefore arrive at these voltages, the NH_3^+ signal was monitored on an oscilloscope and the voltages on the repeller and accelerator altered to give the narrowest TOF peak corresponding to the best temporal focusing conditions. The optimized voltages are shown in figure 2.7, the ratio between the repeller and accelerator voltages being ~ 0.584 . The ion signal intensity was detected by a MCP and recorded with the help of an oscilloscope (LeCroy Waverunner LT372) or a multichannel scalar (Stanford, SR430). The data accumulated by a single TOF scan or a series of TOF scans at given pump-probe delays is transferred via a general purpose interface bus to a computer running an acquisition programme written in LabVIEW 8.6.

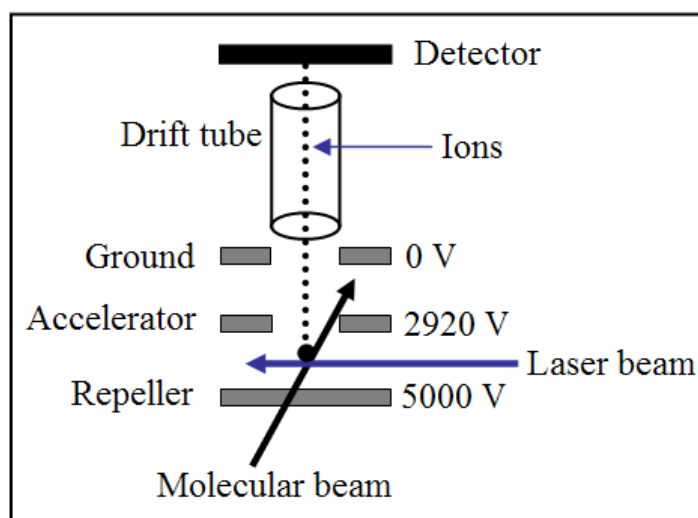


Figure 2.7 TOF-MS setup. As the collinearly aligned laser beams intercept the molecular beam, ions are generated. The ions are then accelerated towards the detector.

2.4. Instrument Response Function and Time Zero

Time resolution in these experiments is dictated by the cross correlation of the pump and probe pulses. Non-resonant ionization methods are used to determine the cross correlation by measuring the ion signal as a function of pump-probe delay. This method is also used to determine the time zero i.e. the time at which both the pump and probe pulses are temporally overlapped. To obtain a cross correlation and hence time zero NH_3 , CH_3OH and ^{129}Xe are used. The reason for selecting CH_3OH is that both pump (266 nm/200 nm) and probe (250 nm) pulses are non-resonant⁷ with the first excited state. At time zero when both pulses are temporally overlapped, maximum parent CH_3OH^+ ion signal is observed, as shown in figure 2.8 (a). This figure gives the normalized ion signal of parent CH_3OH^+ as a function of pump-probe delay. The ionization of a species non-resonantly also eliminates the effect of populated states that can cause a slight shift in time zero. Figure 2.8 (b) depicts the

$^{129}\text{Xe}^+$ signal as a function of pump-probe delay, showing a clear step that is a manifestation of a very long lived intermediate state. Two photons of 250 nm excite the long lived $5p^5(^2P_{3/2})6p[1/2]_{j=0}$ ^{129}Xe intermediate state that is then ionized by 200 nm. If such a long lived state is excited, the time zero is located half way up the step. On the other hand for NH_3 , shown in figure 2.8 (c), the 200 nm pulse can access the first excited state (A-state) and a fast decay can be seen on both sides of time zero. This suggests that following excitation at 200 nm the decay dynamics are so fast that they can not be resolved within the temporal resolution of the instrument response function. Another interesting feature displayed by figure 2.8 (c) is a fast decay at negative delays, that is when the 250 nm pulse arrives first. Indeed 250 nm is non-resonant with the first excited state in NH_3 , but as it temporally overlaps with the 200 nm pulse, it ionizes NH_3 non-resonantly resulting in maximum ion signal at time zero. The resulting ion signal of NH_3^+ and CH_3OH^+ is plotted as a function of pump-probe delay. A Gaussian function is then fitted to each data set to yield the instrument response function or cross correlation (FWHM) which is approximately 160 fs in these experiments (not shown). The Gaussian function gives an excellent fit to both the NH_3 and CH_3OH ion data which signifies that the instrument response function can be approximated to be Gaussian.

While extracting the time constants shorter than the instrument response function does require well-characterized pulses, as described above the instrument response function is a Gaussian and more important to extract time constants is the temporal overlap between the pump and probe pulses, as it is necessary to measure as accurately as possible, the displacement of the H^+ half maximum relative to time zero (i.e. the rise in the H^+ signal that is measured in these experiments). This is

normally characterized with NH_3 . However, whilst NH_3 provides a reasonable value for time-zero, the fact that one of the pulses (200 nm) is resonant with the first excited state could slightly off-set this value. Since methanol is also used to find time zero where both pulses are non-resonant, adopting both methods of resonant and non-resonant ionization, one obtains a time shift of -15 fs in the peak positions between NH_3 and CH_3OH transients.

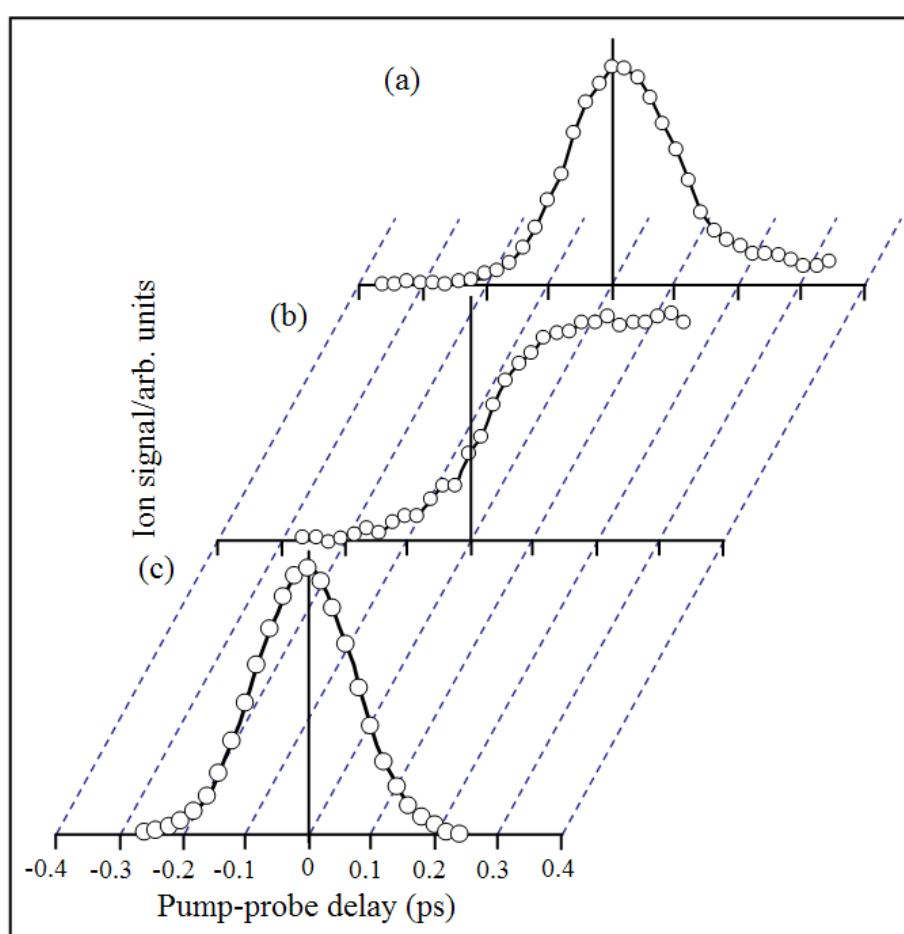


Figure 2.8 (a) CH_3OH , (b) ^{129}Xe and (c) NH_3 ion signal as a function of pump-probe delay. The Gaussian fit to the CH_3OH and NH_3 ion signal suggest that the instrument response function is ~ 160 fs. A step in ^{129}Xe ion signal corresponds to a very long lived state.

However, it is much more practical to use NH₃ to record time zero on a daily basis as it is a gas. As a result, the location of time zero is always offset by -15 fs and incorporated into all the H⁺ transients recorded. Occasionally phenol has also been used to find time zero during time-scan measurements. Interestingly the cross-correlation measured is again 160 fs. The ultrafast decay dynamics on either side of time zero i.e. pump-probe or probe-pump are much faster than the instrument response function and as a result can be used accurately to locate time zero.⁸

2.4.1. Fitting the H⁺ Transient

The central focus of this project is to determine the time evolution of H-atom elimination of biomolecules. Following excitation at 200 nm the optically bright ¹ππ* state is accessed that subsequently couples with an optically dark repulsive ¹πσ* state, through which H-atom elimination can occur. The time constant for H-atom elimination from a particular species is obtained with the help of a mathematical model. The equation (2.9) is used to extract the time constant assuming a single step function in the appearance of the H-atom (i.e. a single pathway) which is the result of a convolution of the instrument response function (Gaussian function) and an exponential rise function.

$$y = y_0 + A^* \left[\left\{ 1 + \operatorname{erf} \left(\frac{x - x_0}{c} \right) \right\} - \left[\frac{\exp \left\{ \frac{c^2 - 4\tau(x - x_0)}{4\tau^2} \right\}^*}{1 - \operatorname{erf} \left\{ \frac{c^2 - 2\tau(x - x_0)}{2c\tau} \right\}} \right] \right] \quad (2.9)$$

Where; $c = \frac{G}{\sqrt{4 \ln 2}}$, (G and all other parameters are defined on next page).

As will become evident in the proceeding chapters, multiphoton effects are prominent in these experiments due to the high intensities of the ultrafast pulses. As a result, in some of the systems studied, a multiphoton component has been observed in H⁺ transients, which is manifested as a sharp rise around time zero owing to the high photon flux. As a result, to extract the time constant from the data containing a step function and multiphoton component equation (2.10) is used which is now the convolution of the instrument response function (Gaussian), an exponential rise function and an additional Gaussian function (encompassing an exponential decay),

$$y = y_0 + A * \left[\left\{ 1 + \operatorname{erf} \left(\frac{x - x_0}{c} \right) \right\} - \left[\frac{\exp \left\{ \frac{c^2 - 4\tau(x - x_0)}{4\tau^2} \right\} *}{1 - \operatorname{erf} \left\{ \frac{c^2 - 2\tau(x - x_0)}{2c\tau} \right\}} \right] \right] + \left[B * \left\{ \exp \left(-\frac{(x - x_0)^2}{c^2} \right) \right\} \right] \quad (2.10)$$

$$\text{Where; } c = \frac{G}{\sqrt{4 \ln 2}}$$

Equations (2.9) and (2.10) are the model equations obtained with the help of Mathematica 7.0. In these equations, y_0 is the base line, A , B are the amplitude factors that determine the various contributions of the step function versus the Gaussian function (multiphoton component), x_0 is time zero, G is the cross-correlation or instrument response (160 fs) and τ is the time constant that needs to be extracted for the appearance of H-atom. The above equations are imported into Origin 7.5 and the above parameters are optimised iteratively when fitting to the data

i.e. H^+ transients. For a normalized H^+ signal, the following parameters are initially used, $y_0 = 0$, $A = B = 1$, $x_0 = \pm 15$ fs and $G = 160$ fs ± 20 fs to extract time constant for H-atoms elimination.

2.4.2. Fitting the Parent Ion Transient

Experiments have also been carried out to probe the real time evolution of first excited state $^1\pi\pi^*$ (S_1) of phenol. In these experiments phenol molecules were excited at various wavelengths using the TOPAS output and probed with the fundamental 800 nm radiation. The results of these experiments will be discussed in chapter 3 but to extract the time constant for the relaxation of this state, the following equation was used.

$$y = y_0 + \left[A * \left[\left[\exp \left\{ \frac{c^2 - 4\tau_1(x - x_0)}{4\tau_1^2} \right\} \right] * \left[1 - \operatorname{erf} \left\{ \frac{c^2 - 2\tau_1(x - x_0)}{2c\tau_1} \right\} \right] \right] \right] + \left[B * \left[\left[\exp \left\{ \frac{c^2 - 4\tau_2(x - x_0)}{4\tau_2^2} \right\} \right] * \left[1 - \operatorname{erf} \left\{ \frac{c^2 - 2\tau_2(x - x_0)}{2c\tau_2} \right\} \right] \right] \right] \quad (2.11)$$

$$\text{Where; } c = \frac{G}{\sqrt{4 \ln 2}}$$

Equation (2.11) was obtained once again in Mathematica 7.0 by convoluting the instrument response function (Gaussian function) with the addition of two decay functions. The additional parameters τ_1 and τ_2 now relate to the time-constants for the two exponential decay components of the fit. For the normalized parent phenol ion

signal, the following values for the above parameters are initially input into Origin; $y_0 = 0$, $A = B = 1$, $x_0 = \pm 15$ fs and $G = 160$ fs and $\tau_l = 10$ fs.

2.5. Velocity Map Ion Imaging

A couple of techniques have been described in chapter 1 to study the photodynamics of molecules, which can give adequate information about the photo-products. But there are many problems in molecular dynamics which require simultaneous measurement of internal and translational energy. Velocity map ion imaging (VMI) is considered a powerful tool to extract this kind of information. The early ion imaging experiments were performed by Chandler and Houston⁹ by dissociating the CH₃I at 266 nm and the resulting CH₃ fragments were ionized at 330 nm via (2 + 1) REMPI. The CH₃⁺ ions generated between the repeller and ground electrodes were accelerated toward a position sensitive detector consisting of a microchannel plate (MCP) and phosphor screen. The images of photo-products were reconstructed by transformation from a 2-dimensional (2D) projection to a 3-dimensional (3D) function and contained the information about the velocity distribution and angular dependence of the photofragmentation relative to the laser polarization.¹⁰

As described in section 2.2, the interaction chamber houses the TOF optics. Spatial distribution of H-atoms eliminated following excitation at 200 nm and probing at 243.1 nm is obtained using the VMI detector. For the time-resolved VMI experiments described herein, the dual stack MCP is replaced by a VMI detector that consists of a dual stack MCP (40 mm diameter Chevron microchannel plates) coupled with a phosphor screen (P-43 Phosphor Screen, Photek). The setup replicates

the setup of Eppink and Parker¹¹, the only difference now being that H^+ ions are detected. The ion optics consist of a repeller, accelerator and ground electrodes; figure 2.9 presents the VMI setup indicating voltages on different ion optics that are used during calibration, the details of which will be discussed shortly.

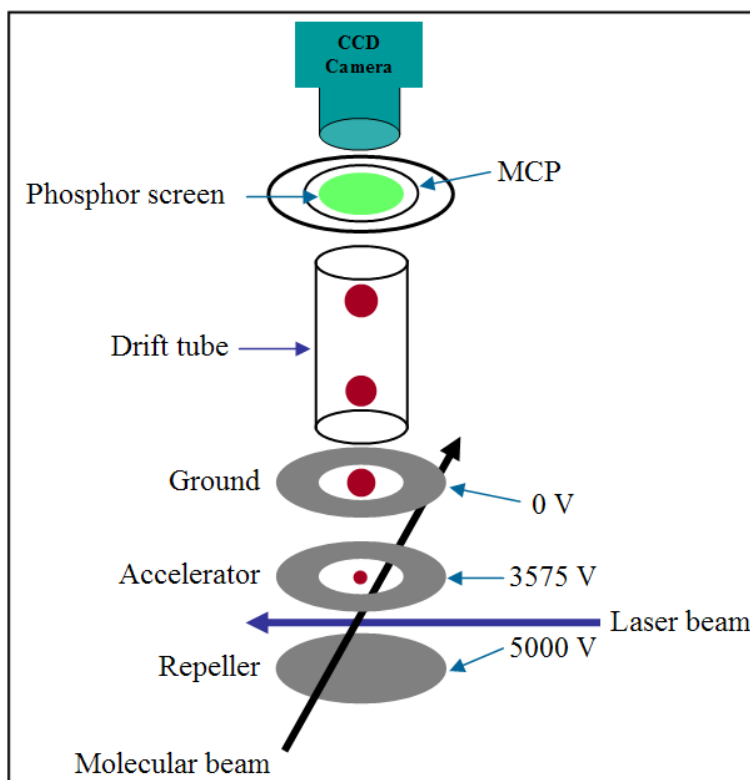


Figure 2.9 VMI setup for H^+ ion detection, indicating H^+ ions (red circles) are generated between repeller and accelerator electrodes, are accelerated through the drift tube and then hit the MCP/phosphor screen (Green). Directly behind is a CCD camera that captures the fluorescence signal from the phosphor screen. The laser polarization is parallel to the plane of the detector.

Eppink and Parker¹¹ improved the ion imaging experiments by replacing the grid to open lens electrodes. Grid electrodes caused a reduction in ions transmission and blurring of the ion images. By overcoming these problems with the help of open lenses they showed that the ions generated with the same initial velocity are mapped

on the same radius on the detector. In other words all the photo-products generated with the same initial velocity vector are focussed on the same point on the detector. They also established an empirical relationship amongst expansion speed, TOF and the radius of the ring appearing on the image and follows as,

$$R = Nvt \quad (2.12)$$

where R , v , t and N are the radius of the ring, expansion speed, TOF and the magnification factor, respectively. The magnification is the factor by which the image size is larger than expected and depends on expansion speed and TOF. The kinetic energy (T) of the recoiling fragments can be related to the radius (from equation (2.12)) of the image by the following equation.

$$T = \frac{1}{2}mv^2 = \frac{1}{2}m\left(\frac{R}{Nt}\right)^2 \quad (2.13)$$

Equation (2.13) shows that the kinetic energy of the recoiling photodissociated products is proportional to the square of the radius of the image. For a flat extraction field ($N = 1$) the speed can be calculated from the image size (R) and TOF. For further calibration of N , a diatomic molecule with well-defined kinetic energies is used. In a later section a detailed description of the calibration of VMI detector will be given, where HBr is used for this purpose.

2.5.1. Anisotropy Measurement of Photo-products

As discussed, VMI can measure the angular dependence of photo-products as a function of laser polarization. When linearly polarized light is absorbed by a molecule e.g. a diatomic molecule, the molecule can dissociate. The dissociated atoms can recoil along the direction of bond but in the gas-phase all molecular orientations are possible. However, it is possible to select the orientation of the molecules to be excited because molecules whose transition dipole moment is aligned along the laser polarization axis preferentially absorb radiation. This picture can be described in a way that during absorption of a photon by a diatomic molecule the electrons in the bond can move along the bond or perpendicular to it; the other orientations are ruled out by symmetry restrictions.¹²

If θ is the angle between the electric vector of the excitation laser and the direction of recoiling fragments, and if dissociation is much faster than molecular rotation, the angular distribution of the photo-products will be proportional to $\cos^2\theta$ for a transition whose transition dipole moment is aligned along the dissociating bond and $\sin^2\theta$ when the transition dipole moment is perpendicular to the dissociating bond. Since both possibilities can arise a mathematical description can give the angular distribution of photo-products,

$$I(\theta) = \left[\frac{1 + \beta P_2(\cos\theta)}{4\pi} \right] \quad (2.14)$$

I is the intensity of absorbed photon at a given θ , β is anisotropy parameter and $P_2(\cos\theta)$ is a second order Legendre polynomial and mathematically can be expressed as,

$$P_2(\cos \theta) = \frac{3 \cos^2 \theta - 1}{2} \quad (2.15)$$

In equation (2.14) β determines the angular distribution of photo-products. For a parallel transition $\beta = 2$ and $I(\theta) \propto \cos^2 \theta$ and for perpendicular transition $\beta = -1$ and $I(\theta) \propto \sin^2 \theta$. Experimentally β ranges between these two limiting values because the rotation of the molecular axis occurs during the separation of photo-products. Some times different states in a molecule are excited simultaneously that have transition dipole moments in different directions, smearing out the β and in extreme cases when transition dipole moments of two states are perpendicular to each other, β becomes zero.

Group theory gives information about the symmetry of the lower and upper electronic states and the direction of the transition dipole with respect to the molecular axis. A projection of the angular momentum of the electrons on the internuclear axis is represented by Ω . For a parallel transition $\Delta\Omega = 0$, hence no angular torque is exhibited on the component of electronic angular momentum that is parallel to the axis because the transition dipole moment is along the internuclear axis. When the transition dipole moment is perpendicular to the internuclear axis the angular momentum of the photon adds to the electronic angular momentum and $\Delta\Omega = \pm 1$. Figure 2.10 illustrates the direction of recoiling fragments with respect to the polarization of laser field.^{12,13}

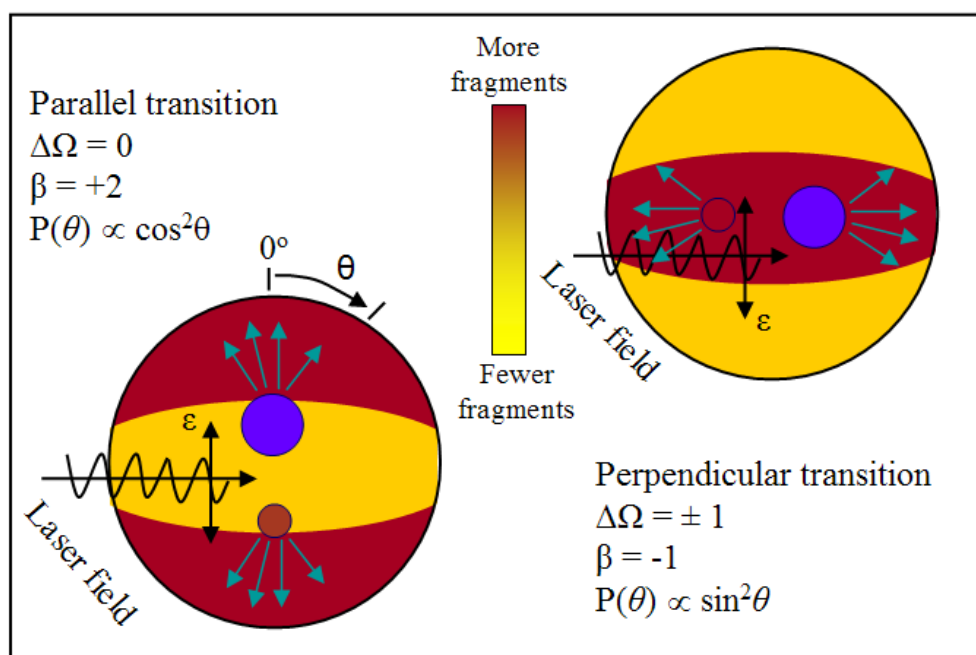


Figure 2.10 Pictorial illustration of angular distribution of photo-products following absorption of linearly polarized light of electric field ϵ , for two extreme parallel and perpendicular transitions assuming very fast dissociation process.¹³

2.5.2. Time-resolved VMI of H^+ Ions

For the purpose of time-resolved VMI of H-atoms both the pump and probe pulses are collinearly combined and are intercepted by the molecular beam of interest. Time zero is obtained by monitoring the parent ion signal of NH_3 . After finding time zero, the probe (243.1 nm) is delayed with respect to the pump (say 200 nm). The pump excites the molecules of interest to a certain PES from which elimination of H-atoms occur which are then probed via (2 + 1) REMPI. The output from the TOPAS i.e. probe beam is normally set at 243.1 nm, but to check whether these H-atoms are neutral or not it is detuned and scanned across 238-248 nm. Normally a sudden rise in signal is observed at 243.1 nm indicative of resonant ionization of H-atoms. The VMI setup encompasses two MCPs (front, and rear) and

a phosphor screen. By applying a timed voltage pulse (Behlke) on the second MCP, this enables us to gate on a particular ion, H^+ in this case, and 2D images of H^+ are recorded. The exposure time to collect the image can be varied $0.1-10^5$ ms but for time-resolved measurements summed images (typically 3-5) are measured at each delay at an exposure time of 10-25 s per image. The fluorescence from the phosphor screen, which varies spatially depending on the location the ion hits the MCP's, is captured by the CCD array of the digital camera (Foculus IEEE 1394). The optical delay between the pump and probe is varied over 3-4 ps in a step size of 0.025 ps. For extended scans this delay stage is varied over 200 ps in a step size of 5 ps. Each accumulated image corresponds to 10000 laser shots and the acquisition and storage process is handled by a programme written in LabVIEW 8.6. The programme gives the images at each delay in BMP (Bit map) format.

Since ultrafast time-resolved pump-probe spectroscopy is employed to generate and detect the H^+ ions, in doing so synchronization is very important amongst various parts of the experimental setup. For instance timing of the laser pulse, Even-Lavie valve, MCPs and deflector plates is critical. The deflector plates are used to deflect the heavier fragment ions in addition to the parent ion which is usually the largest ion signal. This helps to focus (i.e. image) on a particular ion and also to deflect the heavier ions away from the edges of the phosphor screen and hence avoid saturation of the MCPs, The Regenerative Amplifier is used as a base to trigger a digital delay generator (Stanford DG 535) which in turn triggers other components of the experimental setup. The following delays are applied and are shown in figure 2.11 in the form of a flow sheet diagram.

- A trigger with zero delay is used to trigger the oscilloscope.

- A trigger delayed by 1.88 ms is used to pulse the Even-Lavie valve.
- A trigger delayed by 1.98 ms is used to pulse the MCPs.
- A trigger delayed by 1.98 ms is used to pulse the deflector plates.

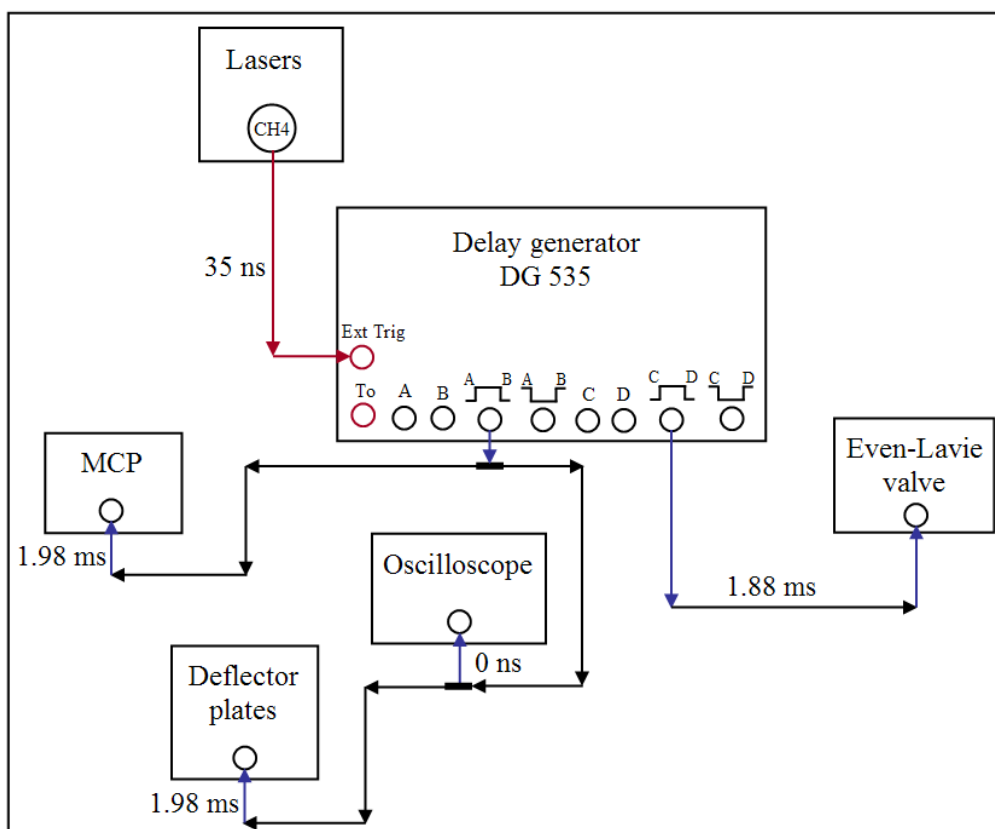


Figure 2.11 A flow sheet diagrammatic representation of triggering scheme used to detect H^+ ions during the experiments. Please note that two additional home-built digital delay generators are used in conjunction with the MCP's and deflector plates to generate the delays of 1.98ms (not shown).

As described above, by applying particular delays on the various parts of the experimental setup, the raw images are obtained and processed with another program (POP) to extract the respective kinetic energies of H-atoms occurring through various pathways. This procedure will be described shortly. However, in order to process the

images and obtain precise kinetic energies of the H-atoms eliminated, calibration of the VMI detector is required (please see section 2.5.3).

By following the procedure described above, time-resolved VMI of H-atom elimination has been measured successfully in phenol¹⁴, indole¹⁵, p-ethylphenol, tyramine and tyrosine. This enabled to pinpoint the various H-atom elimination pathways in these systems and made it possible to establish time constants for each pathway.

2.5.3. Calibration of Velocity Map Ion Imaging

As described in section 2.5, equation (2.13) suggests that the VMI detector can be calibrated with a diatomic molecule that dissociates to yield photo-products with well-defined kinetic energies. HBr is ideal for this purpose. Previous measurements into the photodissociation dynamics of HBr molecules^{16,17} have reported the H-Br bond dissociation energy, D , to be $30\,210 \pm 40 \text{ cm}^{-1}$. From the conservation of energy, following photoexcitation and dissociation, the sum of the dissociation energy, internal energy of the fragments and the total kinetic energy released (TKER) to the fragments must equal the initial photon energy,

$$h\nu = TKER + E(Br)_{\text{int}} + D(H - Br) \quad (2.16)$$

where, $h\nu$ is the energy of absorbed photon, $E(Br)_{\text{int}}$ is the internal energy of bromine and $TKER$ is the total kinetic energy imparted to the H-atoms. In the above equation, the assumption that the H-atom is in its ground electronic state has been made. The resulting photo-products are H and Br. Following photoexcitation at 200 nm, H-Br

can dissociate to give bromine atoms either in their ground state ($^2P_{3/2}$) or spin excited state ($^2P_{1/2}$) separated in energy by 3685 cm^{-1} . By taking into account the reduced mass, the theoretical maximum kinetic energy imparted to the H-atoms are 19546 cm^{-1} and 15906 cm^{-1} for the $^2P_{3/2}$ and $^2P_{1/2}$ channels, respectively. After excitation at 243.1 nm the kinetic energies imparted to H-atoms are 10790 cm^{-1} and 7151 cm^{-1} for $^2P_{3/2}$ and $^2P_{1/2}$ channels and should be observed, albeit with much less intensity given that this is now a four photon process (1 pump photon and 3 probe photons).

The calibration of VMI is done by exciting the HBr molecules at 200 nm and probing the H-atoms at 243.1 nm . The raw image of H^+ along with its kinetic energy is shown in figure 2.12 (a), and has been obtained at a pump-probe delay of 2 ps . This raw image was obtained by applying the following voltages on the ion optics, $V_{\text{repeller}} = 5000\text{ V}$, $V_{\text{accelerator}} = 3575\text{ V}$ ($V_{\text{accelerator}}/V_{\text{repeller}} = 0.715$), these voltages are optimised in such a way that a sharpest and hence best focussed image is obtained on the detector. Figure 2.12(b) gives the H^+ signal as a function of pixel radius and is obtained by deconvolution of the raw H^+ image, presented in figure 2.12(a) using the POP program. The peaks indicated by the arrows represent the kinetic energies imparted to H-atoms whose partner Br fragments are in their ground ($^2P_{3/2}$) and spin/orbit excited ($^2P_{1/2}$) states. There are four peaks corresponding to H^+ obtained with the pump (at 19546 cm^{-1} and 15906 cm^{-1}) and probe (at 10790 cm^{-1} and 7151 cm^{-1}). Figure 2.12(c) presents the H^+ signal versus kinetic energy of H-atoms after converting pixel radius to kinetic energy with the help of equation (2.13). The calibration factor used to convert pixel radius squared to kinetic energy is obtained from the plot shown in figure 2.12(d).

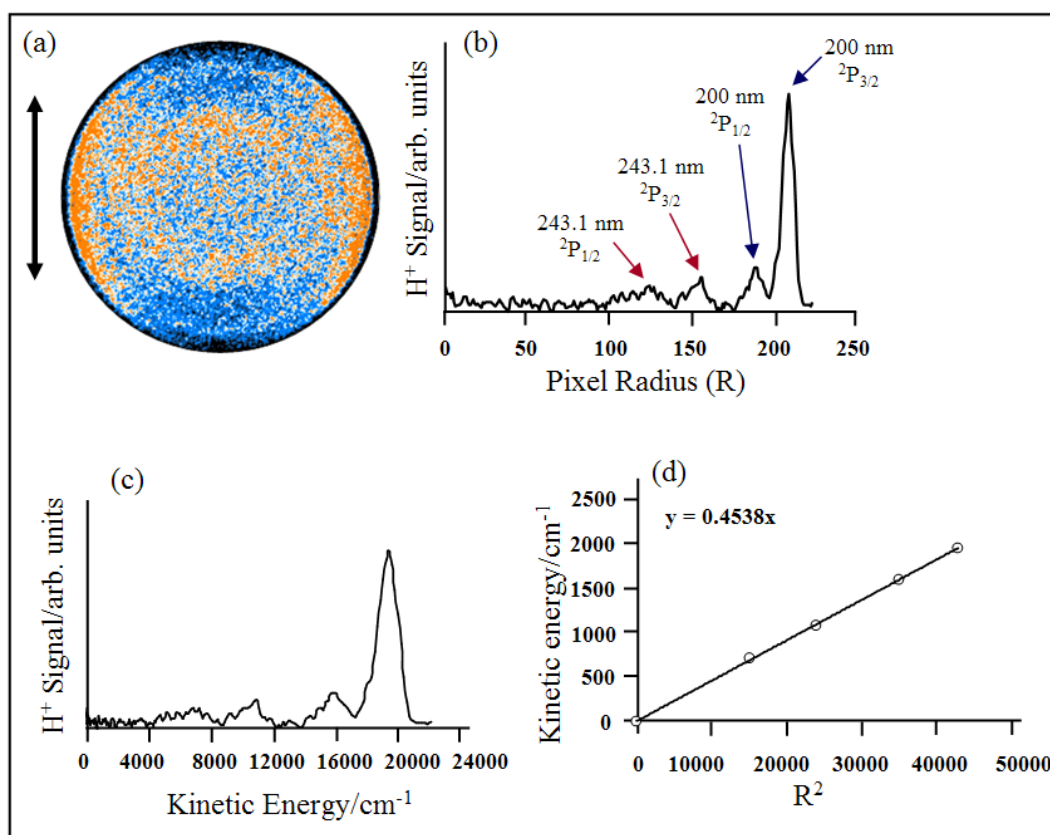


Figure 2.12 Pictorial representation of the calibration of VMI, (a) represents the raw H^+ image that is taken at a pump (200 nm)-probe (243.1 nm) delay of 2 ps, the bold double headed arrow gives the polarization of 200 nm that is parallel to the plane of the paper (b) gives the H^+ signal as a function of pixel radius (c) presents the H^+ signal as a function of kinetic energy and, (d) shows a plot of kinetic energy vs. pixel radius squared suggesting a calibration factor 0.4538 (see text for details).

The anisotropy parameter (β) displayed by the raw image following excitation at 200 nm for the spin/orbit excited and ground states of Br is $\beta = 0$ and $\beta = -1$, respectively, which agree very well with previous measurements.^{16,17} A Gaussian function is used to fit and find the kinetic energy resolution of the instrument using the following,

$$G = e^{-2.77 \left(\frac{(R-R_0)^2}{(0.04 \cdot R)^2} \right)} \quad (2.17)$$

R_0 is the peak maximum and suggest that the resolution defined by $\Delta E/E \sim 4\%$. It is important here to note that the ultimate resolution of the VMI detector is limited by the spectral resolution of the optically broad bandwidth of the ultrafast laser pulses.

2.5.4. Image Processing

When the H-atoms are eliminated after excitation and ionized via $(2 + 1)$ REMPI they are extracted toward the detector which measures the spatial distribution of H-atoms in 2D. The ions generated within the TOF optics are considered as Newton spheres. A method has been developed by Verlet and Roberts¹⁸ to reconstruct the full 3D picture of the photofragment distributions from their 2D projection. The full description of polar onion peeling (POP) technique is beyond the scope of this thesis, but a brief description about the basic principle of this program is given to assist the reader. Essentially, this is done by converting the Cartesian coordinates to cylindrical coordinates, expanding a Newton sphere which is symmetrical around an axis parallel to the projection plane. The basic point is that the intensity of a given point on the 2D detector has a contribution from the Φ dependence of the original 3D distribution as depicted by figure 2.13.

If there is cylindrical symmetry around Φ , i.e. z-axis, its contribution can be removed by calculating R_{\max} from the 2D image and then subtracting for all $R_{\max} < r$ along the decreasing x-direction. By removing the contribution of Φ , a POP algorithm was used, written in LabVIEW. After removing the signal contributed by dissociation events outside the plane of the detector ($R_{\max} < r$), the programme returns the deconvolved intensities as a function of pixel radii which is then converted to kinetic energy using the calibration plot shown in figure 2.12. This

program also calculates the anisotropy parameter of the photodissociated products. As mentioned above (section 2.5.2) the image collected at each delay is exported to the POP program after finding the centre of the 2D image, it deconvolutes the images at each delay and converts this to kinetic energy.

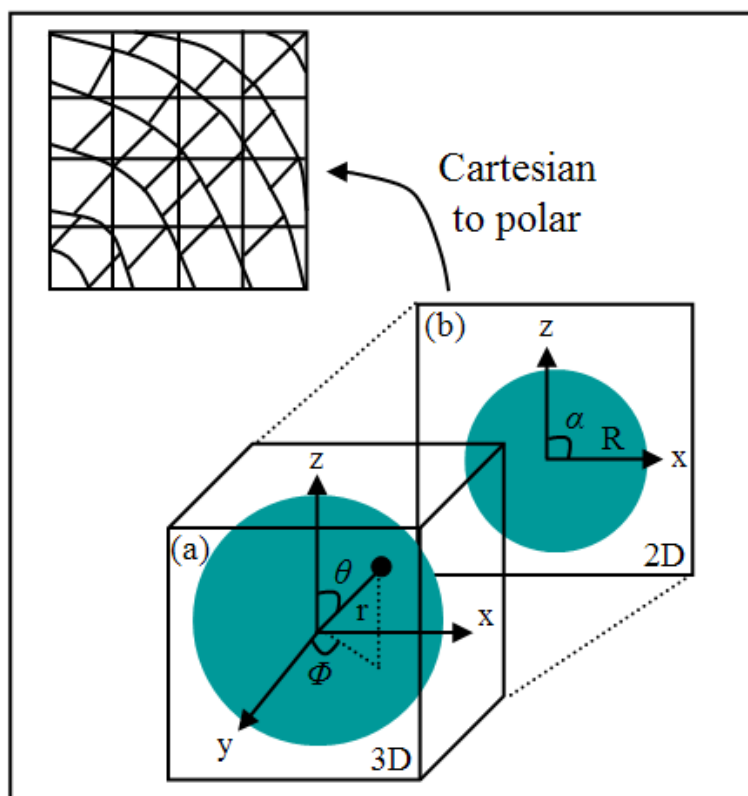


Figure 2.13 Pictorial representation of photo-product of (a) Newton sphere $f(r, \theta, \Phi)$ displaying a cylindrical symmetry about the laser polarization z -axis, (b) 2D distribution $g(R, \alpha)$ produced by mapping onto xz -plane parallel to z -axis. Top figure gives conversion of a Cartesian pixel (square) into a polar pixel (tilted array).¹⁸

This kinetic energy spectrum obtained by the POP program at various pump-probe delays is further integrated at different ranges with the help of another DATAVIEW program that enables one to determine the rise time for the H-atoms as

a function of pump-probe delay. More details of this will be given in the Chapters which follow.

2.6 References

- (1) Jonathan, N.; Morris, A.; Smith, D. J.; Ross, K. J. *Chem. Phys. Lett.* **1970**, 7, 497.
- (2) Demtröder, W. *Laser Spectroscopy; Basic Concepts and Instrumentation*, 2nd *Enlarged ed.* Springer-Verlag Berlin Heidelberg New York, **1998**.
- (3) Even, U.; Jortner, J.; Noy, D.; Lavie, N.; Cossart-Magos, C. *J. Chem. Phys.* **2000**, 112, 8068.
- (4) Tseng, C.-M.; Lee, Y. T.; Ni, C.-K.; Chang, J.-L. *J. Phys. Chem. A* **2007**, 111, 6674.
- (5) Wiley, W. C.; McLaren, I. H. *Rev. Sci. Instrum.* **1955**, 26, 1150.
- (6) Wiley, W. C.; McLaren, I. H. *J. Mass Spectrom.* **1997**, 32, 1.
- (7) Nee, J. B.; Suto, M.; Lee, L. C. *Chem. Phys.* **1985**, 98, 147.
- (8) Lippert, H.; Ritze, H.-H.; Hertel, I. V.; Radloff, W. *ChemPhysChem* **2004**, 5, 1423.
- (9) Chandler, D. W.; Houston, P. L. *J. Chem. Phys.* **1987**, 87, 1445.
- (10) De Rosier, D. J.; Klug, A. *Nature* **1968**, 217, 130.
- (11) Eppink, A. T. J. B.; Parker, D. H. *Rev. Sci. Instrum.* **1997**, 68, 3477.
- (12) Levine, R. D. *Molecular Reaction Dynamics*, Cambridge University Press, **2005**.
- (13) Alexander, A. J.; Zare, R. N. *Acc. Chem. Res.* **2000**, 33, 199.
- (14) Iqbal, A.; Cheung, M. S. Y.; Nix, M. G. D.; Stavros, V. G. *J. Phys. Chem. A* **2009**, 113, 8157.

- (15) Iqbal, A.; Stavros, V. G. *J. Phys. Chem. A* **2010**, *114*, 68.
- (16) Regan, P. M.; Langford, S. R.; Orr-Ewing, A. J.; Ashfold, M. N. R. *J. Chem. Phys.* **1999**, *110*, 281.
- (17) Baumfalk, R.; Buck, U.; Frischkorn, C.; Nahler, N. H. *J. Chem. Phys.* **1999**, *111*, 2595.
- (18) Roberts, G. M.; Nixon, J. L.; Lecointre, J.; Wrede, E.; Verlet, J. R. R. *Rev. Sci. Instrum.* **2009**, *80*, 053104.

Chapter 3

Direct versus Indirect H-Atom Elimination from Photoexcited Phenol Molecules

Using a combination of femtosecond (fs) time-resolved spectroscopy and time-of-flight mass-spectroscopy (TOF-MS), following UV (ultra-violet) excitation of phenol molecules and probing the H-atoms, it has been shown for the first time that the H-atom elimination along the dissociative $^1\pi\sigma^*$ potential energy surface (PES) occurs within $103 \text{ fs} \pm 30 \text{ fs}$, indicating efficient coupling of the PESs at various conical intersections (CIs), with no identifiable role of statistical unimolecular decay of vibronically excited (S_0) phenol in the timeframe of these measurements. In addition, further insight into the precise excitation energy of the S_1/S_2 CI is discussed by probing the excited state dynamics of parent phenol ion (Ph^+) casting considerable doubt over the previously reported location of this intersection.

3.1 Prologue

Aromatic amino acids like tyrosine, tryptophan and phenylalanine have very large UV absorption cross sections. However, the fluorescence quantum yields of these molecules decreases beyond a certain excitation threshold. This is an indication of efficient nonradiative processes, which effectively reduce the fluorescence.¹⁻³ These non-radiative processes must be very fast in order to compete effectively with, and overcome, the fluorescence pathway. In such systems as described above, it seems natural to study the chromophore of the biomolecules itself. Phenol, which is the chromophore of the amino acid tyrosine, shows similar low fluorescence quantum yields.⁴

3.1.1. Potential Energy Profiles along the O-H

Coordinate of Phenol

Recent *ab initio* calculations by Sobolewski and Domcke et al.⁵⁻⁷ have shown that the low fluorescence quantum yield of phenol following excitation above the S_1/S_2 CI is primarily due to an excited singlet state of $^1\pi\sigma^*$ character, which is dissociative with respect to the stretching coordinate of O-H bond. This dissociative state (S_2) bisects both the optically bright $^1\pi\pi^*$ (S_1) and the ground state (S_0) through two successive CIs S_1/S_2 and S_0/S_2 respectively, leading to elimination of H-atom as shown in figure 3.1.

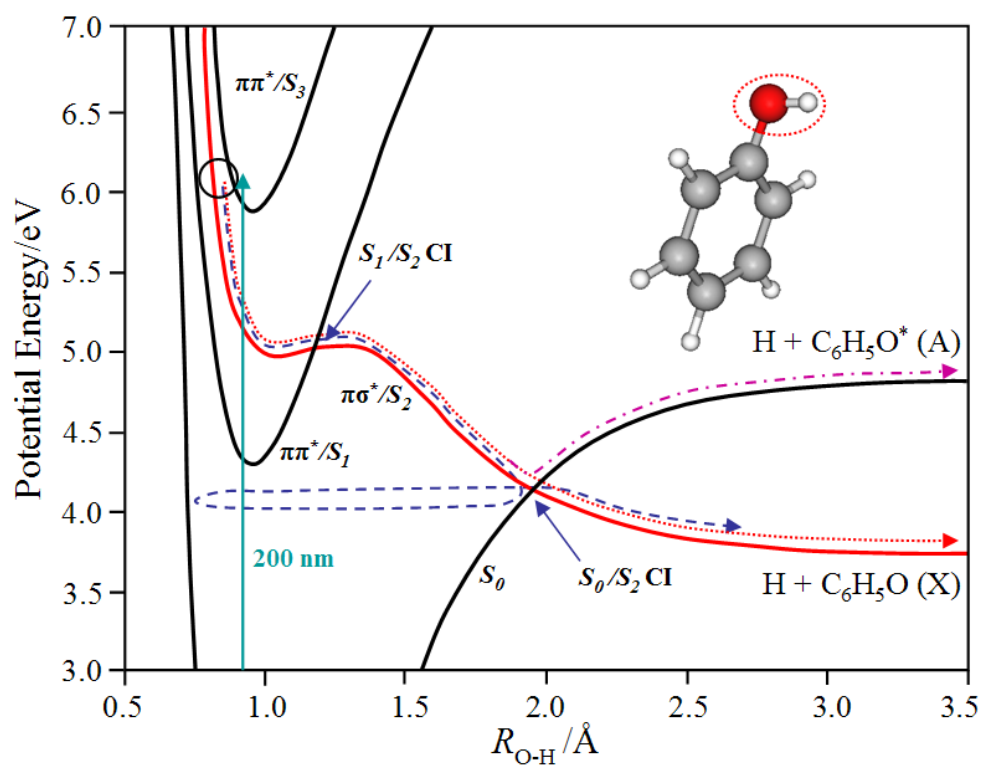


Figure 3.1 Potential energy surfaces along R_{O-H} for the ground (S_0) and the first three excited singlet (two $^1\pi\pi^*$ and one $^1\pi\sigma^*$) states of phenol. These potential energy profiles are adapted from Ashfold *et al.*⁹ and redrawn for illustrative purposes.

The absorption of UV photons below 248 nm corresponds to the photoexcitation of phenol above the S_1/S_2 CI. Generally, the optically dark S_2 state cannot be excited directly. Population from optically bright states such as S_1 or S_3 can be transferred to the S_2 state through the S_1/S_2 or yet uncharacterised S_3/S_2 CI. Once on the S_2 state, the excited phenol evolves towards the S_0/S_2 CI and can undergo two photochemical fates. The first is to continue its passage through the CI and dissociate directly. Alternatively, highly excited ground state phenol may be formed which, following energy dissipation into the correct vibrational mode, i.e. the O-H stretch, can also lead to dissociation. The former and the latter pathways are referred as direct (dotted red curved arrow) dissociation and statistical unimolecular decay^{8,9} (dashed blue

curved arrow), as shown in figure 3.1. The dashed-dotted pink arrow represents the adiabatic pathway of O-H bond dissociation in phenol. The presence of this pathway and the population dynamics of another $^1\pi\pi^*$ (S_3) state following excitation at 200 nm will be discussed in chapter 4.

3.1.2. H-atom Transfer in Phenol-ammonia Clusters

The dynamics of H-atom and proton transfer have been heavily studied in phenol-ammonia clusters.¹⁰⁻¹² Pino et al.,^{13,14} first suggested that excited state hydrogen transfer (ESHT) could be used to explain the decrease in $[\text{PhOH}-(\text{NH}_3)_n]^+$ and the concurrent increase in the $[\text{NH}_4(\text{NH}_3)_{n-1}]^+$ signal. According to Pino et al., and later confirmed by Ishiuchi et al.,¹⁵ using time-resolved ion-dip experiments, the initially excited optically bright $^1\pi\pi^*$ (S_1) state couples to the optically dark $^1\pi\sigma^*$ (S_2) state through a CI. The decay of the phenol cluster can then be explained by tunnelling through a barrier along the O-H coordinate. Unlike in the bare phenol, the reorganization of the electronic levels due to clustering results in the S_2 state not intersecting the ground electronic state (S_0), i.e. there is no S_0/S_2 CI.

3.1.3. H-atom Elimination Measurements in Phenol

The direct observation of H-atom detachment driven through the S_2 state of phenol was first reported by Tseng et al.,¹⁶⁻¹⁸ and then by Ashfold et al.,^{8,9} using multimass ion imaging and total kinetic energy release (TKER) measurements respectively, although to-date, no time-resolved measurements probing the absolute timescales of the direct and statistical unimolecular decay pathways of these two

processes have been reported and provides the driving forces for the work presented in this chapter and thesis. In their work, Nix et al.⁸ report how, at the highest energies in their excitation, which corresponds to approximately the same region of excitation described in this work, they observed two primary peaks in the H-atom kinetic energy release. The peak corresponding to the highest kinetic energy they attributed to direct dissociation. The low energy peak they proposed could be attributed to statistical unimolecular decay of highly excited phenol (S_0) molecules formed due to coupling at the S_0/S_2 CI. A similar observation was also made by Tseng et al.¹⁶⁻¹⁸

3.1.4. Time-resolved H-atom Elimination Studies

To the best of our knowledge, the only direct demonstration of time-resolved H-atom elimination in such systems has been reported in pyrrole via the excited $^1\pi\sigma^*$ state by Lippert et al.¹⁹ using (2 + 1) resonance-enhanced multiphoton ionization (REMPI) by femtosecond laser pulses at 243.1 nm following photoexcitation at 250 nm in a pump-probe setup. Interestingly, Lippert et al., report two timescales for the dissociation, the first they attribute to direct dissociation, with a measured timescale of 0.11 ps. The second pathway due to indirect or statistical unimolecular decay, they measured to occur in 1.1 ps.

If indeed highly excited phenol molecules are undergoing a statistical unimolecular decay process, this should manifest itself in a similar two-step process in phenol. This chapter deals, in part, with the results of a two colour pump-probe experiment with femtosecond laser pulses. The phenol molecules were excited at 200 nm/266 nm and the photoproducts were probed by (2 + 1) REMPI at 243.1 nm with

TOF-MS detection. The results presented strongly implicate a single pathway of H-atom elimination is operative on the timescale of these experiments. The measured dissociation is very fast, suggesting direct dissociation, while no slower component is observed. This implies that if any H-atoms are indeed being formed through a statistical unimolecular decay process, this must be occurring at much longer timescales (>200 ps). This chapter also describes the dynamics of the parent phenol ion (Ph^+) following excitation at 235 nm, 243 nm, 250 nm and 255 nm and probing at 800 nm. These measurements also cast doubt over the energetic location of the S_1/S_2 CI.

To report H-atom elimination measurements in phenol using ultrafast time-resolved TOF-MS, this chapter begins by describing briefly the experimental setup including a description of TOF-MS. This chapter then presents time-resolved TOF-MS of H^+ and discusses the implications of the appearance of H^+ in relation to the dynamics of dissociation. Following this, the dynamics of the S_1 state in phenol will be described by monitoring the Ph^+ ion signal following excitation at various wavelengths.

3.2. The Experiment

The detailed experimental description has been given in chapter 2. Briefly, the optical layout uses a femtosecond laser which is a commercial Spectra-Physics XP system consisting of a Ti-Sapphire oscillator and a regenerative amplifier. The system delivers 3 mJ pulses centred at 800 nm at 1 kHz repetition rate. The measured pulse duration is 35 fs. The output is split into 3 beams of equal intensity, 1 mJ/pulse

is used to generate 200 nm and 266 nm by frequency up-conversion techniques as described in chapter 2. The remaining two beams are used to pump two optical parametric amplifiers (OPA, TOPAS C, Light Conversion). Only one OPA is used for the experiments described herein, which is set at 243.1 nm to probe the H-atoms. The output power is around 6-7 $\mu\text{J}/\text{pulse}$. The other excitation wavelengths used in the photoexcitation are 235 nm, 250 nm and 255 nm and were also obtained using this TOPAS. The fundamental 800 nm was used as a probe to study the life-times of S_1 state. The intensity of 800 nm was adjusted with the help of an iris by altering the diameter of the iris, the beam diameter and therefore power of the 800 nm could be altered. The pump and probe pulses are combined collinearly at a dichroic mirror and sent into the interaction region of a TOF-MS, intercepting a molecular beam of phenol (Fluka, $\geq 99.5\%$). A pump-probe laser cross-correlation (instrument response function) of approximately 160 fs full width half maximum (FWHM) was measured through non-resonant two colour (200 nm/243.1 nm) multiphoton ionization of NH_3 . The relative delay between the pump and probe is varied using a motor controlled delay stage (Physik-Instrumente). The probe is typically varied over 2 ps with a minimum step size of 0.033 ps. For extended H-scans the delay stage was moved over 200 ps in a step size of 5 ps.

A molecular beam of phenol is produced by co-expanding 2-3 psi of He and the vapour pressure of phenol at 70 °C into vacuum using an Even-Lavie pulsed solenoid valve²⁰ operating at 500 Hz synchronously with the laser system. The molecular beam apparatus has been presented, once again, in chapter 2. Briefly, the source chamber housing the pulsed-valve is separated from the interaction chamber by a 2 mm skimmer. The interaction chamber houses the TOF optics which

accelerate the ions, hitting the microchannel plate detector (MCP) located at the terminus of the flight tube (approximately 50 cm). The MCP signal is directed into a multichannel scalar (Stanford, SR430). The ion TOF data accumulated for each 10000 laser pulses is transferred via general purpose interface bus (GPIB) to a computer running an acquisition program written in LabVIEW. Typical peak counts are kept below 0.1 ion counts per 5 ns TOF bin per laser pulse in order to avoid saturation of the scalar.

3.3. Time-of-flight Mass-spectrum

Figures 3.2(a) and 3.2(b) show the TOF-MS of phenol obtained by photoionization using only the pump (200 nm) and both the pump and probe (200 nm and 243.1 nm), respectively. In all the measurements described here, the intensity of the 200 nm was carefully adjusted such that minimum fragmentation of the parent was observed, greatly reducing alternative sources of H-atom production through multi-photon effects. A representative example of this is shown in figure 3.2(a) in which a strong signal is observed at $m/z = 94$ corresponding to the parent phenol in addition to peaks at $m/z = 65$ and $m/z = 66$ corresponding to $C_5H_5^+$ and to a lesser extent $C_5H_6^+$ respectively. Figure 3.2(a) does not show any peak at $m/z = 1$. In contrast, when the pump is followed by the probe, as shown in figure 3.2(b), careful inspection of the TOF-MS reveals a peak at $m/z = 1$, corresponding to the appearance of H^+ . This peak can be seen more clearly in the inset which is magnified 100 fold for illustration purposes. Figure 3.2(b) was obtained by setting the probe delay to be 1.5 ps after the pump. The relatively small size of H^+ signal is indicative of the

inefficiency of the excitation of a narrow atomic line (2s) with a spectrally broad laser pulse, coupled to the non-linearity of the process itself (2 + 1) REMPI.

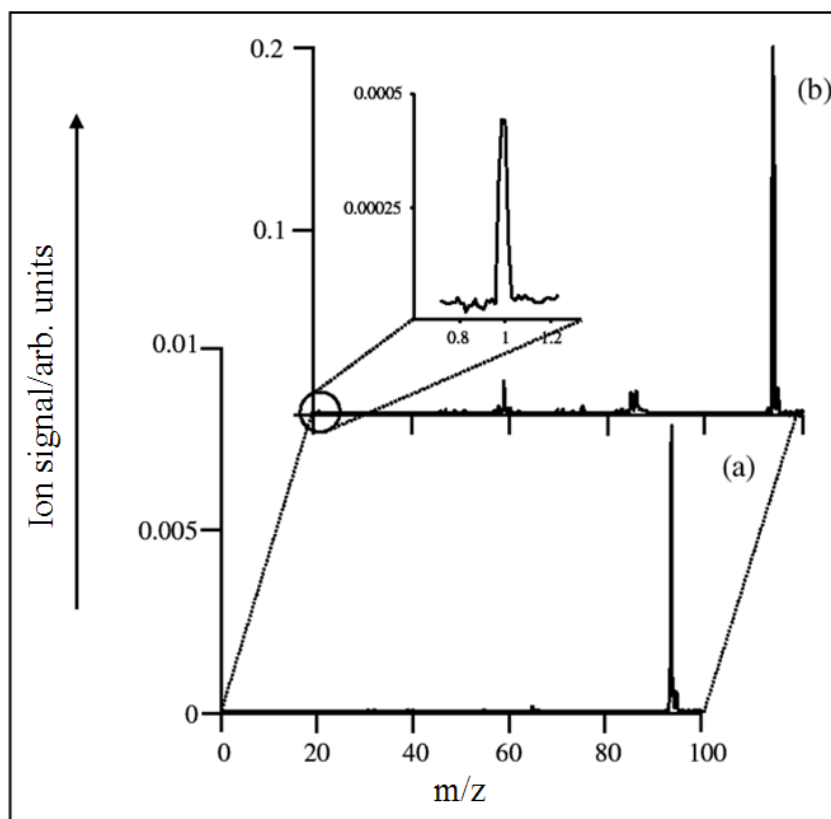


Figure 3.2 One and two-colour mass spectra recorded with femtosecond laser-pulses at 200 nm (a) and 200 nm + 243.1 nm (b) respectively. The delay between 200 nm and 243.1 nm was fixed at 1.5 ps. The intensity of the 200 nm was reduced to avoid other fragmentation pathways.

Ensuring that the 200 nm minimizes the extent of fragmentation through multiphoton ionization is critical to such measurements as other pathways can lead to the generation of H-atoms. For example, appearance energy data²¹ show that at 12.96 eV another exit channel $C_5H_5^+$ ($m/z = 65$) emerges, the other photoproducts being $CO + H$. It is therefore essential that $C_5H_5^+$ is minimized to avoid any contributions

of this pathway to the total H^+ signal and as 12.96 eV corresponds to at least three photons of 200 nm (~ 6.2 eV), small adjustments to the intensity of the 200 nm greatly reduces $C_5H_5^+$ and therefore eliminates this pathway.

3.4. H-atom Elimination via the $^1\pi\sigma^*$ State

Further confirmation that indeed H-atoms are probed following excitation above the S_1/S_2 CI is shown in figure 3.3. This spectrum represents the variation in the integrated H^+ signal as a function of probe wavelength. This measurement was once again taken by setting the delay between the pump and the probe to 1.5 ps. As is immediately apparent, the peak in the H^+ signal is centred at 243 nm. This is to be expected, as 243.1 nm coincides with the resonance at the two-photon level with the 2s state in H (Lyman- α transition). The FWHM of this peak (approximately 1.5 nm), results from the broad spectral profile of the ultrafast pulses originating from the OPA.

Competing pathways such as dissociative ionization which generate H^+ directly can certainly be operative in such large molecular systems and with the high intensities inherent with femtosecond lasers. It is reasonable to assume however that dissociative ionization is unlikely to show such a sharp wavelength dependence on the H^+ signal, as that observed in figure 3.3, coinciding with the $2s \leftarrow 1s$ transition in H-atom. The REMPI signal shown in figure 3.3 together with the minimum fragmentation observed in phenol with 200 nm alone (figure 3.2(a)), suggests that the H^+ ion observed in these measurements originates from H-atoms such as those formed through dissociation via the $^1\pi\sigma^*$ state and not through dissociative ionization to yield H^+ directly.

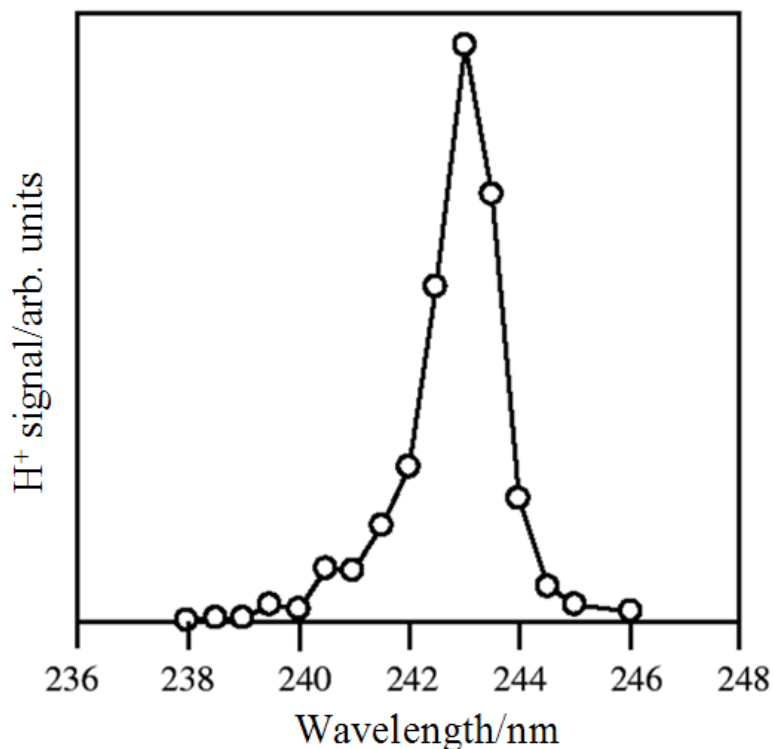


Figure 3.3 Two-colour, multiphoton ionization of H-atoms as a function of wavelength. As the wavelength is tuned on resonance with the $2s \leftarrow 1s$ transition ($\lambda \sim 243$ nm) there is a considerable rise in the integrated H^+ signal as expected.

3.4.1. Direct Pathway of H-atom Elimination

Figure 3.4 shows the transient H^+ signal as the delay between the pump and probe is varied as a function of time. Error bars reported correspond to 95% confidence limits, i.e., two standard deviations of the mean. As can be seen in figure 3.4, when the probe precedes the pump, i.e. at $t < 0$, no H^+ is observed. At times corresponding to $t > 0$, a sharp rise in the H^+ signal can be seen, which is an indication of very fast O-H bond dissociation.

Fitting the time trace to a convolution of an exponential rise function with a Gaussian (instrument response function 160 fs) yields a time constant of $103 \text{ fs} \pm 30$

fs (solid line) in figure 3.4. Time zero and the cross-correlation of the instrument response, was once again measured through non-resonant two-colour multiphoton ionization of NH_3 , methanol and Xe, as described in chapter 2. The uncertainties in the measured FWHM of the Gaussian and the accuracy of time zero have been incorporated in the error.

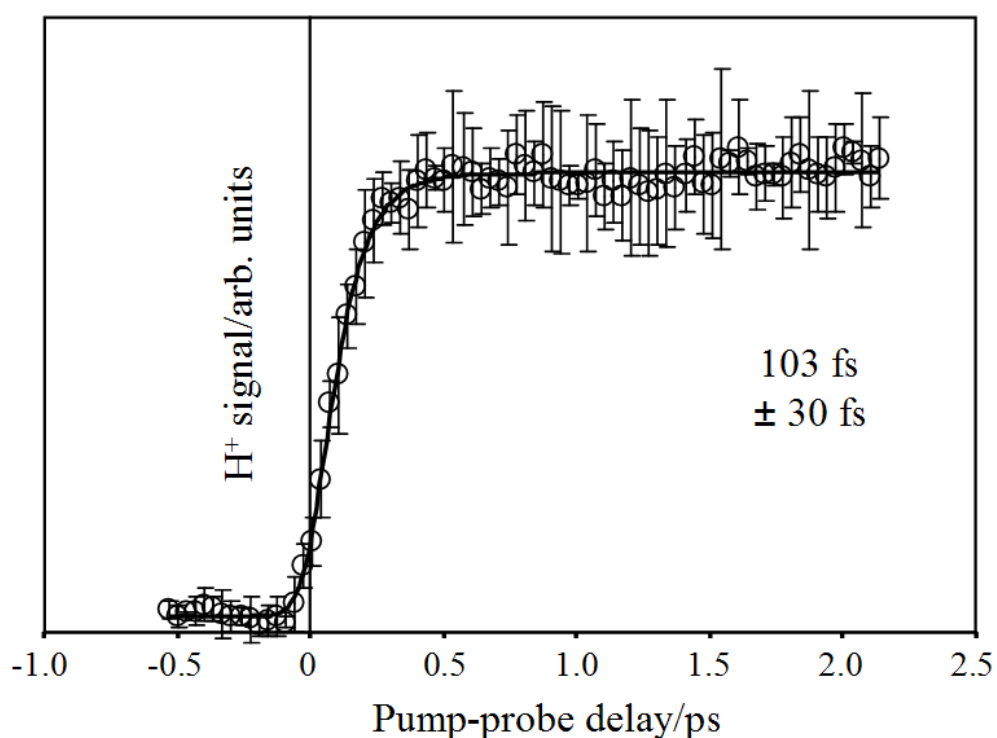


Figure 3.4 H^+ transient as a function of pump-probe delay. At negative time delays ($t < 0$), there is no appreciable H^+ signal. At positive delays, the H^+ signal rises sharply and plateaus beyond 400 fs.

These time scans have been extended to 200 ps, as presented by figure 3.5 and there is no indication of an appreciable increase in the H^+ signal but rather a plateau appears at 400 fs and persists at such long delays.

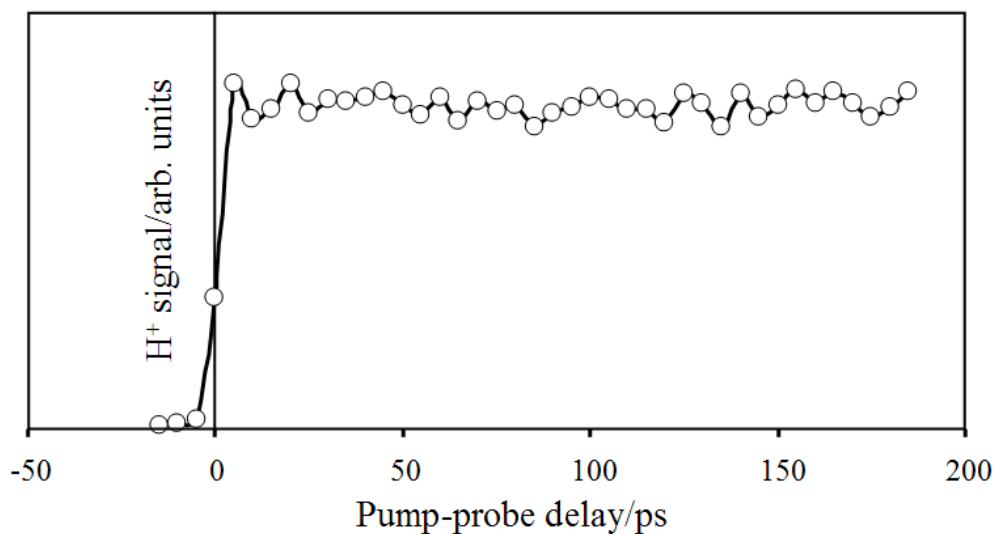


Figure 3.5 H^+ signal versus extended pump-probe delays.

3.4.2. Indirect H-atom Elimination

It is also important to highlight here that attempts have been made to observe H-atom elimination following excitation at 266 nm. These energies excite the phenol molecules below the S_1/S_2 CI, as indicated by figure 3.1, which, as noted by Nix et al.⁸ results in the production of only low kinetic energy H-atoms. The lack of a pump-probe H^+ transient observed (not shown) within the time window of these measurements is consistent with the long lived $^1\pi\pi^*$ state (1-2 ns^{4,22,23}) which undergoes internal conversion to yield highly vibrationally excited phenol (S_0) molecules which can then undergo statistical unimolecular decay.

3.4.2.1. Discussion

The ultrafast H-atom detachment in phenol can be explained using the PESs from figure 3.1, which have been adapted from Ashfold et al.⁹ Following excitation

above the S_1/S_2 CI at 6.2 eV (200 nm), the optically dark S_2 state is populated. This state, which is repulsive with respect to the stretching coordinate of O-H bond, intersects not only the electronically excited S_1 state but also the electronic ground state. These non-adiabatically coupled PESs are responsible for H-atom elimination.⁵⁻⁷ The minimum of the S_1 state is located at ~ 4.5 eV, while the S_1/S_2 CI is at ~ 5 eV. As previously reported^{4,8} excitation at $\lambda \leq 248$ nm (5 eV), H-atom detachment is suggested to occur either directly (dotted red curved arrow in figure 3.1) through two successive CIs, S_1/S_2 and S_0/S_2 or through statistical unimolecular decay (dashed blue curved arrow in figure 3.1) following population of vibrationally excited phenol (S_0) molecules from the S_0/S_2 CI. These two pathways should indeed have two distinct timescales (as reported by Lippert et al.¹⁹), the direct dissociation showing much faster dynamics as compared to the statistical unimolecular decay pathway. The data that is presented in figures 3.4 and 3.5 show very clearly that highly efficient decay dynamics are operative, with a single step observed in the H^+ appearance signal, strongly implicating, within the time-window of the experiment, the direct dissociation pathway dominating, with no apparent statistical unimolecular decay contributing to the signal.

The observation of the ultrafast elimination of H-atoms observed in this work is consistent with the recent time-dependent quantum wavepacket calculations by Lan et al.⁷ In this work, the authors show the effects of initial vibronic excitation in the ground electronic state (S_0) of phenol and the population dynamics between the S_2 , S_1 and S_0 states. These calculations, while they do not exactly mimic the experiments described here, show that the population dynamics are essentially over in 100 fs which, on a qualitative level, agrees with the observations made here.

As described, the recent TKER measurements by Nix et al.⁸ suggests that the statistical unimolecular decay pathway may be operative. The low kinetic energy H-atom fragments observed in these experiments show TKER distributions consistent with statistical unimolecular decay of highly vibrationally excited phenol (S_0) molecules such as might be formed by the coupling at the S_0/S_2 CI. Unlike high kinetic energy H-atoms, which show anisotropy in the H-atom distribution (see chapter 4), consistent with prompt dissociation, the lack of anisotropy in the slower H-atoms, suggest that this pathway is slower than the rotational period of the molecule itself.

In principle, these highly vibrationally excited phenol (S_0) molecules can decay on the period of a single O-H stretching vibration (and longer). If this pathway is indeed operative here, this should manifest itself in a slower component in the appearance of the H^+ signal which has not been observed, even up to delays of 200 ps (figure 3.5). It is interesting to discuss this result with reference to the recent time-resolved measurements by Lippert et al.¹⁹ in pyrrole, following excitation at 250 nm directly to the S_1 ($^1\pi\sigma^*$) state. Lippert et al. observed a slower component in their H^+ signal with a time constant of 1.1 ps, which they attribute to indirect dissociation, following population of vibrationally excited pyrrole (S_0) molecules via the S_0/S_1 ($^1\pi\sigma^*$) CI. It may be that vibrationally excited phenol (S_0) molecules formed via the S_0/S_2 CI do not possess sufficient energy in the O-H vibration to overcome the S_0/S_2 barrier. These excited molecules must then remain on the S_0 PES and, as suggested by Nix et al.,⁸ through anharmonic mixing, sample a much larger range of vibrational phase space before finding a route to dissociate by loss of an H-atom. However, following excitation above the S_1/S_2 CI, both dissociation channels are open in

phenol, leading to either the electronic ground or excited phenoxy fragment: formation of the latter will be discussed in the next chapter 4. Therefore, it is debatable that reflection and subsequent capture of the wavepacket back to the bound state surface of phenol (S_0) will occur, unless the excess energy is absorbed by other degrees of freedom.⁷ Alternatively, vibrationally excited phenol (S_0) molecules are formed through an alternative internal conversion pathway which then undergo statistical unimolecular decay. Either process however must be occurring on a timescale that is longer than the duration of these experimental measurements (>200 ps).

3.5. Dynamics of Parent Phenol Molecules

In an effort to establish the energetic location of the S_1/S_2 CI, a subject that is still open to debate, pump-probe measurements were carried out on the parent molecular ion. In these experiments, the pump excitation wavelength was varied across a broad range of excitation energies whilst the probe was set at 800 nm. Figure 3.6 presents the phenol ion signal (Ph^+) as a function of pump-probe delay. In these experiments the phenol molecules were excited at 235 nm (5.28 eV) figure 3.6(a), 243 nm (5.1 eV) figure 3.6(b), 250 nm (4.96 eV) figure 3.6 (c) and 255 nm (4.86 eV) figure 3.6(d) and probed with 800 nm (1.55 eV). Following excitation at 235 nm, 243 nm, 250 nm and 255 nm the lifetimes (τ) of S_1 state extracted are 80 ps, 240 ps, 410 ps and 920 ps, respectively. The scan lengths of all these experiments were up to 200 ps, due to the limited range of the optical delay line. As the excitation wavelength is increased (i.e. excitation energy decreases), the excited state life time

of this state increases because the excitation occurs below the S_1/S_2 CI. As a result the phenol molecule resists O-H dissociation and is trapped on the $^1\pi\pi^*$ state which is long lived $> 1\text{ns}$.^{4,22,23}

In the potential energy diagram (figure 3.1) the S_1/S_2 CI is situated at $\sim 5\text{ eV}$. All these wavelengths excite the S_1 state of phenol molecules in the vicinity of S_1/S_2 CI. Following excitation at 250 nm and 255 nm the repulsive S_2 state is populated by quantum tunnelling,⁷ which occurs on a very long time scale because the wave packet is trapped in the well of S_1 state. Eventually these excited state molecules relax to the ground state following internal conversion.

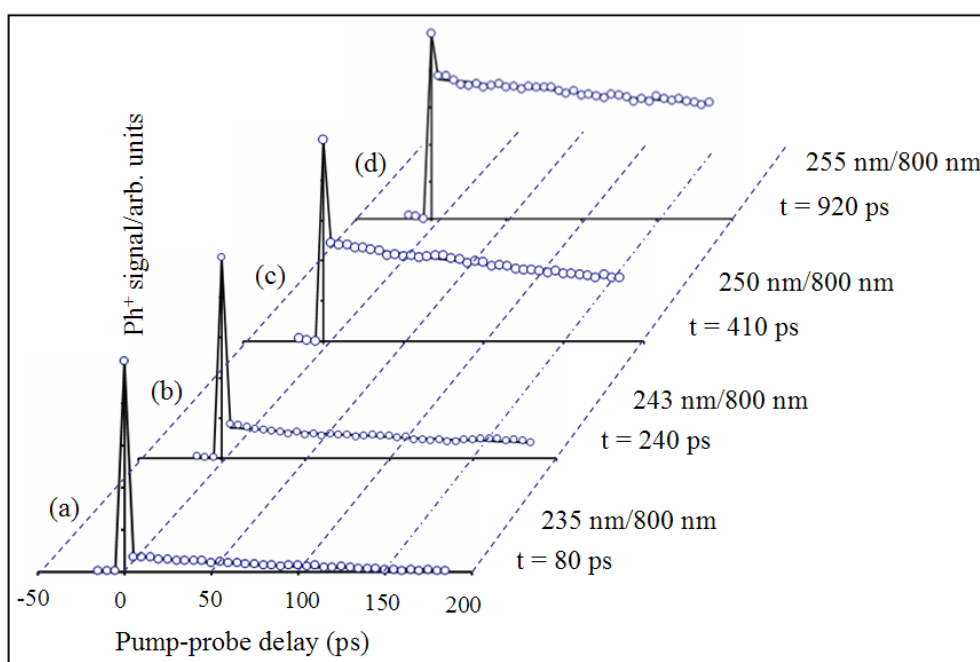


Figure 3.6 Excitation of phenol molecules at different wavelengths and probing with 800 nm. The time constants are extracted with the help of black solid line that is the best fit to the experimental data (blue circles) and is obtained by convolution of a Gaussian of 160 fs FWHM with the sum of two single-exponential decay functions, as explained in chapter 2. On the right hand side of the figure the extracted lifetimes are presented along with excitation and probing wavelengths.

As the wavelength increases, the probability of populating the S_2 state decreases as suggested by the excited state lifetimes. At 243 nm and 235 nm the excitation energies are above the previously reported S_1/S_2 CI. For example, following excitation at 235 nm the excitation energy is ~ 0.28 eV above the S_1/S_2 CI that should result in very fast decay, however the fairly long lifetime measured of $t = 80$ ps casts some doubt about the location of S_1/S_2 CI and it can be speculated that it is likely located above the previously reported value of 5 eV.

It would be ideal to be able to extend these measurements to shorter and shorter pump wavelengths. However owing to the cut-off of the TOPAS output at 235 nm, this is not possible with the current setup. However, it is interesting to see how exciting phenol at 200 nm (6.2 eV) and probing at 243 nm indicates very fast relaxation dynamics which can be attributed to the strong coupling of the S_2 with the S_1 and S_0 states, as shown in figure 3.7.

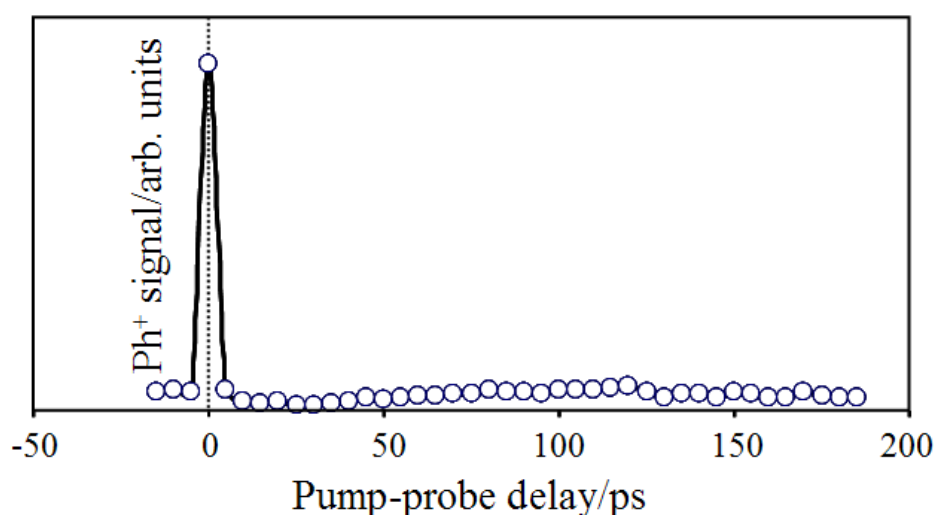


Figure 3.7 Excited state dynamics of phenol exciting at 200 nm and probing with 243 nm.

Another important feature of this transient plot is that following very fast relaxation, there is no evidence to suggest a second slower step (up to 200 ps), clearly indicating that this state has completely decayed. This result is consistent with the findings described above that H-atom elimination following excitation at 200 nm occurs within $103 \text{ fs} \pm 30 \text{ fs}$, without further evidence of a second, slower step.²⁴

3.6. Epilogue

Ultrafast time-resolved pump-probe TOF-MS measurements in phenol, following excitation at 200 nm and probing the H-atoms via (2 + 1) REMP at 243.1 nm show that H-atom elimination along the dissociative $^1\pi\sigma^*$ state occurs within $t = 103 \text{ fs} \pm 30 \text{ fs}$, indicating efficient coupling of the PESs at various CIs, as depicted in figure 3.1 . This is consistent with the high kinetic energy H-atoms observed in recent TKER measurements. Within the time window of the measurements performed here, however, a second pathway to H-atom elimination has not been observed, as observed previously in analogous time-resolved measurements made in pyrrole. This suggests that the low kinetic energy H-atoms observed in TKER measurements carried out in phenol are likely to occur on a much longer timescale ($> 200 \text{ ps}$). Further details about the origin of low kinetic energy H-atoms will be given in chapter 4, where H^+ transient following O-H bond dissociation in phenol-h6 and phenol-d5 will be presented in an energy and time-resolved fashion.

By monitoring the parent phenol ion (Ph^+) signal, the excited state dynamics of the phenol indicates that the lifetime of S_1 ($^1\pi\pi^*$) strongly depends upon the precise excitation energy of this PES. Following excitation at 235 nm, 243 nm, 250 nm and 255 nm and probing of the parent phenol ion at 800 nm, the lifetimes of the

S_1 state obtained are 80 ps, 240 ps, 410 ps and 920 ps, respectively. An observation of a slow decay even at 235 nm suggests that the S_1/S_2 CI is likely located above 5 eV, somewhat higher in energy than expected from earlier spectroscopic measurements.

3.7. References

- (1) Callis, P. R. *Annu. Rev. Phys. Chem.* **1983**, *34*, 329.
- (2) Creed, D. *Photochem. Photobiol.* **1984**, *39*, 563.
- (3) Creed, D. *Photochem. Photobiol.* **1984**, *39*, 537.
- (4) Sur, A.; Johnson, P. M. *J. Chem. Phys.* **1986**, *84*, 1206.
- (5) Sobolewski, A. L.; Domcke, W. *J. Phys. Chem. A* **2001**, *105*, 9275.
- (6) Sobolewski, A. L.; Domcke, W.; Dedonder-Lardeux, C.; Jouvét, C. *Phys. Chem. Chem. Phys.* **2002**, *4*, 1093.
- (7) Lan, Z.; Domcke, W.; Vallet, V.; Sobolewski, A. L.; Mahapatra, S. *J. Chem. Phys.* **2005**, *122*, 224315.
- (8) Nix, M. G. D.; Devine, A. L.; Cronin, B.; Dixon, R. N.; Ashfold, M. N. R. *J. Chem. Phys.* **2006**, *125*, 133318.
- (9) Ashfold, M. N. R.; Devine, A. L.; Dixon, R. N.; King, G. A.; Nix, M. G. D.; Oliver, T. A. A. *PNAS* **2008**, *105*, 12701.
- (10) David, O.; Dedonder-Lardeux, C.; Jouvét, C. *Int. Rev. Phys. Chem.* **2002**, *21*, 499.
- (11) Hineman, M. F.; Kelley, D. F.; Bernstein E. R. *J. Chem. Phys.* **1993**, *99*, 4533.
- (12) Syage, J. A. *J. Phys. Chem.* **1995**, *99*, 5772.

- (13) Pino, G. A.; Dedonder-Lardeux, C.; Grégoire, G.; Jouvét, C.; Martrenchard, S.; Solgadi, D. *J. Chem. Phys.* **1999**, *111*, 10747.
- (14) Pino, G.; Grégoire, G.; Dedonder-Lardeux, C.; Jouvét, C.; Martrenchard, S.; Solgadi, D. *Phys. Chem. Chem. Phys.* **2000**, *2*, 893.
- (15) Ishiuchi, S.; Sakai, M.; Daigoku, K.; Hashimoto, K.; Fujii, M. *J. Chem. Phys.* **2007**, *127*, 234304.
- (16) Tseng, C. M.; Lee, Y. T.; Ni, C. K. *J. Chem. Phys.* **2004**, *121*, 2459.
- (17) Tseng, C. M.; Lee, Y. T.; Ni, C. K.; Chang, J. L. *J. Phys. Chem. A* **2007**, *111*, 6674.
- (18) Tseng, C. M.; Lee, Y. T.; Lin, M. F.; Ni, C. K.; Liu, S. Y.; Lee, Y. P.; Xu, Z. F.; Lin, M. C. *J. Phys. Chem. A* **2007**, *111*, 9463.
- (19) Lippert, H.; Ritze, H.-H.; Hertel, I. V.; Radloff, W. *ChemPhysChem*. **2004**, *5*, 1423.
- (20) Even, U.; Jortner, J.; Noy, D.; Lavie, N.; Cossart-Magos, C. *J. Chem. Phys.* **2000**, *112*, 8068.
- (21) Fraser-Monteiro, M. L.; Fraser-Monteiro, L.; de Wit, J.; Baer, T. *J. Phys. Chem.* **1984**, *88*, 3622.
- (22) Ratzer, C.; Kupper, J.; Spangenberg, D.; Schmitt, M. *Chem. Phys.* **2002**, 283, 153.
- (23) Grégoire, G.; Dedonder-Lardeux, C.; Jouvét, C.; Martrenchard, S.; Solgadi, D. *J. Phys. Chem. A* **2001**, *105*, 5971.
- (24) Iqbal, A.; Pegg, L.-J.; Stavros, V. G. *J. Phys. Chem. A* **2008**, *112*, 9531.

Chapter 4

Exploring the Timescales of H-atom Detachment from Photoexcited Phenol-h6 and Phenol-d5: Statistical vs Nonstatistical Decay

Using a combination of femtosecond (fs) pump-probe spectroscopy and velocity map ion imaging (VMI) techniques, the time and energy resolved H-atom elimination in phenol-h6 and phenol-d5, following excitation at 200 nm above the S_1/S_2 conical intersection (CI) has been measured. H-atoms are eliminated with two distinct ranges of kinetic energy release. Those with high kinetic energy are attributed to direct dissociation, while those with low kinetic energy are traditionally attributed to indirect dissociation or statistical unimolecular decay, both pathways giving electronic ground state phenoxy fragments. At the lowest kinetic energies, the H-atom elimination from phenol-d5 occurs in < 150 fs, in sharp contrast to what one expects from a statistical decay process. This implies that these H-atoms are formed through a direct dissociation process yielding electronically excited phenoxy fragments.

4.1. Prologue

Phenol, the chromophore of the amino acid tyrosine, has been a prime focus in recent years as a prototype molecule for developing a better understanding of electronic structure and photochemistry of other, larger hetero-aromatic biomolecules. The potential energy profiles of phenol along the O-H coordinate proposed by Sobolewski, Domcke and co-workers^{1,2} have been presented in chapter 3, figure 3.1 (section 3.1.1) and we will allude to these throughout this chapter. As described in chapter 3, the potential energy surfaces (PESs) suggested that the low fluorescence quantum yield of phenol following excitation at the wavelength of interest here (200 nm) is due to an excited singlet $^1\pi\sigma^*$ (S_2) state that has a repulsive character with respect to the stretching coordinate of the O-H bond. This dissociative state (S_2) lies below the upper $^1\pi\pi^*$ (S_3) state but intersects both the optically bright $^1\pi\pi^*$ state (S_1) and the ground state (S_0) through two successive CIs S_1/S_2 and S_0/S_2 , respectively.

Due to the weak $S_2 \leftarrow S_0$ transition, S_2 is not excited directly and is populated by radiationless transfer from the optically bright S_1 state or, at these higher energies, from another $^1\pi\pi^*$ (S_3) state that dominates the absorption when $\lambda < 220$ nm.^{3,4} Following population of the S_2 state, the excited phenol molecule evolves towards the S_0/S_2 CI with two possible photochemical fates. The molecule can eliminate an H-atom from the heteroatom site directly via the repulsive $^1\pi\sigma^*$ state or, alternatively, highly excited ground state phenol molecules may be formed which can also release H-atoms when sufficient energy becomes localised in the correct vibrational mode following intramolecular vibrational relaxation (IVR). These H-

atom elimination pathways are commonly referred to as direct dissociation and statistical unimolecular decay respectively,^{3,5} as explained in figure 3.1, chapter 3.

4.1.1. Disentangling Statistical and Nonstatistical

Relaxation Routes

The ability to disentangle the contributions from the direct and statistical pathways to dissociation of these hydrides (X-H) is of considerable value as this can provide detailed information about the nature of the coupling of PESs at the various CIs. This chapter describes the application of ultrafast time-resolved VMI which enables one to clock the real-time H-atom elimination with energy dependence and thus establish a time constant for dissociation via the different pathways. Direct dissociation is known to yield H-atoms with large amounts of kinetic energy, due to the repulsive nature of the $^1\pi\sigma^*$ state, while indirect dissociation typically leads to H-atoms with much less kinetic energy on average. Disentangling these two pathways is possible as VMI enables one to separate H-atoms with varying amounts of kinetic energy within the image. The work presented in this chapter shows that both high and low kinetic energy H-atoms are released on an ultrafast (< 150 femtosecond) timescale, in sharp contrast to what one would expect via an IVR mediated statistical pathway for the low kinetic energy H-atoms. This casts considerable doubt over the previously assigned statistical pathway for dissociation yielding these H-atoms, as determined through multimass ion-imaging and total kinetic energy release measurements.^{3,5-9}

4.1.2. Multimass Ion-imaging of H-atoms

The H-atom elimination through the S_2 state was first reported by Tseng et al.⁶⁻⁸ using multimass ion-imaging. Following excitation at 248 nm and 193 nm, the H-atom detachment from photoexcited phenol-h6 molecules occurred through two channels: One channel gave high kinetic energy H-atoms attributed to direct coupling of the $^1\pi\pi^*$ with the $^1\pi\sigma^*$ state at the S_1/S_2 CI, and the S_0/S_2 CI.⁶ The second channel resulted in low kinetic energy H-atoms, which were assumed to be formed from internal conversion to the ground state, followed by dissociation. As the excitation energy increased, the proportion of low kinetic energy H-atoms increased, apparently due to the increasing rate of internal conversion.⁸ This argument was to some extent supported by the recent calculations of Vieuxmaire et al.⁹ which identified a prefulvenic conical intersection (CI_{pref}) existing at excitation energies of about 2300 cm^{-1} above the S_1/S_2 CI. At these energies, the prefulvenic decay channel opens, providing a direct nonradiative passage from the photoexcited $^1\pi\pi^*$ state through CI_{pref} to the S_0 PES. This channel should compete with the direct H-atom detachment process, thus enhancing the formation of highly vibrationally excited S_0 molecules which undergo IVR mediated H-atom elimination on the ground state S_0 .

4.1.3. Total Kinetic Energy Released by H-atoms

Following excitation above the S_1/S_2 CI, the total kinetic energy release (TKER) measurements by Ashfold et al.^{3,5} reported two primary peaks in the H-atom TKER spectrum. They attributed the peak corresponding to the highest kinetic energy ($\sim 12000 \text{ cm}^{-1}$) to direct dissociation while the low-energy peak was assigned

as being due to statistical unimolecular decay of very highly excited phenol-h6 (S_0) molecules such as those formed due to coupling at the S_0/S_2 or prefulvenic CIs, following single or multiphoton excitation. The observed TKER_{max} of this statistical channel was too high to originate from purely single photon processes. In more recent measurements using velocity map ion imaging (VMI), Hause et al.¹⁰ also attributed the intensity of the H^+ signal in the centre of their ion image, i.e. H-atoms with low kinetic energy, to statistical internal conversion and multiphoton dissociation.

4.1.4. H-atom Elimination in an Energy and Time-resolved Fashion

The ability to measure directly the timescales of both high and low kinetic energy H-atom release provides detailed insight into the dynamics of these two decay channels and therefore represents a step forward in aiding our understanding of statistical vs. non statistical decay dynamics in some of nature's most important photoactive molecules. The only time-resolved H-atom detachment demonstrations in such hetero-aromatic chromophores have been achieved by Lippert et al.¹¹ in pyrrole and also in phenol using a combination of time-resolved spectroscopy and TOF-MS presented in chapter 3. As described in chapter 3, following excitation at 200 nm and probing the H-atoms via (2 + 1) REMPI at 243.1 nm, H-atom elimination from photoexcited phenol molecules occurred within $103 \text{ fs} \pm 30 \text{ fs}$.¹² This was attributed to the very efficient coupling of PESs at various CIs, with no identifiable role of statistical unimolecular decay on the timescale of these

measurements (< 200 ps). However, both the work presented in chapter 3 and the work of Lippert et al.¹¹ measured the total H^+ signal.

The work presented in this chapter is based on a combination of pump/probe spectroscopy and VMI, which enables one to clock the real-time dissociation of H-atom elimination with both time *and* energy resolution. The extra dimension afforded by VMI also allows to measure the appearance times for both the fast (high kinetic energy) and slow (low kinetic energy) H-atoms. The measured appearance time of the slow H-atoms (< 150 fs), casts doubt over their origin as being from a statistical process, implying that they are more likely formed through a direct pathway.

In this chapter, using ultrafast time-resolved VMI, attempts have been made to pinpoint the various H-atom elimination pathways in photoexcited phenol-h6 (C_6H_5-OH) and phenol-d5 (C_6D_5-OH) molecules. The purpose of studying phenol-d5 is to eliminate the contribution, if any, of H from the phenyl ring. Energy *and* time-resolved H^+ transients is presented originating from both phenol-h6 and phenol-d5, discussing their origin in terms of the known and proposed dynamics of dissociation.

4.2. The Experiment

The experiment has been described in detail in chapter 2. Briefly, the optical setup uses 200 nm as pump pulses ($1 \mu J/pulse$) and is generated through frequency up-conversion. The probe pulses at 243.1 nm are generated by an optical parametric amplifiers (TOPAS model 4/800/f, Light Conversion) whose output power is around 6-7 $\mu J/pulse$ and is used to probe H-atoms via (2 + 1) REMPI. After obtaining a collinear combination of both the pump and probe pulses, these are sent into the

interaction region of a VMI spectrometer and the relative delay between the pump and probe is varied over 3 picoseconds (ps) with a minimum step size of 0.025 ps. For extended scans the delay stage is varied over 200 ps in a step size of 5 ps.

A molecular beam of phenol-h6 (Fluka, $\geq 99.5\%$) or phenol-d5 (Sigma-Aldrich, Phenol-2, 3, 4, 5, 6-d5, 98 atom % D) is produced by seeding a vapour pressure of the target molecule in He (2-3 psi and 70 °C), which is admitted into the vacuum using an Even-Lavie pulsed solenoid valve¹³ operating at 500 Hz and synchronized to the laser system. The source chamber houses the pulsed-valve. The interaction chamber contains the VMI detector, replicating the setup as described by Eppink and Parker,¹⁴ to detect H-atoms. The ion optics comprise of a repeller, extractor and ground electrodes. The H⁺ ions are extracted towards the detector consisting of a 40 mm diameter Chevron microchannel plate (MCP) assembly coupled to a P-43 phosphor screen (Photek). By applying a timed voltage pulse (Behlke) on the second MCP, 2D images of H⁺ are collected. The deconvolution of the raw images is done by using an acquisition programme written in LabVIEW which uses the polar onion peeling method.¹⁵

4.3. The Raw Images of H⁺

Figure 4.1(a) and 4.1(b) shows raw images of H⁺ obtained by dissociating phenol-h6 and phenol-d5 respectively, following excitation at 200 nm and probing with 243.1 nm radiation. Only half of each image is shown for illustrative purposes, separated by the horizontal dashed line, each image having been cut centrally along the axis perpendicular to the laser polarization (bold double arrow). The delay

between the pump and probe pulses was set to 2 ps. Both images look qualitatively very similar, with an intense central region and a sharper outer ring.

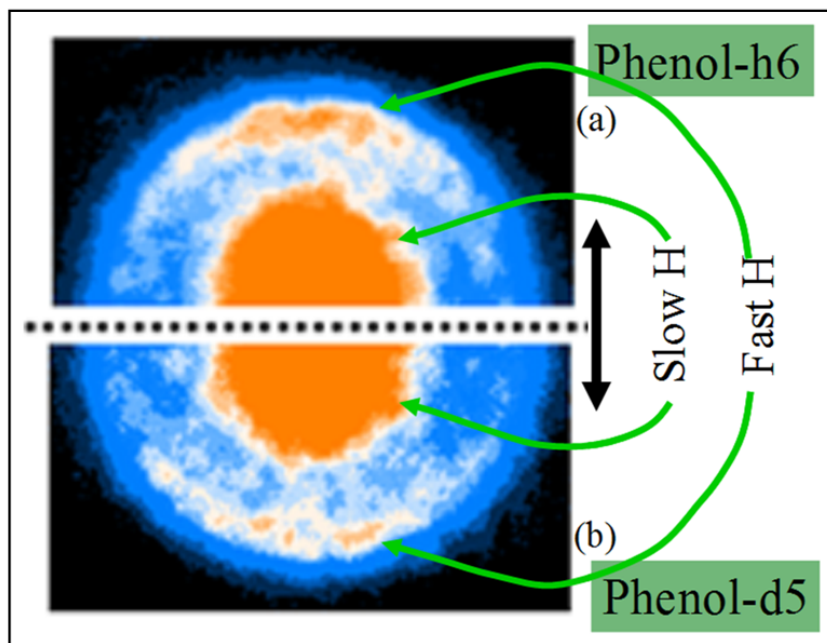


Figure 4.1 Raw images for H^+ following photodissociation at 200 nm and probing with 243.1 nm. Only half of each image is shown for illustrative purposes where (a) and (b) correspond to phenol-h6 and phenol-d5, respectively. In both figures, the 243.1 nm probe was preceded by the pump by a delay of 2 ps.

The outer ring arises from ionisation of kinetically energetic H-atoms formed via direct dissociation through both the S_1/S_2 and S_0/S_2 CIs and most likely another, as yet uncharacterized S_3/S_2 CI, yielding fast H-atoms and ground state phenoxyl cofragments. Following excitation at 200 nm the S_3 state is accessed,^{3,4} the involvement of this state evidenced by the anisotropy parameter (β_2), which suggests that partial parallel dissociation of O-H bond is operative and will be discussed in proceeding paragraphs. The outer ring corresponds to H-atoms with kinetic energies of approximately 11600 cm^{-1} and clearly displays anisotropy, with a measured

anisotropy parameter of $\beta_2 \approx 0.4$, implying a greater contribution of dissociation parallel to the polarization axis of the laser beam. The ions in the centre of the image originate as H-atoms that are born with very low kinetic energy and, based on the current arguments given in the literature, are anticipated largely be a result of some statistical decay process. Immediately apparent however is that the centralized spot occurs even at a 2 ps time delay between the pump and probe pulses.

It is important to stress here that: Firstly, when the probe pulse precedes the pump pulse, there is negligible H^+ signal, indicating that this signal is truly 2-colour; Secondly, detuning the TOPAS output from the $2s \leftarrow 1s$ resonance in the H-atom, considerably reduces the H^+ signal in phenol-d5 indicating that the H^+ detected are indeed H-atoms from dissociation of O-H, which are being probed, rather than nascent H^+ ions originating from multiphoton ion fragmentation channels. Both these observations will be discussed and rationalised in further detail in the proceeding discussion.

4.3.1. Kinetic Energy Spectrum of H-atoms

Figures 4.2(a) and 4.2(b) show the H^+ transient as a function of kinetic energy of H-atoms at two pump-probe delays for phenol-h6 and phenol-d5, respectively. When the pump is preceded by the probe, there is no H^+ signal present and this data is therefore not shown. At $t = 0$, where t refers to the delay in time between the pump and probe pulses, i.e. when the pump and probe are temporally overlapped, H^+ signal appears (dashed line). The signal grows with increasing t , but the kinetic energy spectrum remains unchanged from 500 fs onwards and a representative example is

shown by the solid line, corresponding to a 2 ps pump-probe delay. As is evident from both figures, there are two distinct peaks in the spectra, with maxima occurring at approximately 11600 cm^{-1} for fast H-atoms and at 2700 cm^{-1} for slow H-atoms. The shape of these kinetic energy distributions is in very good agreement with those obtained for nanosecond single photon dissociation by Ashfold et al.⁵ and more recently by Hause et al.¹⁰

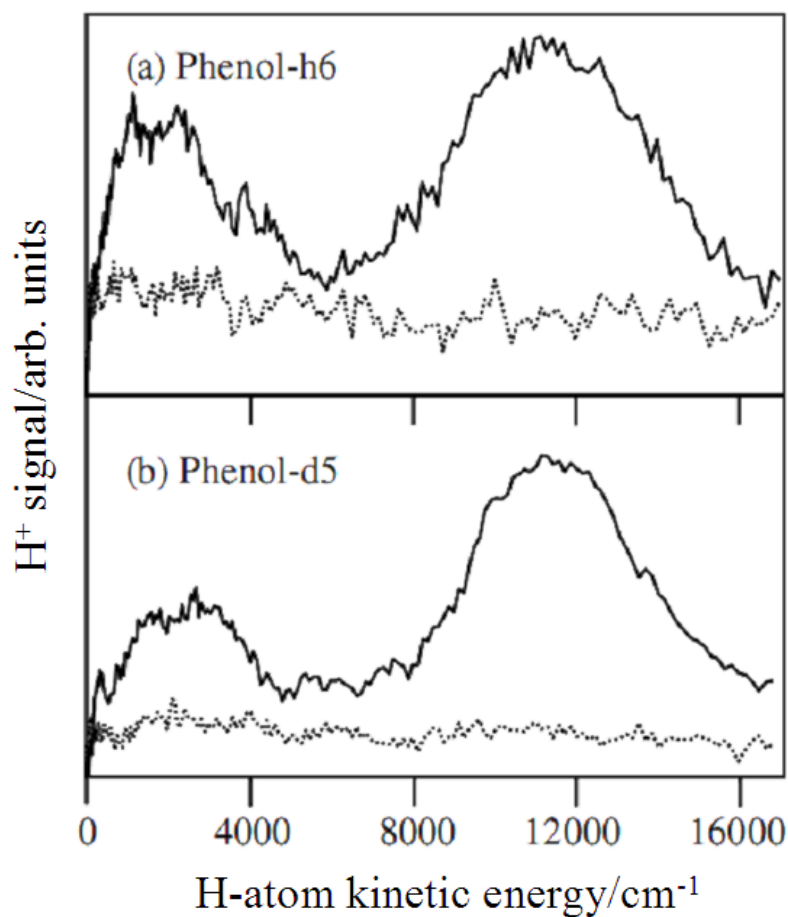


Figure 4.2 H^+ transient as a function of H-atom kinetic energy (dashed and solid lines correspond to pump-probe delays (t) of 0 and 2 ps respectively) for (a) Phenol-h6 and (b) Phenol-d5 molecules. At $t < 0$ there is no appreciable H^+ signal and therefore these transients are excluded for clarity.

Deuterating the C-H bonds in phenol and probing for H-atoms removes any contribution to the signal from the H-atoms of the phenyl ring. As is evident in figures 4.2(a) and 4.2(b), the peak intensity of the low kinetic energy H-atoms in phenol-d5 is somewhat less than that of the high kinetic energy H-atoms (figure 4.2(b)) whereas the peak intensity of the low kinetic energy H-atoms in phenol-h6 is comparable to that of the high kinetic energy H-atoms (figure 4.2(a)).

This illustrates some contribution of phenyl ring C-H fission to the signal in phenol-h6, as observed by Hause et al.¹⁰ Multiphoton effects are likely candidates for generating H^+ directly from any H-atom site. This is quite clearly illustrated in figures 4.3(a) and 4.3(b). Once again, these figures show the transient H^+ as a function of kinetic energy at a pump-probe delay of 2 ps. The solid and dashed lines correspond to the probe pulse centred at 243.1 nm and 238 nm respectively. When the probe wavelength is detuned from the H-atom $2s \leftarrow 1s$ resonance using 238 nm radiation, the H^+ signal is reduced considerably in phenol-d5 across a broad range of kinetic energies compared with a 243.1 nm probe. In phenol-h6, this is not the case with the persistence of a substantial signal for low kinetic energy H^+ , even when the probe pulse is non-resonant. The wavelength independence and broad kinetic energy distribution of this off resonance signal indicates that the origin of the H^+ observed (at 238 nm) in phenol-h6 at low kinetic energy is very likely due to a combination of multiphoton effects such as from 238 nm alone (not observed in phenol-d5) and 200 nm/238 nm, both resulting in dissociative ionization of the parent C-H bonds yielding H^+ directly or alternatively from the parent ion further absorbing 200 nm/238 nm light non-resonantly to yield H^+ . Although the low kinetic energy H^+ observed in phenol-h6 at 243.1 nm is very likely to include a significant component

of H-atoms from O-H dissociation, to eliminate the ambiguity in the dynamics that arises from H⁺ from the phenyl ring, the remaining discussion focuses on O-H fission in phenol-d5.

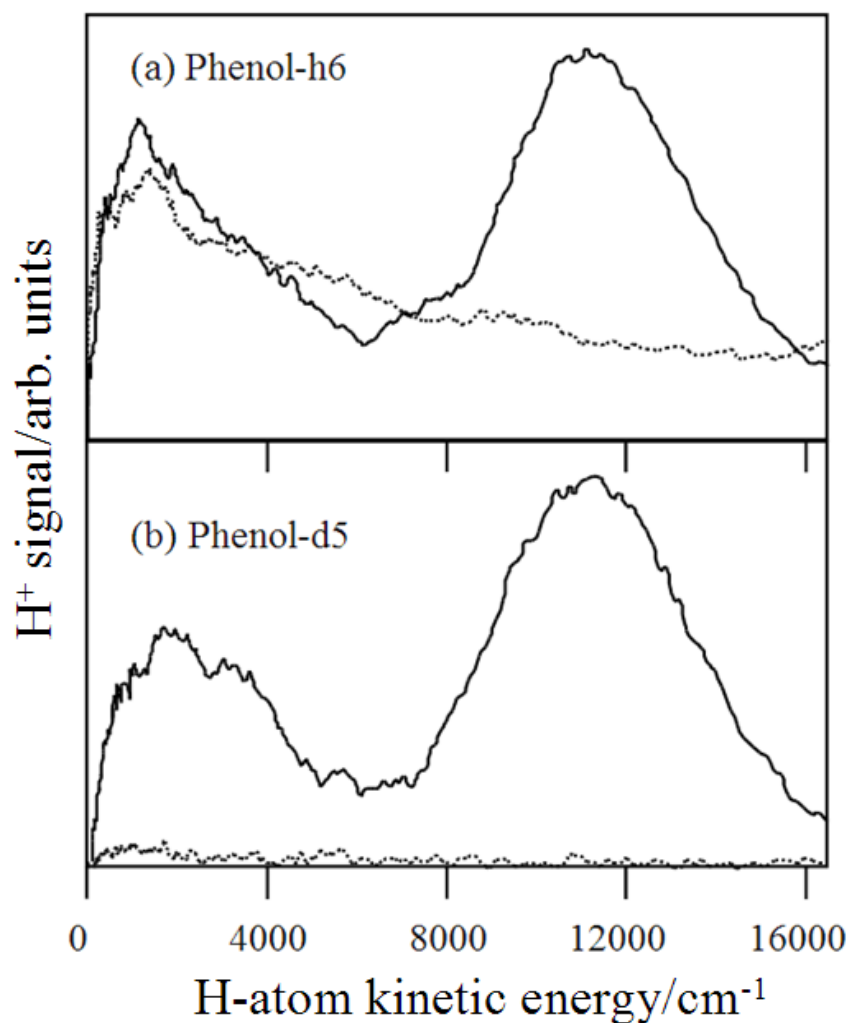


Figure 4.3 H⁺ transient as a function of H-atom kinetic energy. Dashed and solid lines correspond to a pump (200 nm) followed by a delayed probe (2 ps) centred at 238 nm and 243.1 nm respectively, (a) phenol-h6 and (b) phenol-d5 molecules. Note that the spectra recorded at 238 nm and 243.1 nm have not been normalized.

4.3.2. Timescales of O-H Bond Photolysis in Phenol-d5

Figures 4.4(a) and 4.4(b) show the transient H^+ signal following photodissociation of phenol-d5 at 200 nm and ionisation at 243.1 nm. The error bars correspond to a confidence limit of 95 % i.e., two standard deviations of the mean. The transient H^+ signals were obtained by collecting a series of kinetic energy spectra at various pump-probe delays and integrating the H^+ signal across discrete portions of the kinetic energy spectrum. Figure 4.4(b) corresponds to the integrated intensity obtained at the maximum of the high kinetic energy peak at 11600 cm^{-1} and figure 4.4(a) corresponds to the integrated intensity at the low kinetic energy peak at 2700 cm^{-1} (the integral widths are approximately 1000 cm^{-1}).

It is also important to highlight here that data presented in figures 4.4(a) and 4.4(b) is normalized. In both figure 4.4(a) and 4.4(b), when the probe precedes the pump, that is, $t < 0$, no H^+ is observed. At $t > 0$, a sharp rise in the H^+ signal can be seen that plateaus at 500 fs and persists up to 2500 fs, indicative of very fast O-H bond dissociation. Fitting the time trace to a convolution of an exponential rise function with a Gaussian function (FWHM of 160 fs), yielding time constants of $88\text{ fs} \pm 30\text{ fs}$ and $146\text{ fs} \pm 25\text{ fs}$ (solid black line) for the fast and slow H-atoms, respectively. Further details regarding fitting procedure is given in chapter 2.

There is a general consensus in the literature that the H-atoms with low kinetic energy must be due to some statistical decay process following population of highly excited ground-state phenol molecules.^{3,5,10} However, as is clearly evident from figure 4.4(a), following photolysis at 200 nm, low kinetic energy H-atoms are formed on an ultrafast timescale. If these H-atoms were formed from a statistical

process, it would be anticipated that their appearance would be over a much longer timescale than that measured here.

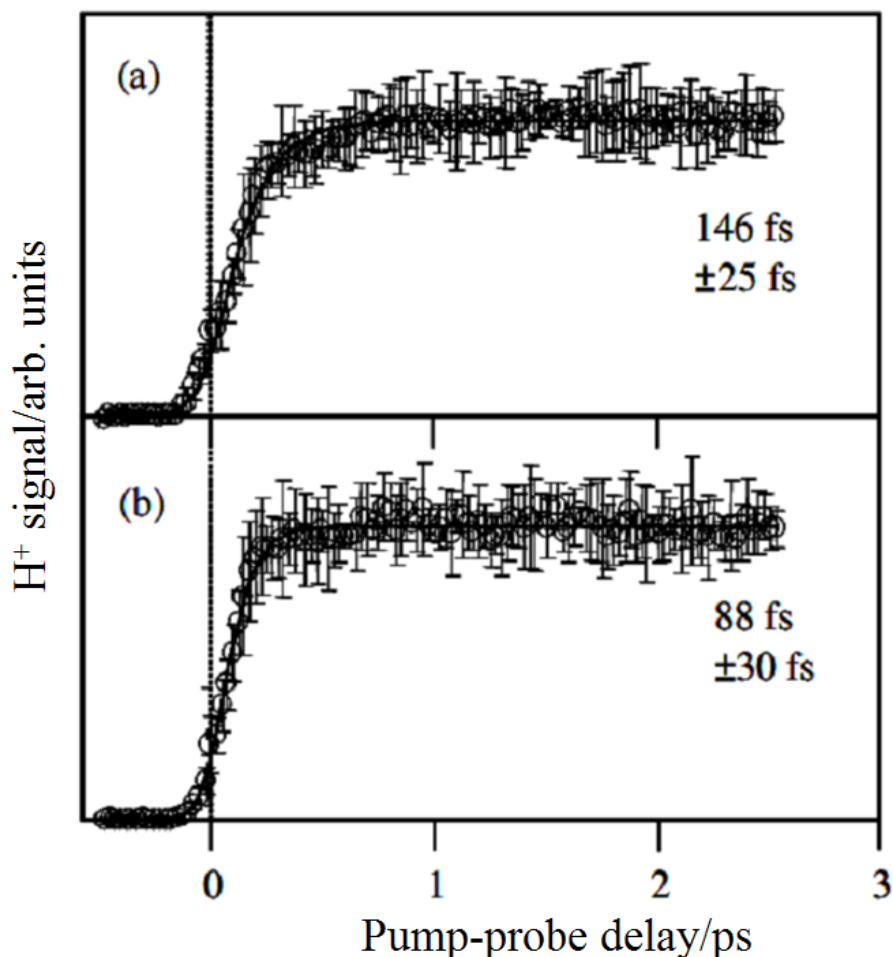


Figure 4.4 H^+ transients as a function of pump (200 nm)-probe (243.1 nm) delay for the low kinetic energy (a) and high kinetic energy (b) H-atoms in phenol-d5. At negative time delays ($t < 0$), there is no appreciable H^+ signal. At positive delays, the H^+ signal rises sharply and plateaus beyond 500 fs.

These scans have been extended to 200 ps and there is in no significant difference in H^+ yield, as shown in figure 4.5. The extended time of H^+ transients have been obtained for both high (black trace with circles) and low kinetic energy H-

atoms (red trace with squares) which show that even at delays approaching 200 ps, there is no identifiable increase in either transient signal, strongly indicating that there must be another, ultrafast, pathway that is giving H-atoms with the low recoil energies observed. It must be noted here that although a statistical pathway may still be operative, this process is likely to occur well-beyond the timeframe of these measurements.

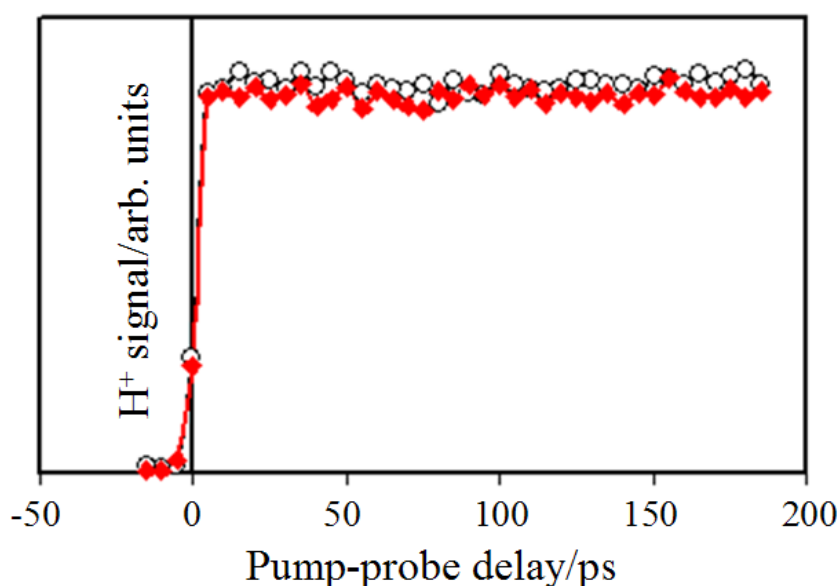


Figure 4.5 H^+ transient as a function of pump (200 nm)-probe (243.1 nm) at extended delays for phenol-d5. The black trace with circles indicates the integral at high kinetic energy maximum (11600 cm^{-1}) and the red trace with squares represents the integral at low kinetic energy maximum (2700 cm^{-1}).

Indeed, RRKM calculations have been carried out using the standard rate equation and the Direct Beyer-Swinehart algorithm for vibrational density of states.¹⁶ Calculations were performed by using B3LYP *ab-initio* frequencies for phenol-d5 OH at equilibrium and assumed that the 3 disappearing modes have half their

original frequency at the transition state (S_0/S_2 CI). Using 33000 cm^{-1} as the critical energy (location of the S_0/S_2 CI) and 50000 cm^{-1} as the available energy, the RRKM calculation yielded a lifetime of the order of 65 microseconds (μs). Any H-atoms formed through a statistical process will therefore represent a very small fraction of the overall yield by $t = 2\text{ ps}$. The measured kinetic energy distributions are extremely similar to those of Ashfold et al.^{3,5} and Hause et al.¹⁰, obtained using nanosecond lasers, which would also be insensitive to such a slowly growing signal.

4.3.3. Anisotropy displayed by H-atoms

Figure 4.6 shows the variation of the angular anisotropy parameter, β_2 as a function of kinetic energy deposited in the H-atom fragment. The origin of the β_2 value for the high kinetic energy H-atoms will be discussed first. The positive non-limiting β_2 value for the high kinetic energy H-atoms in the region of 12000 cm^{-1} is in clear contrast to the negative, non-limiting β_2 for the high kinetic energy H-atoms observed by Nix et al., when pumping phenol-h6 in the range $246 > \lambda_{\text{phot}} > 220\text{ nm}$.¹⁷ At the excitation wavelengths described in the measurements by these authors, initial excitation accessed the S_1 state, where the transition dipole for the $S_1 \leftarrow S_0$ transition lies in a plane orthogonal to the C-O bond. Subsequent prompt dissociation leading to these fast H-atoms preserved the initial recoil anisotropy leading to a negative, non-limiting $\beta_2 \approx -0.5$. The measurements described here, however most likely access the S_3 state, which is observed in the UV-Vis spectrum at $\sim 210\text{ nm}$.^{3,4} From TDDFT and CASSCF¹⁸ calculations, the S_3 state is predicted to be the second $^1\pi\pi^*$ where the $S_3 \leftarrow S_0$ excitation now has a transition dipole that is orthogonal to that of $S_1 \leftarrow S_0$

and is roughly aligned along the C-O bond axis. It is therefore unsurprising that following excitation to the S_3 state, prompt dissociation leading to H-atoms with large amounts of kinetic energy preserves the initial recoil anisotropy, leading to a *positive*, non-limiting $\beta_2 \approx 0.4$, opposite to that observed when pumping via the S_1 state. Owing to the decrease in signal-to-noise at the very highest kinetic energies, it is not possible to extend these anisotropy measurements beyond 16000 cm^{-1} .

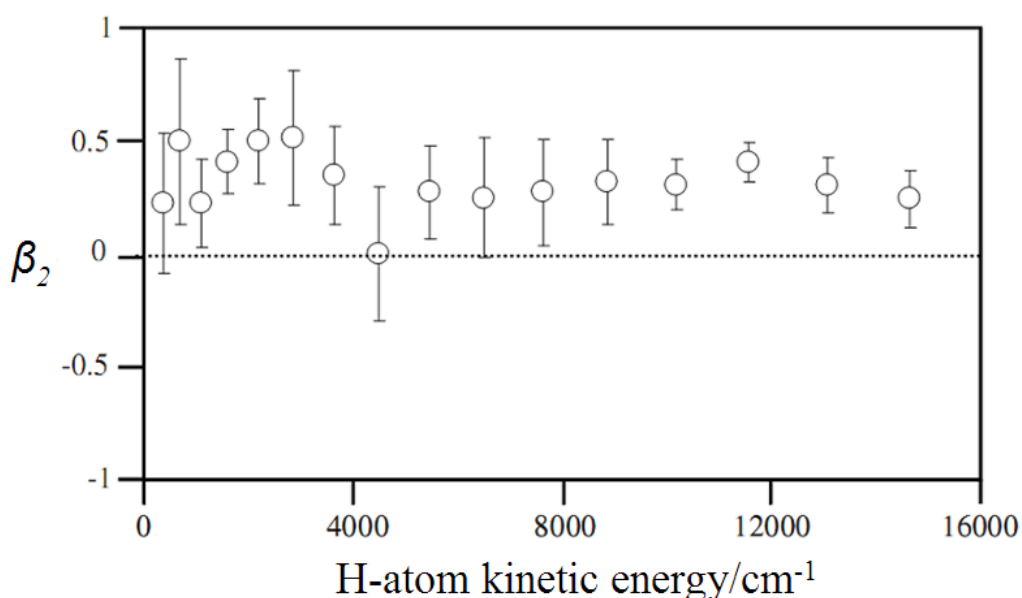


Figure 4.6 Anisotropy parameter (β_2) as a function of kinetic energy of H-atom fragment. The pump (200 nm)-(probe (243.1 nm) delay was set at 2 ps for these measurements. At the highest kinetic energies, $\beta_2 \approx 0.4$ while at lower kinetic energies, a positive, non-limiting β_2 still persists but with decreased signal-to-noise (see text for details).

For the low kinetic energy H-atoms, the anisotropy parameter still displays positive values, albeit with larger errors due to decrease in signal-to-noise. The anisotropic distribution of these low kinetic energy H-atoms is again in contrast with that observed by Nix et al. at lower photon energies in phenol-h₆,¹⁷ who, in the

absence of time resolved data, assigned these fragments to single and multiphoton statistical unimolecular decay processes. The timescales involved with statistical unimolecular decay are such that any initial recoil anisotropy would be lost as the molecule would most certainly have undergone multiple rotations prior to dissociation. However, the measurements performed here, the time constant for the low kinetic H-atoms from phenol-d5 is $146 \text{ fs} \pm 25 \text{ fs}$. Dissociation on this timescale would cause any initial recoil anisotropy to be preserved, clearly shown by figure 4.6 at low kinetic energies.

4.3.3.1. Discussion

Recent calculations by Vieuxmaire et al.⁹ have suggested that a prefulvenic decay mechanism, similar to that observed in other single ring aromatic systems, such as benzene, may effectively compete with other decay mechanisms from the S_1 state, such as direct hydrogen detachment via the $^1\pi\sigma^*$ state. This interpretation has been suggested to explain the low kinetic energy H-atoms in some of the multimass ion-imaging results obtained by Tseng et al.⁸ between 248 nm and 193 nm. The CI_{pref} can provide a nonradiative decay channel resulting in the formation of highly vibrationally excited S_0 molecules which undergo statistical unimolecular decay. For this pathway to be effective at explaining the results, both nonradiative population of the S_0 state and subsequent statistical unimolecular decay must be completed by 500 fs, as seen in figure 4.4. Although this pathway may be operative at much longer timescales than in the timeframe of these measurements, it is unlikely to explain the prompt, low kinetic energy H-atoms observed here unless the majority of the excess

electronic energy is deposited immediately into the O-H stretching vibrational mode for dissociation to complete after a few vibrational periods. The calculated structure and branching space of this intersection do not indicate any role for the O-H bond extension in coupling the S_1 and S_0 states non-adiabatically and it therefore seems unlikely that such uniquely selective internal conversion could occur at this CI.

The appearance times of these slow H-atoms (< 150 fs) rules out their indirect formation through statistical unimolecular decay and an alternative explanation must be sought. Ultrashort lasers pulses are synonymous with multiphoton effects. Indeed, superexcited states populated following multiphoton excitation via $^1\pi\pi^*$ states have been shown to lead to ultrafast dynamics, via predissociation to yield H-atoms.¹⁹ Schick and Weber have demonstrated that photoelectrons generated by autoionisation of these superexcited states, following multiphoton excitation around the ionization potential of phenol (8.5 eV),²⁰ occur with appearance times shorter than their instrumental response function (< 230 fs),¹⁹ suggesting that the decay lifetimes of these excited states into the ionisation continuum is equally prompt. Two-photon excitation with 200 nm light used here would result in excitation well-above the ionization potential of phenol, increasing the autoionisation rate and limiting the role of superexcited states in producing H-atoms via a predissociation mechanism occurring with a ~ 146 fs timescale. It therefore seems unlikely that these states explain the low kinetic energy H-atom appearance times that have been measured here.

Recent measurements by Devine et al. in thiophenol²¹ have shown that, following excitation above the S_1/S_2 CI, both the ground and electronically excited phenylthiyl radicals (C_6H_5S , \tilde{X} - and \tilde{A} -state respectively) were formed. The fastest H-

atoms resulting from the \tilde{X} -state C_6H_5S showed a recoil anisotropy of $\beta_2 \approx -0.45$, whereas the slower H-atoms appeared more isotropic. While the β_2 associated with the fastest H-atoms corresponding to \tilde{A} -state C_6H_5S was also expected to give a negative β_2 , the larger isotropic contribution from highly excited \tilde{X} -state C_6H_5S fragments with the same total kinetic energy washed out any anisotropy.

The persistence of a positive, non-limiting β_2 at low kinetic energies can also be explained on the basis that the measurements on phenol-d5, both ground and electronically excited phenoxy-d5 radicals (C_6D_5O) are formed. As in thiophenol, \tilde{A} -state C_6D_5O is also expected to give a partially positive β_2 , subject to masking by any isotropic contribution from highly excited \tilde{X} -state C_6D_5O with the same total kinetic energy (which could also explain the increased error bars). Interestingly, the A-state of C_6H_5O lies $\sim 8900\text{ cm}^{-1}$ above the ground state as compared to the \tilde{A} -state of C_6H_5S $\sim 2800\text{ cm}^{-1}$. Therefore, given that branching to the \tilde{A} -state asymptote is expected to occur at the S_0/S_2 CI, it is expected that \tilde{X} and \tilde{A} -state products to be formed with similar internal excitation, determined much nearer the Franck-Condon region. This would lead one to expect \tilde{A} -state products to peak at $\sim 2700\text{ cm}^{-1}$ ($11600 - 8900\text{ cm}^{-1}$), in good agreement with the observed peak centre (clearly displayed by the lower kinetic energy peak in figure 4.2 and β_2 in figure 4.6). As a result of the increased $\tilde{A} \leftarrow \tilde{X}$ separation in phenol relative to thiophenol, the S_0/S_2 CI in phenol occurs at a much shorter R_{X-H} bond distance. This results in a much steeper gradient at the CI in phenol. This will most likely result in a lower probability for the adiabatic dynamics (as represented by pink curved arrow in figure 3.1, in previous chapter 3) at the S_0/S_2 CI in phenol-d5 that would ultimately lead to excited phenoxy-d5 fragments, reducing the propensity for excited state products, which

could explain the observed peak intensity ratio between the low and high kinetic energy H-atoms shown in figure 4.2(b).

Further evidence that the low kinetic energy component of the spectrum is due to A-state phenoxy-d5 comes from measuring different timescales of dissociation for the low and high kinetic energy components. As shown in figures 4.4(a) and 4.4(b), the H^+ transients clearly show two different time constants of $146 \text{ fs} \pm 25 \text{ fs}$ and $88 \text{ fs} \pm 30 \text{ fs}$ (solid black line) for the slow and fast H-atoms respectively. The different timescales can once again be rationalized based on the competing adiabatic vs. non-adiabatic dynamics at the S_0/S_2 CI. For dissociation to occur adiabatically and to yield electronically excited phenoxy-d5 fragments, the wavepacket will undoubtedly decelerate as it avoids the CI and begins climbing up the potential energy surface to dissociate adiabatically at the \tilde{A} -state asymptote. This simple classical picture can be used to rationalize the factor of ~ 2 difference in timescales observed. Indeed, a factor of 4 difference in the kinetic energies of the two exit channels translates to a factor of 2 difference in the velocities and hence the timescales, in very good agreement with the measured value. Both models support the rationale that \tilde{A} -state phenoxy-d5 fragments are responsible for the low kinetic energy H-atoms which, owing to their direct nature, display positive, non-limiting β_2 .

It is important to mention that recently, while exciting phenol-d5 molecules at 193 nm, TKER measurements by King et al.²² have revealed another pathway for H-atom elimination, not observed in their previous measurements at 206 nm. This channel yields a structured signal at $\sim 5500 \text{ cm}^{-1}$ in the TKER spectrum and is attributed to the formation of vibrationally cold C_6D_5O co-fragments in their second excited state (\tilde{B} -state). This suggests the existence of another CI at extended R_{O-H} at

an excitation energy of ~ 6.4 eV providing a route from the optically bright S_3 state to another higher $^1\pi\sigma^*$ state, which correlates with the phenoxy B-state. CASPT2 calculations in the same work revealed that the onset of this channel occurs at ~ 6.4 eV, where the S_3 and upper $^1\pi\sigma^*$ state intersect. With the measurements performed here, while pumping phenol-d5 molecules at 200 nm (~ 6.2 eV), if it is assumed that this channel is accessible by tunnelling, internally cold C_6D_5O fragments in their B-state would result in a peak at ~ 4000 cm^{-1} . Whilst the relatively poor resolution attached to femtosecond time-resolved measurements and VMI spectrometer, in comparison to the H Rydberg atom photofragment translational spectroscopy method and the threshold nature of this channel at 200 nm prohibits clear identification of this channel, it must result in at most a minor contribution to the low kinetic energy signal at 200 nm. It seems most likely that the threshold energy for the $S_3/^1\pi\sigma^*$ CI has not been achieved and the channel remains closed.

4.4. Epilogue

The competition between statistical vs. non-statistical deactivation pathways in hetero-aromatics has been the subject of increasing interest in the very recent literature. One of the contributing factors that has fuelled such curiosity is the presence of optically dark $^1\pi\sigma^*$ states. The $^1\pi\sigma^*$ states are dissociative along the X-H coordinate, where X is typically N or O, leading to H-atoms with high kinetic energies. However, additional low kinetic energy H-atoms are often released in these photolysis experiments. Using a combination of femtosecond pump-probe spectroscopy and VMI, the work presented in this chapter has shown the ability to

clock the real-time dissociation of the O-H bond in phenol-d5, following excitation of the optically bright S_3 state at 200 nm. From these measurements, it is inferred that direct H-atoms with high kinetic energies form with a time-constant of $88 \text{ fs} \pm 30 \text{ fs}$, in a non-statistical decay route involving passage through or around three successive CIs (S_3/S_2 , S_1/S_2 and S_0/S_2) to form $\text{H} + \text{C}_6\text{D}_5\text{O}$ in its electronic ground state. The H-atoms with lower kinetic energy, rising with a time-constant of $146 \text{ fs} \pm 25 \text{ fs}$ also appear to form via a non-statistical decay route, involving the same decay pathway, but leading to electronically excited phenoxy-d₅ radicals due to branching induced by adiabatic dynamics in the region of the final (S_0/S_2) CI. Whether these slow H-atoms are a result of the phenoxy co-fragment being formed electronically excited, or are due to multiphoton processes and superexcited states, is still open to debate. This work seems to favour the former interpretation given previous work on thiophenol, the known term value for the $\tilde{A} \leftarrow \tilde{X}$ transition in phenoxy and the anisotropy measurements. Non-limiting, positive β_2 for low kinetic energy H-atoms bring into question the presence of indirect dynamics, thus ruling out the possibility of these H-atoms being associated with single photon unimolecular decay leading to hot ground state phenoxy radicals. The appearance of these H-atoms at a timescale of 146 fs also suggests direct dynamics prevail, ruling out a statistical pathway for the O-H bond fission. It is still possible that ring H-atoms may dissociate statistically although the similarity of the phenol-d5 and phenol-h6 data leads one to suspect this channel is at most a minor one.

Multiphoton processes, mediated by superexcited states may be operative given the pump wavelength used here, 200 nm, although multiphoton absorption will lead to excitation well-above the ionization potential, increasing the autoionisation

rate and reducing the likelihood of direct dynamics from these states. Furthermore, one might expect extremely high kinetic energy release following photoexcitation to these neutral states ($25,000 \text{ cm}^{-1}$),²³ in contrast to the observed low kinetic energy release associated with the 146 fs channel.

While these measurements illustrate the need for further high-level calculations, what is clearly evident from this work on phenol-d5 is the appearance of low kinetic energy H-atoms, which might previously have been attributed to some single photon statistical pathway, should be interpreted in terms of direct processes, most likely leading to excited state phenoxy-d₅ products. In fully hydrogenated systems, the low kinetic energy H⁺ signals are often enhanced and take on a typical ‘statistical decay’ kinetic energy profile. It seems likely that these signals are multi-component and comprise of multiphoton statistical decay, which may occur with a rather longer time constant, in addition to ‘direct channels’ leading to excited state products. The combination of time *and* energy resolved VMI with selective deuteration of the aromatic ring has made it possible to disentangle these contributions in phenol-d5 and confirm the direct dynamical nature²⁴ of the low kinetic energy channel in C₆D₅OH photolysis at 200 nm.

It also seems instructive to compare the results obtained by combining ultrafast time-resolved spectroscopy with TOF-MS and VMI. In chapter 3, time-resolved TOF-MS suggested that O-H bond dissociation in phenol following excitation at 200 nm occurred within $103 \text{ fs} \pm 30 \text{ fs}$. As presented in this chapter, the time-resolved VMI gave H⁺ transients in energy *and* time-resolved fashion and suggested that the O-H bond dissociation resulting in high and low kinetic energies occurred in $88 \text{ fs} \pm 30 \text{ fs}$ and $146 \text{ fs} \pm 25 \text{ fs}$, respectively. For these timescales the

integrals were obtained at the peaks heights of the high and low kinetic energies and the integrals widths were $\sim 1000 \text{ cm}^{-1}$. If the kinetic energy spectra at various pump-probe delays is integrated over the entire range of kinetic energies, the time constant will be again $\sim 100 \text{ fs}$ which agrees very well with the value of $103 \text{ fs} \pm 30 \text{ fs}$ obtained using time-resolved TOF-MS. This illustrates, as one would expect, that both techniques (time-resolved TOF-MS and VMI) give the same overall result with one major difference, which is, that VMI enables one to disentangle different dissociation paths, serving to validate the critically important extra dimension afforded by energy.

4.5. References

- (1) Sobolewski, A. L.; Domcke, W.; Dedonder-Lardeux, C.; Juvet, C. *Phys. Chem. Chem. Phys.* **2002**, *4*, 1093.
- (2) Lan, Z.; Domcke, W.; Vallet, V.; Sobolewski, A. L.; Mahapatra, S. *J. Chem. Phys.* **2005**, *122*, 224315.
- (3) Ashfold, M. N. R.; Cronin, B.; Devine, A. L.; Dixon, R. N.; Nix, M. G. D. *Science* **2006**, *312*, 1637.
- (4) Kimura, K.; Nagakura, S. *Mol. Phys.* **1965**, *9*, 117.
- (5) Ashfold, M. N. R.; Devine, A. L.; Dixon, R. N.; King, G. A.; Nix, M. G. D.; Oliver, T. A. A. *PNAS* **2008**, *105*, 12701.
- (6) Tseng, C. M.; Lee, Y. T.; Ni, C. K. *J. Chem. Phys.* **2004**, *121*, 2459.
- (7) Tseng, C. M.; Lee, Y. T.; Ni, C. K.; Chang, J. L. *J. Phys. Chem. A* **2007**, *111*, 6674.

- (8) Tseng, C. M.; Lee, Y. T.; Lin, M. F.; Ni, C. K.; Liu, S. Y.; Lee, Y. P.; Xu, Z. F.; Lin, M. C. *J. Phys. Chem. A* **2007**, *111*, 9463.
- (9) Vieuxmaire, O. P. J.; Lan, Z.; Sobolewski, A. L.; Domcke, W. *J. Chem. Phys.* **2008**, *129*, 224307.
- (10) Hause, M. L.; Yoon, Y. H.; Case, A. S.; Crim, F.F. *J. Chem. Phys.* **2008**, *128*, 104307.
- (11) Lippert, H.; Ritze, H.-H.; Hertel, I. V.; Radloff, W. *ChemPhysChem*. **2004**, *5*, 1423.
- (12) Iqbal, A.; Pegg, L.-J.; Stavros, V. G. *J. Phys. Chem. A* **2008**, *112*, 9531.
- (13) Even, U.; Jortner, J.; Noy, D.; Lavie, N.; Cossart-Magos, C. *J. Chem. Phys.* **2000**, *112*, 8068.
- (14) Eppink, A. T. J. B.; Parker, D. H. *Rev. Sci. Instrum.* **1997**, *68*, 3477.
- (15) Roberts, G. M.; Nixon, J. L.; Lecointre, J.; Wrede, E.; Verlet, J. R. R. *Rev. Sci. Instrum.* **2009**, *80*, 053104.
- (16) Nix, M. G. D. *Private Communication*.
- (17) Nix, M. G. D.; Devine, A. L.; Cronin, B.; Dixon, R. N.; Ashfold, M. N. R. *J. Chem. Phys.* **2006**, *125*, 133318.
- (18) Frisch, M. J.; Trucks, G. W.; Schlegel, H. B.; Scuseria, G. E.; Robb, M. A.; Cheeseman, J. R.; Montgomery, J. A., Jr.; Vreven, T.; Kudin, K. N.; Burant, J. C.; Millam, J. M.; Iyengar, S. S.; Tomasi, J.; Barone, V.; Mennucci, B.; Cossi, M.; Scalmani, G.; Rega, N.; Petersson, G. A.; Nakatsuji, H.; Hada, M.; Ehara, M.; Toyota, K.; Fukuda, R.; Hasegawa, J.; Ishida, M.; Nakajima, T.; Honda, Y.; Kitao, O.; Nakai, H.; Klene, M.; Li, X.; Knox, J. E.; Hratchian, H. P.; Cross, J. B.; Bakken, V.; Adamo, C.; Jaramillo, J.; Gomperts, R.; Stratmann, R.

E.; Yazyev, O.; Austin, A. J.; Cammi, R.; Pomelli, C.; Ochterski, J. W.; Ayala, P. Y.; Morokuma, K.; Voth, G. A.; Salvador, P.; Dannenberg, J. J.; Zakrzewski, V. G.; Dapprich, S.; Daniels, A. D.; Strain, M. C.; Farkas, O.; Malick, D. K.; Rabuck, A. D.; Raghavachari, K.; Foresman, J. B.; Ortiz, J. V.; Cui, Q.; Baboul, A. G.; Clifford, S.; Cioslowski, J.; Stefanov, B. B.; Liu, G.; Liashenko, A.; Piskorz, P.; Komaromi, I.; Martin, R. L.; Fox, D. J.; Keith, T.; Al-Laham, M. A.; Peng, C. Y.; Nanayakkara, A.; Challacombe, M.; Gill, P. M. W.; Johnson, B.; Chen, W.; Wong, M. W.; Gonzalez, C.; Pople, J. A. *Gaussian 03*, revision B.04; Gaussian, Inc.: Pittsburgh, PA, 2003.

(19) Schick, C. P.; Weber, P. M. *J. Phys. Chem. A* **2001**, *105*, 3725.

(20) Lipert, R. J.; Colson, S. D. *J. Chem. Phys.* **1990**, *92*, 3240.

(21) Devine, A. L.; Nix, M. G. D.; Dixon, R. N.; Ashfold, M. N. R. *J. Phys. Chem. A* **2008**, *112*, 9563.

(22) King, G. A.; Oliver, T. A. A.; Nix, M. G. D.; Ashfold, M. N. R. *J. Phys. Chem. A* **2009**, *113*, 7984.

(23) Devine, A. L.; Nix, M. G. D.; Cronin, B.; Ashfold, M. N. R. *Phys. Chem. Chem. Phys.* **2007**, *9*, 3749.

(24) Iqbal, A.; Cheung, M. S. Y.; Nix, M. G. D.; Stavros, V. G. *J. Phys. Chem. A* **2009**, *113*, 8157.

Chapter 5

Exploring the Timescales of H-atom Elimination from Photoexcited Indole

A combination of femtosecond pump-probe spectroscopy and velocity map ion imaging (VMI) techniques has been implemented to study time and energy resolved photoinduced H-atom elimination, following excitation at 200 nm of indole molecules. After excitation above the S_1/S_2 conical intersection, photoinduced N-H bond cleavage results in a range of H-atom kinetic energy release. H-atoms with large amounts of kinetic energy are attributed to direct dissociation while those with low kinetic energy were attributed to indirect pathways such as statistical unimolecular decay. The results show that H-atoms with both high *and* low kinetic energies are generated on an ultrafast timescale < 200 fs, suggesting a direct route to H-atom formation yielding H-atoms with low kinetic energies.

5.1. Prologue

As described in Chapters 3 and 4, the photochemistry of biological chromophores, for example nucleic bases and amino acids, is controlled by the various relaxation mechanisms following initial ultraviolet (UV) excitation.¹⁻⁵ The focus of this chapter is on the photophysics of indole, the chromophore of the amino acid tryptophan, which has been a topic of recent interest as it is a precursor to unravelling the relaxations pathways of tryptophan. The amino acid tryptophan, itself is considered an important fluorescence probe in proteins for many spectroscopic investigations. Identifying these pathways in the chromophore and relating them to its electronic structure will undoubtedly assist in the transition from the micro (chromophore) to the macro (solvated amino acid and beyond) and to eventually understanding the photochemistry of these biomolecules *in vivo*.

5.1.1. Potential Energy Profiles of Indole along N-H

Coordinate

Indole has two absorption bands in the near UV, and these are assigned to $\pi^* \leftarrow \pi$ transitions. These two excited states are traditionally labelled as 1L_a and 1L_b states. The 1L_b state has a strong transition at 283.78 nm⁶ and lies about 1400 cm⁻¹ below the 1L_a state.⁷⁻¹⁰ Sobolewski and Domcke¹¹ have shown that the lowest singlet ${}^1\pi\sigma^*$ (S_2) state has repulsive character along the N-H coordinate intersecting the bound 1L_a and 1L_b (${}^1\pi\pi^*$) ((S_1)) states as well as the ground (S_0) state, providing a route for non-radiative decay. Their *ab initio* calculations have shown that the low

fluorescence quantum yield of indole following excitation above the S_1/S_2 conical intersection (CI) is due to the S_2 state that can lead to the elimination of an H-atom as a non-radiative product.¹¹ The potential energy surfaces (PES) of indole along N-H coordinate are presented in figure 5.1.

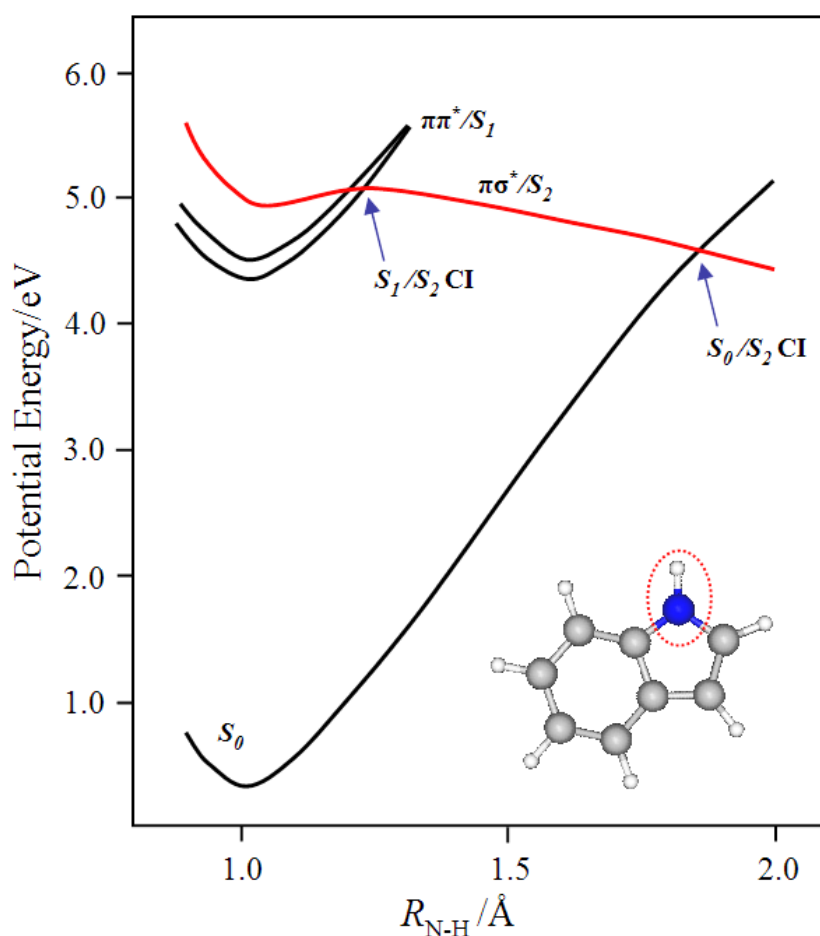


Figure 5.1 Potential energy profiles of the lowest ${}^1\pi\pi^*$ (S_1), ${}^1\pi\sigma^*$ (S_2) and the electronic ground state (S_0) as a function of N-H stretch reaction coordinate of indole. These PESs have been adapted from Sobolewski et al.¹¹ and redrawn to scale for illustrative purposes.

Due to the small energy gap between the 1L_a and 1L_b states, the vibronic coupling is predicted to be very strong¹² and it is assumed that both these states can

be excited simultaneously. Owing to the weak $S_2 \leftarrow S_0$ transition, the S_2 state is not excited directly (optically dark) and is populated by radiationless transfer from the optically bright S_1 state via the S_1/S_2 CI.¹³ Once on the S_2 state, its repulsive nature along the N-H coordinate means that excited indole molecules evolve towards the S_0/S_2 CI resulting in either direct photodissociation to yield H-atoms with large amounts of kinetic energy or population of vibrationally excited indole (S_0) molecules. In much the same way as discussed in phenol (chapters 3 and 4), these ‘hot’ ground state molecules can undergo statistical unimolecular decay resulting in further H-atoms, albeit with much less kinetic energy.

5.1.2. Photoinduced N-H Bond Cleavage in Indole and its Timescales

Timescales of H-atom elimination from these systems are of obvious importance to develop a better understanding about how potential PESs couple with one-another and the role of the CIs. In addition, the ability to determine any trends in these biomolecules from an electronic standpoint would also be invaluable as the knowledge gained from these studies can then be applied to other biomolecules and predictions can also be made. In an effort to carry this out, this chapter focuses on the application of time-resolved velocity map ion imaging (VMI) for H-atom elimination as a function of kinetic energy release in indole. Due to the repulsive nature of the S_2 state, direct dissociation via the S_1/S_2 and S_0/S_2 CIs, in indole is known to produce H-atoms with large amounts of kinetic energy, while indirect dissociation via hot ground state molecules leads to H-atoms with much less kinetic energy. As discussed

in chapter 4, VMI enables one to disentangle these two pathways because H-atoms with varying amounts of kinetic energy can be separated from the ion-image obtained. The work described herein reveals that for *all* kinetic energy ranges, N-H bond dissociation occurs on an ultrafast (< 200 fs) timescale within the timeframe of these measurements (< 200 ps), in stark contrast to the timescale expected for low kinetic energy H-atoms born from a statistical unimolecular decay pathway. This suggests that while vibrationally excited indole (S_0) molecules may undergo unimolecular decay on a much longer timescale, as recently reported through multimass ion-imaging measurements,¹⁴ an additional route to low kinetic energy H-atoms is also operative, which is direct in nature.

5.1.3. A Brief Overview of N-H bond Dissociation

Dynamics in Indole

The photo-induced H-atom elimination from indole through the S_2 state was first reported by Lin et al.¹⁴ using multimass ion-imaging. Following photoexcitation at 248 nm and 193 nm the H-atom elimination was suggested to occur through two pathways: The H-atoms with high kinetic energy were attributed to direct coupling of the S_1 and ground state with the S_2 state at the S_1/S_2 and S_0/S_2 CIs respectively. The second pathway resulted in low kinetic energy H-atoms and the dissociation was assumed to occur following internal conversion to ground (S_0) state. According to these authors, 80 % of indole dissociated from the electronically excited state after photoexcitation at 248 nm, while photoexcitation at 193 nm resulted in 54% of dissociation occurring from electronically excited state. As the excitation energy

increased the rate of internal conversion to the ground state increased, apparently due to the increase in the density of states at higher energies, thus enhancing the low kinetic energy H-atom elimination channel. They established a dissociation rate of $6 \times 10^{-5} \text{ s}^{-1}$, corresponding to statistical dissociation on the ground (S_0) state.

Following this, Nix et al.¹⁵ measured the total kinetic energy release (TKER) by H-atoms following excitation of indole molecules above the S_1/S_2 CI and reported that the high kinetic energy H-atoms were attributed to direct coupling of the PES at the S_1/S_2 and S_0/S_2 CIs, in agreement with Lin et al.¹⁴ However, the low kinetic energy H-atoms observed in their measurements could not be attributed only to one-photon dissociation of vibrationally excited indole (S_0) molecules but also to H-atoms generated by one or more multiphoton processes through resonance excitation of the 1L_a and 1L_b states.

This chapter presents time-resolved H-atom elimination measurements with both time *and* energy resolution following excitation of indole molecules at 200 nm and probing H-atoms through (2 + 1) resonance enhanced multiphoton ionization (REMPI). Time-resolved VMI makes it possible to separate H-atoms carrying various amounts of kinetic energies and help to obtain timescales for the pathways through which these are eliminated. The measurements performed here show that H-atoms with high kinetic energy are attributed to dissociation along the S_2 state leading to H-atoms and the partner indolyl fragments in their electronic ground state. H-atoms with low kinetic energy are attributed to multiphoton, direct processes and possibly direct dissociation leading to indolyl fragments in the electronically excited state and not through statistical unimolecular decay of vibrationally excited indole (S_0) molecules. This work once again suggests that while unimolecular decay may

yield H-atoms with low kinetic energy, this is not the only source of such H-atoms, in agreement with recent TKER measurements and the studies on the comparative system, phenol, as described in chapters 3 and 4.

5.2. The Experiment

The experimental setup has been described in detail in chapter 2 and 4. Briefly, the indole molecules were excited at 200 nm, which was obtained by doubling the fundamental 800 nm output from the SP amplifier and then frequency up-converting this through various optical mixing processes. The resulting 200 nm has an energy of approximately 1 μJ /pulse. The eliminated H-atoms were detected with the help of 243.1 nm pulses (6-7 μJ /pulse) via (2 + 1) REMPI and were generated from the TOPAS UV system. The optical delay between the pump and probe is varied over 4 picoseconds (ps) with a minimum step size of 0.025 ps.

The molecular beam is generated by seeding a vapour pressure of indole (Sigma-Aldrich, indole $\geq 99\%$) molecules in He (2-3 psi and 70 °C) and is sent into vacuum using an Even-Lavie¹⁸ valve operating at 500 Hz and synchronized to the laser system. By changing the delay between the pump and probe pulses, 2D images of H⁺ are obtained with the help of the VMI setup¹⁹ at each delay. These images are then deconvoluted with the help of the POP²⁰ program to obtain kinetic energy spectra.

5.3. Time-of-Flight Mass Spectrum

Figures 5.2(a) and 5.2(b) present the time-of-flight mass spectrum (TOF-MS) of indole obtained following photoionization by only the pump (200 nm) and both the pump and probe (200 nm and 243.1 nm), respectively. In figure 5.2(b) the parent indole⁺ ($m/z = 117$) signal is not shown, gated to avoid saturation of the MCP's with the help of deflector plates. As mentioned above due to two adjacent $^1\pi\pi^*$ states, indole has a very large absorption cross-section and thus when 243.1 nm is added in addition to the 200 nm, the signal intensity rises sharply, particularly the parent indole⁺. The delay between the pump and probe pulses was set to 2 ps. In all the measurements described in this chapter the intensity of 200 nm was adjusted such that minimum fragmentation of the parent indole was observed, thus reducing the other pathways of H-atom production with the pump alone, such as through fragmentation. In figure 5.2(a) a strong signal at $m/z = 117$, corresponds to parent indole⁺, in addition to a peak at $m/z = 90$ that corresponds to $C_7H_6^+$. However, there is no peak observed at $m/z = 1$. In contrast to figure 5.2(a), when the pump is followed by probe, figure 5.2(b) reveals a peak at $m/z = 1$ that corresponds to H^+ . Figure 5.2(b) also reveals another peak at $m/z = 27$ (HCN^+) in addition to a peak at $m/z = 90$ ($C_7H_6^+$). These observations are consistent with Nix et al.¹⁵ who suggest that after pump laser excitation the indole⁺ loses HCN whose partner fragment is C_7H_6 . The $C_7H_6^+$ can further lose H-atom through statistical unimolecular decay leaving $C_7H_5^+$ ($m/z = 89$). These observations will be discussed in detail in proceeding paragraphs.

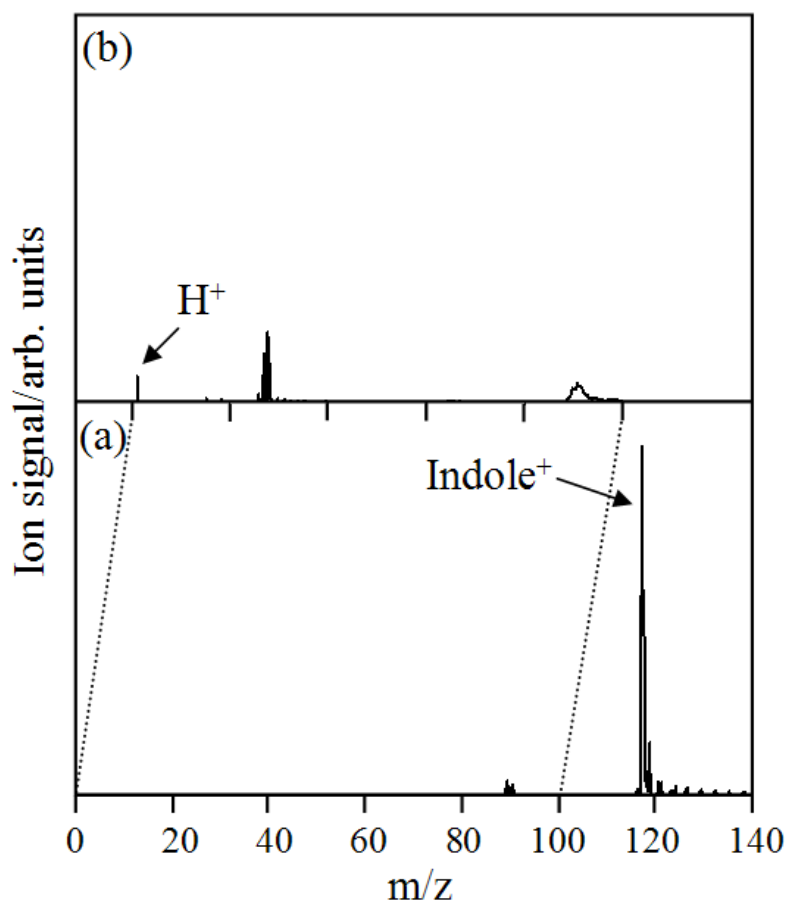


Figure 5.2 One- and two-colour TOF-MS recorded at (a) pump (200 nm) and (b) pump + probe (200 nm + 243.1 nm), respectively. The delay between the pump and probe was set at 2 ps.

5.4. The Raw Images of H⁺ After N-H Bond

Cleavage

Figure 5.3 shows raw VMI images for two pump-probe delays. Both images have been cut through the centre and re-scaled merely for illustrative purposes. Figure 5.3(a) corresponds to a pump-probe delay (t) of -0.5 ps, i.e. the probe precedes the pump while figure 5.3(b) corresponds to a pump-probe delay (t) of +2.0

ps, the probe delayed relative to the pump. Whilst not apparent from figure 5.3 due to the rescaling, there is substantially more ion signal when the pump precedes the probe (approximately 3 times more), indicative of probing H-atoms through (2 + 1) REMPI following photodissociation.

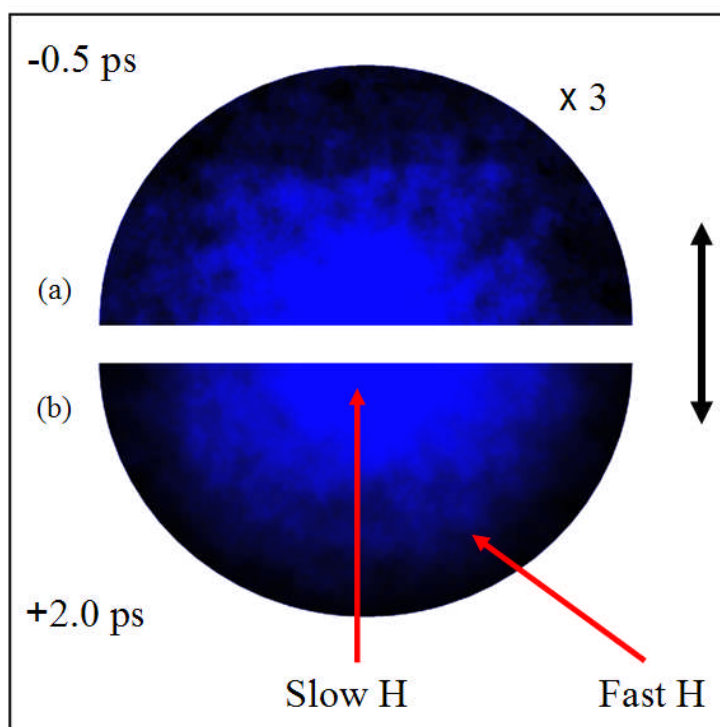


Figure 5.3 Raw H^+ images following photodissociation at 200 nm and probing with 243.1 nm. Only half of each image is shown for illustrative purposes for pump-probe delays (t) of -0.5 ps and +2.0 ps, (a) and (b) respectively.

As can be inferred from figure 5.3, even at a delay of 2 ps between the pump and probe, there is considerable H^+ signal at all radii of the image, i.e. at all kinetic energies. The inner part of the image relates to H-atoms that carry very low kinetic energy following photodissociation while those at the outer part of the image are born with very large amounts of kinetic energy. There is no apparent boundary

connecting these two kinetic energy regimes but merely a smooth transition between the two regions exists, reflected in the kinetic energy spectra shown in figure 5.4 (see section 5.4.1). Following from previous discussions in the literature, the inner part of the image can be attributed to H-atoms formed as a result of either unimolecular decay of highly vibrationally excited indole molecules or as a result of multiphoton processes. The outer part of the image represents the energetic H-atoms born through direct dissociation via the S_2 state.

Unlike in phenol, as described in chapter 4, the images do not appear to exhibit any angular anisotropy.¹⁶ The anisotropy parameter measured is approximately $\beta_2 \approx 0$ at all kinetic energies, i.e. isotropic. TDDFT and CASSCF²¹ calculations suggest that the transition dipoles for the $S_1 \leftarrow S_0$ transitions (i.e. to 1L_a and 1L_b states) lie in the molecular plane but orthogonal to one-another. Even though prompt dissociation should preserve the initial recoil anisotropy, this smears-out owing to the orthogonal transition dipole moments of the 1L_a and 1L_b states, as evident in figure 5.3. It is important to stress that detuning the TOPAS output from the resonance $2s \leftarrow 1s$ in the H-atom reduces the H^+ signal substantially at all kinetic energies indicating H-atoms are being probed rather than nascent H^+ ions generated directly from some dissociative ionization and/or multiphoton fragmentation process. In the later paragraphs, the origin of the different kinetic energy regimes will be discussed in detail.

5.4.1. Kinetic Energy Spectrum of H-atoms

Figure 5.4 gives the H^+ transient as a function of H-atom kinetic energy at various pump-probe delays. The dotted, dashed and solid lines correspond to pump-probe delays (t) of -0.5, 0 and 2 ps respectively. When the pump pulses are preceded by the probe pulses, the H^+ signal is shown by the dotted line and is dominated by probe alone signal. The dashed line represents the H^+ signal at $t = 0$, when the pump and probe pulses are temporally overlapped. After $t = 0$ the signal continues to grow and remains unchanged beyond 600 fs, persisting up to pump-probe delay of 3.5 ps. A representative example is shown by the solid line that corresponds to a pump-probe-delay (t) of 2 ps. It is clear from the solid trace that the whole kinetic energy spectrum is dominated by a broad feature that extends out to $\sim 11000\text{ cm}^{-1}$. However, it indicates two features peaking at 1500 cm^{-1} and 7000 cm^{-1} which are referred to hereon as low and high kinetic energy H-atoms, respectively.

It is also clear from figure 5.4 that there is a considerable increase in the H^+ signal for both the low and high kinetic energy H-atoms at positive pump-probe delays; the former occurring much faster than what one would predict assuming a statistical unimolecular decay process. The shape of the KE spectrum agrees reasonably well with that reported by Nix et al.¹⁵ obtained using nanosecond (ns) single photon dissociation, following excitation above the S_1/S_2 CI. The difference between the kinetic energy spectra obtained in the ns work and the present work will be discussed in further detail in the proceeding paragraphs.

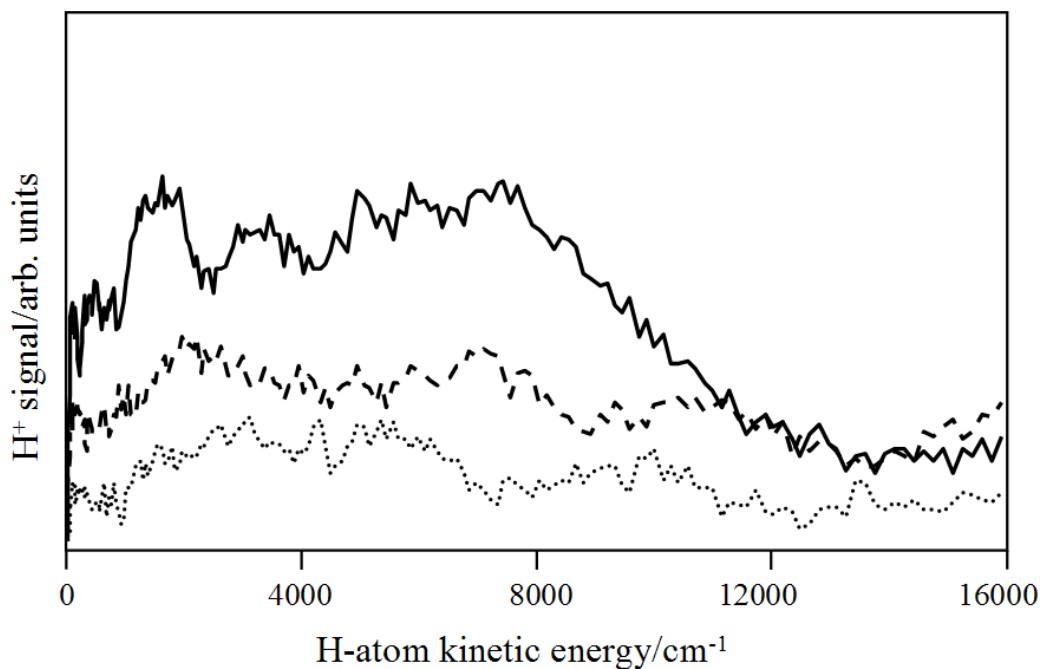


Figure 5.4 H^+ transients as a function of H-atom kinetic energy. The dotted, dashed and solid lines correspond to pump (200 nm)-probe (243.1 nm) delays (t) of -0.5, 0 and 2 ps respectively.

5.4.2. Timescales for N-H Bond Photolysis

Real-time N-H bond dissociation in indole following photoexcitation at 200 nm and probing the H-atoms is shown in figure 5.5. The error bars are obtained assuming two standard deviations of the mean representing a 95 % confidence limit. It is also worth mentioning here that the data reported in figures 5.5 is normalized. The H^+ transient signals were obtained by collecting a series of kinetic energy spectra at various pump-probe delays (t) and integrating the H^+ signal across different portions of the kinetic energy spectrum. Figure 5.5(b) corresponds to the integral obtained at the maximum of the high kinetic energy peak at 7000 cm^{-1} and figure 5.5(a) corresponds to the integrated intensity at the low kinetic energy peak at

1500 cm^{-1} (the integral widths are approximately 1000 cm^{-1}). Both parts of figure 5.5 indicate that at $t < 0$, no appreciable two-colour H^+ signal is observed, but at $t > 0$ the H^+ signal rises sharply and plateaus after 600 fs, remaining unchanged up to delays of 3.5 ps.

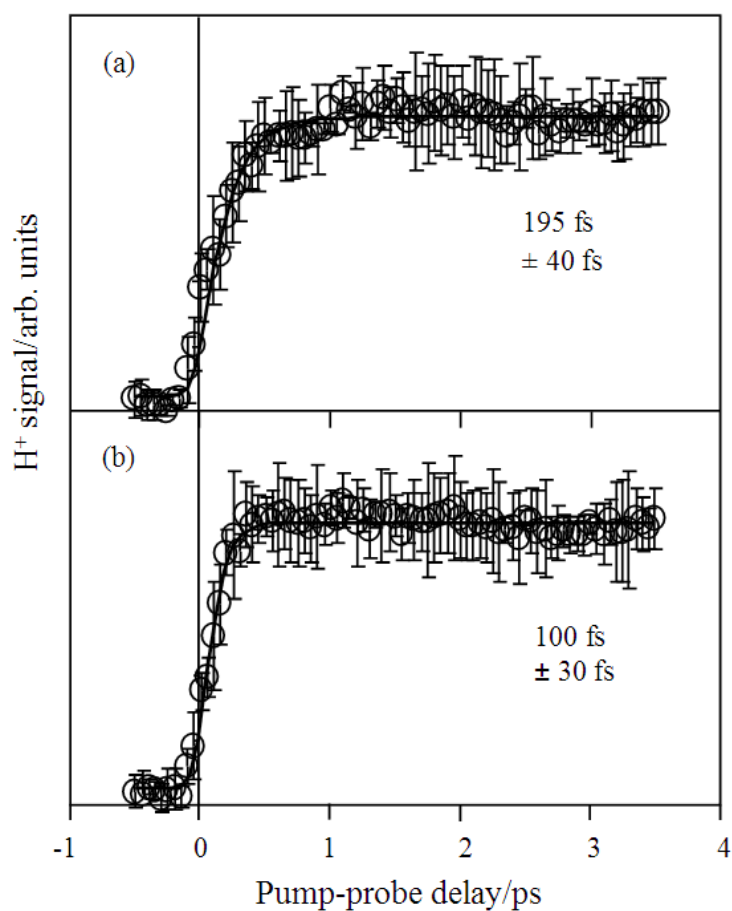


Figure 5.5 H^+ transients as a function of pump (200 nm)-probe (243.1 nm) delay for the low kinetic energy (a) and high kinetic energy (b) H-atoms in indole together with corresponding fits.

Fitting these time traces with an exponential rise function convolved with a instrument response function (Gaussian, FWHM 160 fs) suggests time constants of

100 fs \pm 30 fs for the high kinetic energy H-atoms (peaking at 7000 cm⁻¹) and 195 fs \pm 40 fs for the low kinetic energy H-atoms (peaking at 1500 cm⁻¹). Both transients clearly demonstrate that N-H bond dissociation occurs on an ultrafast timescale (< 200 fs).

The N-H bond dissociation lifetime for a range of kinetic energies is illustrated by figure 5.6. This figure gives some further insights into the timescales of H-atom elimination and the extracted time-constants suggest that following excitation at 200 nm, dissociation is very likely occurring along a direct path. Figure 5.6 also shows that even at the very lowest kinetic energies resolvable in these measurements, the appearance time of slow H-atoms is approximately 200 fs.

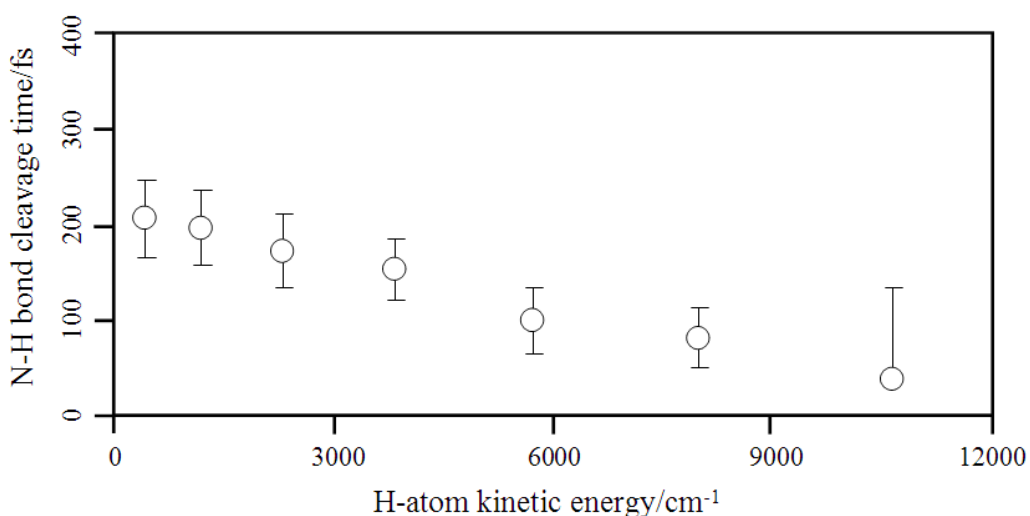


Figure 5.6 N-H bond dissociation as a function of H-atom kinetic energy following excitation of indole at 200 nm and probing H-atoms via (2 + 1) REMPI at 243.1 nm.

If these H-atoms are dissociating through vibrationally excited indole (S₀) molecules, the ensuing statistical unimolecular decay would result in a microsecond-long¹⁴ process which clearly is not the case here. The above mentioned results are in sharp

contrast to the work of Lin et al.¹⁴ who in the absence of time-resolved measurements attribute the low kinetic energy feature in their multi-mass ion imaging as being a result of dissociation through hot parent molecules.

5.4.2.1. Discussion

The observation of a fast component peaking at 7000 cm^{-1} can be rationalized with the argument that after excitation above the S_1/S_2 CI, the S_2 state is populated through the S_1/S_2 CI. Since the S_2 state has repulsive character with respect to the N-H stretching coordinate, it evolves towards the S_0/S_2 CI leading to elimination of H-atoms. This argument is also consistent with that presented by Lin et al.¹⁴ for their high kinetic energy H-atoms. As pyrrole is the subunit of indole itself, it is instructive to compare these results with the time-resolved measurements by Lippert et al.²² Following excitation at 250 nm, the lowest energy state, now the $^1\pi\sigma^*$ state, can be accessed directly. These authors reported two distinct timescales to H-atom elimination. The fast time constant of 0.1 ps was attributed to direct dissociation due to the repulsive character of the $^1\pi\sigma^*$ state. A second, slower time constant of 1.1 ps represented indirect dissociation, following inflection of the wavepacket on the excited state, populating the electronic ground state and subsequently undergoing unimolecular decay.

Unlike pyrrole, the $^1\pi\sigma^*$ (S_2) state in indole cannot be accessed directly. Following excitation above the S_1/S_2 CI (4.71 eV),¹⁵ as is the case with 200 nm pump photons (6.2 eV), radiationless decay from the initially bright S_1 to the S_2 and subsequent direct dissociation yields high kinetic energy H-atoms with a time-

constant of 100 fs (figure 5.5(b)), in agreement with the fast time constant observed in the pyrrole work. However, the similarity in these measurements ends here as a second, much slower component is clearly absent from the measurements performed here. Whilst the low kinetic energy H-atoms give a time-constant of 195 fs, it is very difficult to rationalize as originating through a much slower indirect channel. In contrast to the work of Lippert et al.,²² inflection of the wavepacket on the excited state in indole is not possible as the total energy of the wavepacket is above the second exit channel (by ~1 eV) which correlates with the first electronically excited state of the indolyl radical (calculated as 1.2 eV above the electronic ground state using TDDFT).²¹ Coupled to the microsecond-long timescales for statistical unimolecular decay reported by Lin et al.¹⁴ this means that an alternative explanation must be sought to explain the origin of these low kinetic energy H-atoms.

Multiphoton excitation via S_1 states generating superexcited states have been shown to display ultrafast dynamics, predissociating to yield H-atoms. As discussed in chapter 4, the photoelectron kinetic energies measured by Schick and Weber following multiphoton excitation via the S_1 state in phenol²³ were rationalized as occurring through autoionisation of superexcited states. These superexcited states, which are located around the ionization potential of phenol, displayed very fast decay dynamics (< 230 fs). Although the valence excitation of indole and phenol are similar, two-photon excitation with 200 nm light (12.4 eV) used here would, as in the case of phenol (chapter 4), result in excitation well above the ionization potential of indole (7.76 eV),²⁴ limiting the role of superexcited states as a source of H-atoms via a predissociation mechanism on a timescale of < 200 fs. As in the case of the work described in chapters 3 and 4, it therefore seems unlikely that these states explain the

appearance times of the low kinetic energy H-atoms. Below two alternative suggestions are offered.

Whilst attributing some of their low kinetic energy H-atoms to statistical unimolecular decay of highly vibrationally excited indole (S_0) molecules, Nix et al.¹⁵ suggest from their TKER measurements that most of the slow H-atoms may originate from multiphoton absorptions, resonance enhanced by the 1L_a and 1L_b states. For example, the photofragmentation of molecular ions (in particular cations) during the pump laser excitation is one possible pathway. One suggested example of this was unimolecular decay of highly internally excited $m/z = 90$ ions (to give $m/z = 89$ and H, as shown in figure 5.2) formed during HCN elimination from the parent ion. Other fragments were also suggested to contribute in the same manner, based on the (TOF-MS) obtained. This pathway can only be operative in these measurements provided the photofragmentation of these ions occurs within the cross-correlation of the laser pulses (160 fs). Whilst these pathways can contribute here, it is important to note that they are likely to be less pronounced than with nanosecond long pump pulses as used by Nix et al.¹⁵ which can also be used to explain the larger signals observed in the kinetic energy spectra by these authors at low kinetic energies as compared to the present work (see figure 4 in reference 15).

The work presented in chapter 4 in phenol for the elimination of low kinetic energy H-atoms (< 150 fs) suggested that these H-atoms could be formed through a direct dissociation process following single photon excitation yielding electronically excited phenoxy fragments.¹⁶ In much the same way; it is plausible that electronically excited indolyl fragments could be formed in these experiments. The different timescales observed for the high and low kinetic energy H-atoms,

100 fs \pm 30 fs and 195 fs \pm 40 fs respectively, can once again be rationalized on the competing adiabatic vs. non-adiabatic dynamics at the S_0/S_2 CI. Adiabatic dissociation yielding electronically excited indolyl fragments will lead to a deceleration of the wavepacket as it avoids the S_0/S_2 CI and climbs back up the PES to dissociate adiabatically at the A-state asymptote. Whilst this pathway is plausible, it is worth noting that the profile of the kinetic energy spectra in phenol (figure 4.2 in chapter 4) contained two distinct peaks at high and low kinetic energies making it much more straightforward to rationalize the low kinetic energy H-atoms with electronically excited phenoxy cofragment coupled to the non-zero anisotropy parameter for both high and low kinetic energy H-atoms. In indole, the entire kinetic energy spectrum is dominated by a broad feature that extends out to ~ 11000 cm⁻¹. As a result, whilst the preceding argument is plausible, it should remain speculative.²⁵

5.5. Epilogue

Understanding the role of the optically dark $^1\pi\sigma^*$ (S_2) state in the excited state dynamics of particular biological chromophores is key to elucidating, in part, the photoresistive properties of the molecule. Its participation is evident in the work presented in this chapter on indole. The H-atoms with high kinetic energy clearly point towards their formation from photodissociation of a highly repulsive PES such as that of a S_2 state. Whilst this non-statistical pathway is understood in this and other similar hetero-aromatics, the role of statistical dynamics is less understood. The measurements presented here show that ultrafast H-atom elimination occurs throughout *all* kinetic energies. Both the high *and* low kinetic energy H-atoms are

formed with a time-constant of $100 \text{ fs} \pm 30 \text{ fs}$ and $195 \text{ fs} \pm 40 \text{ fs}$ respectively. The former is clearly attributed to dissociation involving the S_2 state. The latter is still open to debate. However, this work clearly demonstrates that the low kinetic energy H-atoms observed in these measurements cannot be attributed to an indirect, statistical unimolecular decay pathway. Two explanations are offered for the low kinetic energy H-atoms observed in these measurements, the first based on multiphoton effects and in agreement with TKER measurements whilst the second relates to adiabatic dissociation leading to electronically excited indolyl fragment. However, it is very likely that these low kinetic energy H-atoms are multicomponent in nature. The combination of time and energy resolved VMI clearly shows that low kinetic energy H-atoms are not only formed through an indirect, statistical pathway but are also formed through a direct pathway which is very likely operative in a number of other hetero-aromatics containing an X-H bond.

5.6. References

- (1) Creed, D. *Photochem. Photobiol.* **1984**, *39*, 537.
- (2) Callis, P. R. *Annu. Rev. Phys. Chem.* **1983**, *34*, 329.
- (3) Martinez, T. J. *Acc. Chem. Res.* **2006**, *39*, 119.
- (4) Crespo-Hernandez, C. E.; Cohen, B.; Hare, P. M.; Kohler, B. *Chem. Rev.* **2004**, *104*, 1977.
- (5) Peon, J.; Zewail, A. H. *Chem. Phys. Lett.* **2001**, *348*, 255.
- (6) Lipert, R. J.; Bermudez, G.; Colson, S. D. *J. Phys. Chem.* **1988**, *92*, 3801.
- (7) Fender, B. J.; Sammeth, D. M.; Calls, P. R. *Chem. Phys. Lett.* **1995**, *239*, 31.

- (8) Phillips, L. A.; Levy, D. H. *J. Chem. Phys.* **1986**, *85*, 1327.
- (9) Bersohn, R.; Even, U.; Jortner J. *J. Chem. Phys.* **1984**, *80*, 1050.
- (10) Bickel, G. A.; Demmer, D. R.; Outhouse, E. A.; Wallace, S. C. *J. Chem. Phys.* **1989**, *91*, 6013.
- (11) Sobolewski, A. L.; Domcke, W.; Dedonder-Lardeux, C.; Jouvét, C. *Phys. Chem. Chem. Phys.* **2002**, *4*, 1093.
- (12) Dedonder-Lardeux, C.; Jouvét, C.; Perun, S.; Sobolewski, A. L. *Phys. Chem. Chem. Phys.* **2003**, *5*, 5118.
- (13) Lippert, H.; Ritze, H.-H.; Hertel, I. V.; Radloff, W. *Chem. Phys. Lett.* **2004**, *398*, 526.
- (14) Lin, M.-F.; Tseng, C.-M.; Lee, Y. T.; Ni, C.-K. *J. Chem. Phys.* **2005**, *123*, 1243031.
- (15) Nix, M. G. D.; Devine, A. L.; Cronin, B.; Ashfold, M. N. R. *Phys. Chem. Chem. Phys.* **2006**, *8*, 2610.
- (16) Iqbal, A.; Cheung, M. S. Y.; Nix, M. G. D.; Stavros, V. G. *J. Phys. Chem. A* **2009**, *113*, 8157.
- (17) Wells, K. L.; Perriam, G.; Stavros, V. G. *J. Chem. Phys.* **2009**, *130*, 074308.
- (18) Even, U.; Jortner, J.; Noy, D.; Lavie, N.; Cossart-Magos, C. *J. Chem. Phys.* **2000**, *112*, 8068.
- (19) Eppink, A. T. J. B.; Parker, D. H. *Rev. Sci. Instrum.* **1997**, *68*, 3477.
- (20) Roberts, G. M.; Nixon, J. L.; Lecointre, J.; Wrede, E.; Verlet, J. R. R. *Rev. Sci. Instrum.* **2009**, *80*, 0531041.
- (21) Nix, M.G.D. *Private Communication*.
- (22) Lippert, H.; Ritze, H.-H.; Hertel, I. V.; Radloff, W. *ChemPhysChem.* **2004**, *5*,

1423.

(23) Schick, C. P.; Weber, P. M. *J. Phys. Chem. A* **2001**, *105*, 3725.

(24) Hagger, J. W.; Wallace, S. C. *Anal. Chem.* **1988**, *60*, 5.

(25) Iqbal, A.; Stavros, V. G. *J. Phys. Chem. A* **2010**, *114*, 68.

Chapter 6

Active Participation of $^1\pi\sigma^*$ States in the Photodissociation of Tyrosine and Sub-units

This chapter presents the first evidence of the active involvement of $^1\pi\sigma^*$ states in the H-atom elimination of the amino acid tyrosine and its sub-unit tyramine, following excitation at 200 nm. The H-atom elimination from p-ethylphenol has also been carried out to compare the various features of the H-atom kinetic energy spectra with tyramine and tyrosine. Ultrafast time-resolved pump-probe spectroscopy and velocity map ion imaging (VMI) reveals that ultrafast H-atom elimination occurs following dissociation of the O-H bond in p-ethylphenol after excitation at 200 nm. Timescales of H-atom elimination in tyramine and the kinetic energy features of H-atom spectra in tyrosine also strongly suggest that following excitation at 200 nm, H-atom elimination is occurring through the same coordinate i.e. O-H bond fission as exhibited by the chromophore phenol, thus confirming the active participation of $^1\pi\sigma^*$ states from the chromophore of the amino acid to the amino acid itself.

6.1. Prologue

As discussed in the previous chapters, the photochemistry of the building blocks of life is of critical importance to our existence. The ultimate goal of the body of research described in this thesis is aimed, as suggested by the title of the thesis, towards building a coherent picture of the photochemistry of tyrosine and understanding the underlying non-radiative pathways that diffuse the UV radiation absorbed briskly and efficiently to the surrounding environment before any harmful, i.e. irreversible reactions can occur. A detailed investigation into the photochemistry of phenol, the chromophore of tyrosine discussed in chapters 3 and 4 has already shown the active participation of a dissociative electronic state ($^1\pi\sigma^*$). In chapter 5, it has also been seen that this state is also actively involved in the photochemistry of indole, the chromophore of tryptophan. The question now is whether or not this optically dark state is also contributing non-radiatively to the photochemistry of the amino acid itself.

En route to answering this question, the work described in this chapter takes a step-like approach in which the level of molecular complexity is increased incrementally from p-ethylphenol through to tyramine and ending up with tyrosine itself. In taking this approach, one is then able to pin point any trends emerging and relate this to the photoresistivity of the system of interest. Whilst the aromatic amino acids and their respective chromophores have been subjected to extensive experimental and theoretical investigations both in the gas-phase and condensed-phase, there are still many questions open to debate, some of which hopefully can be addressed with the work presented in this chapter. For the first time using

femtosecond time-resolved spectroscopy and velocity map ion imaging (VMI) following excitation at 200 nm, this chapter reports direct evidence of H-atom elimination from the amino acid tyrosine, which seems to implicate the same decay channels as observed in the chromophore.

6.1.1. Fluorescence Quantum Yields of Tyrosine and its Chromophore

The aromatic amino acid tyrosine has a very large UV absorption cross-section. However, the fluorescence quantum yield of this molecule beyond a certain excitation (< 245 nm) threshold decreases.¹ This is an indication of efficient nonradiative processes, which effectively reduce the fluorescence.^{2,3} These non-radiative processes must be very fast in order to compete effectively with, and overcome, the fluorescence pathway. Phenol, the chromophore of tyrosine, shows a similar pattern in its fluorescence quantum yields. Sobolewski and Domcke⁴⁻⁶ proposed that the low fluorescence quantum yield of phenol and other heteroaromatics containing O/N-H bond is due to an electronically excited singlet $^1\pi\sigma^*$ state, which exhibits a conical intersection (CI) with the lowest electronically excited $^1\pi\pi^*$ state and with the electronic ground state (S_0). As described in previous chapters 3-5, this state transfers population from the optically bright $^1\pi\pi^*$ to the ground state (S_0) giving highly vibrationally excited ground state molecules or alternatively by eliminating neutral H-atoms directly.

6.1.2. Substituted and Unsubstituted Phenols and O-H

Bond Photolysis

The first direct experimental evidence of H-atom elimination in phenol through the $^1\pi\sigma^*$ state was first reported by Tseng et al.^{7,8} using multimass ion-imaging. In an attempt to extend these measurements from phenol to larger and more relevant systems, H-atom elimination in p-methylphenol, p-ethylphenol and in p-(2-aminoethyl) phenol (tyramine) was attempted following excitation at 248 nm using multimass ion-imaging by the same authors.⁹ The evidence of H-atom elimination driven through $^1\pi\sigma^*$ states in p-methylphenol and p-ethylphenol was reported, after excitation at 248 nm. However, H-atom elimination through this state in tyramine was not observed. The authors attributed this to internal conversion and intersystem crossing.⁹

6.1.3. H-atom Abstraction via the O-H Coordinate

In this chapter, the first evidence of H-atoms elimination driven through the $^1\pi\sigma^*$ state in tyramine *and* tyrosine is introduced, following excitation at 200 nm and probing the H-atoms via (2 + 1) resonance enhanced multi-photon ionization (REMPI) by combining ultrafast time-resolved laser spectroscopy and VMI techniques in the gas-phase. The H-atom elimination following excitation at 200 nm from p-ethylphenol has also been carried out to compare the various features of the H-atom kinetic energy spectra and their evolution in time in all three systems. Figure 6.1, parts (a), (b) and (c) presents the structures of p-ethylphenol, tyramine and

tyrosine. Also highlighted for each molecule is the bond of interest which undergoes H-atom elimination.

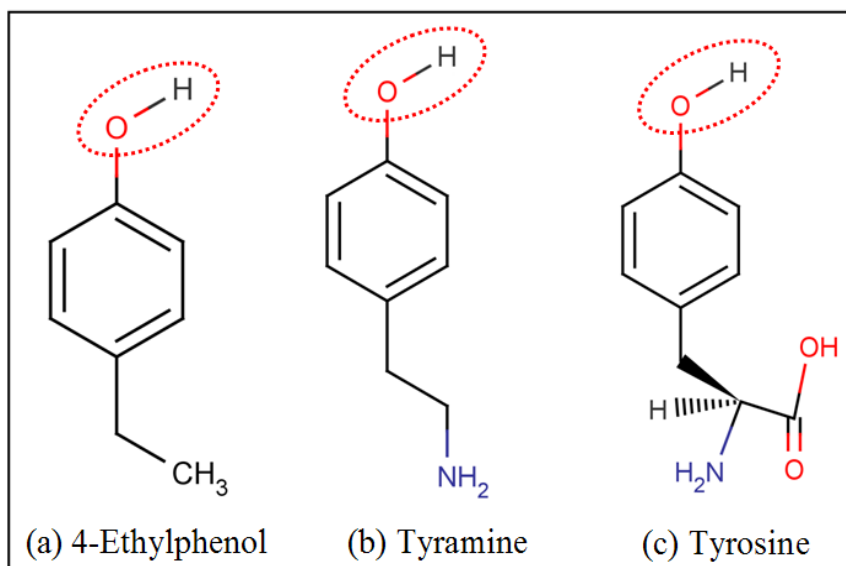


Figure 6.1 Structures of (a) *p*-ethylphenol, (b) tyramine and (c) tyrosine highlighting O-H bond containing labile H-atom.

6.2. The Experiment

The experimental procedure has been described in detail in chapter 2. Briefly, to perform ultrafast time-resolved H-atom elimination measurements in the systems of interest here, 200 nm (1 μ J/pulse) radiation is used as the pump and 243.1 nm radiation (6-7 μ J/pulse) is used to probe the H-atoms eliminated through (2 + 1) REMPI.

The target molecules are *p*-ethylphenol (Aldrich, 4-ethylphenol \geq 99 %), tyramine (Aldrich, \geq 99 %) and L-tyrosine (reagent grade, Aldrich, \geq 98 %), used without any further purification. An Even-Lavie¹⁰ valve was used to introduce *p*-

ethylphenol into vacuum with He as seeding gas at 70 °C. The tyramine solid powder was packed in a quartz cell and fitted inside the cartridge of the valve and heated to 165 °C. Tyrosine was pasted inside a borosilicate cell, which was mounted directly in front of the nozzle of this valve and heated to 250 °C to vaporize it and introduce into vacuum (see chapter 2 for details). After combining both pump and probe pulses collinearly, these are then sent into the interaction region of VMI setup intercepting a molecular beam of sample of interest. The delay between pump and pulses is varied over 3 ps in a step size of 0.025 ps. By changing the delay between pump and probe, 2D images of H^+ are obtained at each delay by following the procedure¹¹ described in chapter 2 and the kinetic energy spectrum at each delay is obtained by deconvolution of the raw images with the help of polar onion peeling (POP)¹² program.

6.3. Time-of-flight Mass Spectrum of Tyramine and p-Ethylphenol

Figure 6.2(a) and (b) presents two-colour time-of-flight mass-spectra (TOF-MS) of tyramine and p-ethylphenol following excitation at 200 nm and probing at 243.1 nm at a pump-probe delay of 2 ps, respectively. In figure 6.2(a) a strong peak at $m/z = 137$ can be observed that corresponds to parent tyramine⁺ in addition to two strong peaks at $m/z = 30, 107$ corresponding to $NH_2CH_2^+$, $CH_2C_6H_4OH^+$ fragments, respectively. These fragment channels have been seen by Tseng et al.⁹, following

excitation at 248 nm but at this excitation energy, the H-atom fragment was not observed.

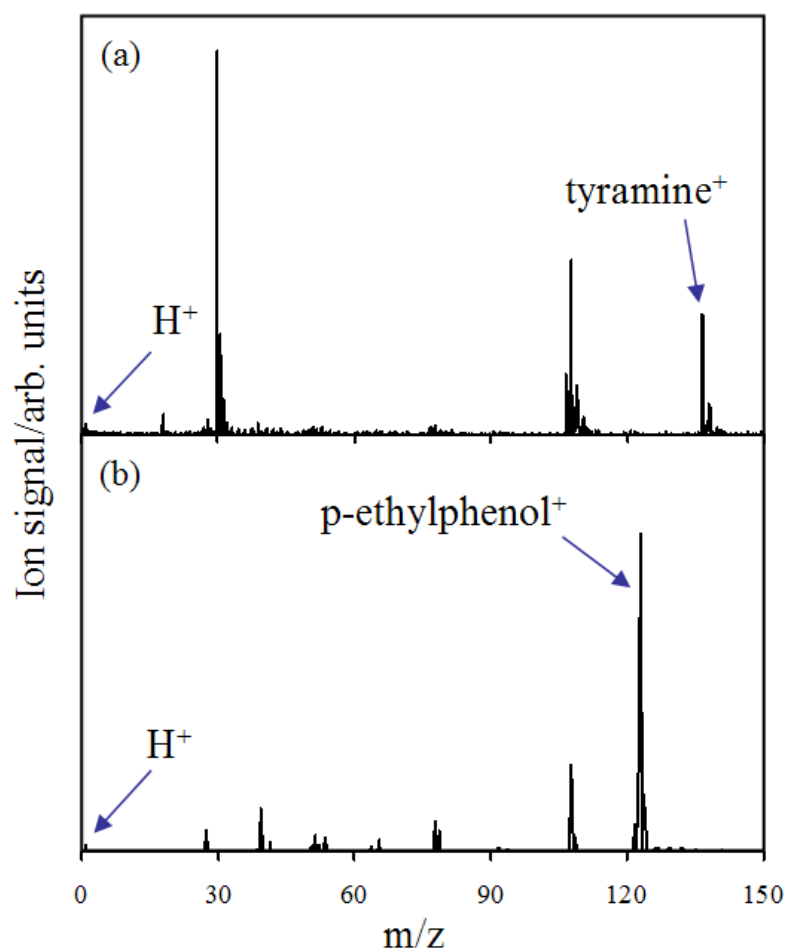


Figure 6.2 Two-colour TOF-MS of (a) tyramine and (b) p-ethylphenol at a pump (200 nm)-probe (243.1 nm) delay of 2 ps.

Following pump excitation i.e. at 200 nm alone the overall signal intensity is very small and has not been shown, but excitation at 200 nm and probing at 243.1 nm, the TOF-MS reveals a peak at $m/z = 1$, as depicted in figure 6.2(a). The low intensity of H^+ signal can be attributed to the poor efficiency to ionize through a narrow atomic line (2s) with a spectrally broad laser pulse in addition to the fact that this is indeed a multiphoton excitation process ((2 + 1) REMPI). The relative signal intensity of H^+

following photodissociation of p-ethylphenol, tyramine and tyrosine will be discussed in proceeding paragraphs. Figure 6.2(b) gives the TOF-MS spectrum of p-ethylphenol, in which a strong peak at $m/z = 122$ is observed that corresponds to parent p-ethylphenol⁺ signal. It also reveals a peak at $m/z = 1$ that corresponds to H⁺. In all these measurements the intensity of 200 nm is kept at a minimum to avoid alternative sources of H-atoms or in generating H⁺ directly. It is also important to highlight here that when only pump (200 nm) was used for excitation/ ionization the signal intensity was very small and is therefore not shown.

6.4. Time-of-flight Mass Spectrum of Tyrosine

Figure 6.3(a) shows the two-colour TOF-MS of tyrosine. This spectrum has been collected at a pump (200 nm)-probe (243.1 nm) delay of 2 ps. The spectrum clearly reveals a peak at $m/z = 181$ that corresponds to the parent tyrosine⁺ signal. The spectrum also shows a peak at $m/z = 1$ corresponding to H⁺, in addition to a very strong peak at $m/z = 107$ that corresponds to the CH₂C₆H₄OH⁺ fragment, which has also been observed in the subunits of tyrosine i.e. tyramine and p-ethylphenol (as shown in figure 6.2(a), (b)), respectively. Ultrafast time-resolved laser spectroscopy coupled with TOF-MS reveals that these H⁺ ions originate from neutral H-atoms that are eliminated from the parent tyrosine molecule driven through the $^1\pi\sigma^*$ state and is confirmed by figure 6.3(b), further details of which will be given in proceeding paragraphs. This figure gives the H⁺ transient as a function of wavelength. As it is clear when the probe wavelength is detuned from the resonance of $2s \leftarrow 1s$ (243.1 nm) transition, a sudden drop in the signal is observed. It is also important to note

that the signal does not go to zero because the probe-alone generates most likely H^+ ions through dissociative ionization.

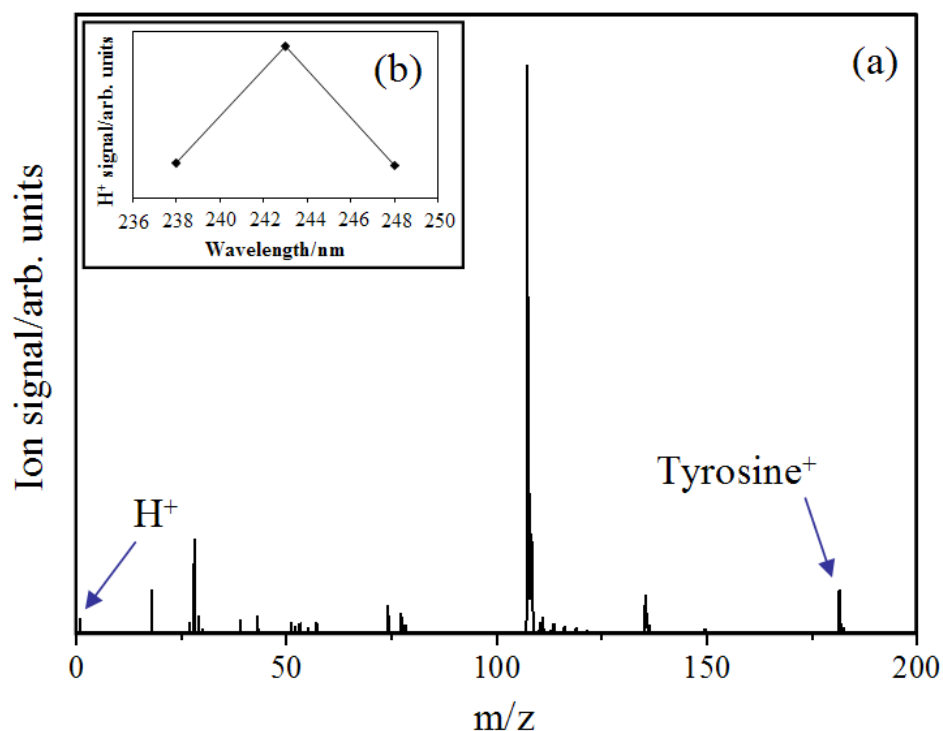


Figure 6.3 (a) Two-colour TOF-MS of tyrosine at a pump (200 nm)-probe (243.1 nm) delay of 2 ps, (b) REMPI of H-atom as a function of wavelength. As the wavelength is tuned on resonance with the $2s \leftarrow 1s$ transition ($\lambda = 243.1$ nm) a sudden rise in the H^+ signal is observed as expected.

6.5. Raw Images and Kinetic Energy Spectrum of H-atoms

Raw images of H^+ and their respective kinetic energy spectra following excitation at 200 nm of p-ethylphenol, tyramine and tyrosine are presented in figures 6.4(a), (b) and (c), respectively. The double headed bold arrow represents the laser

polarization and is parallel to the plane of the detector. Each image and hence kinetic energy spectrum is taken by setting the pump-probe delay at 2 ps.

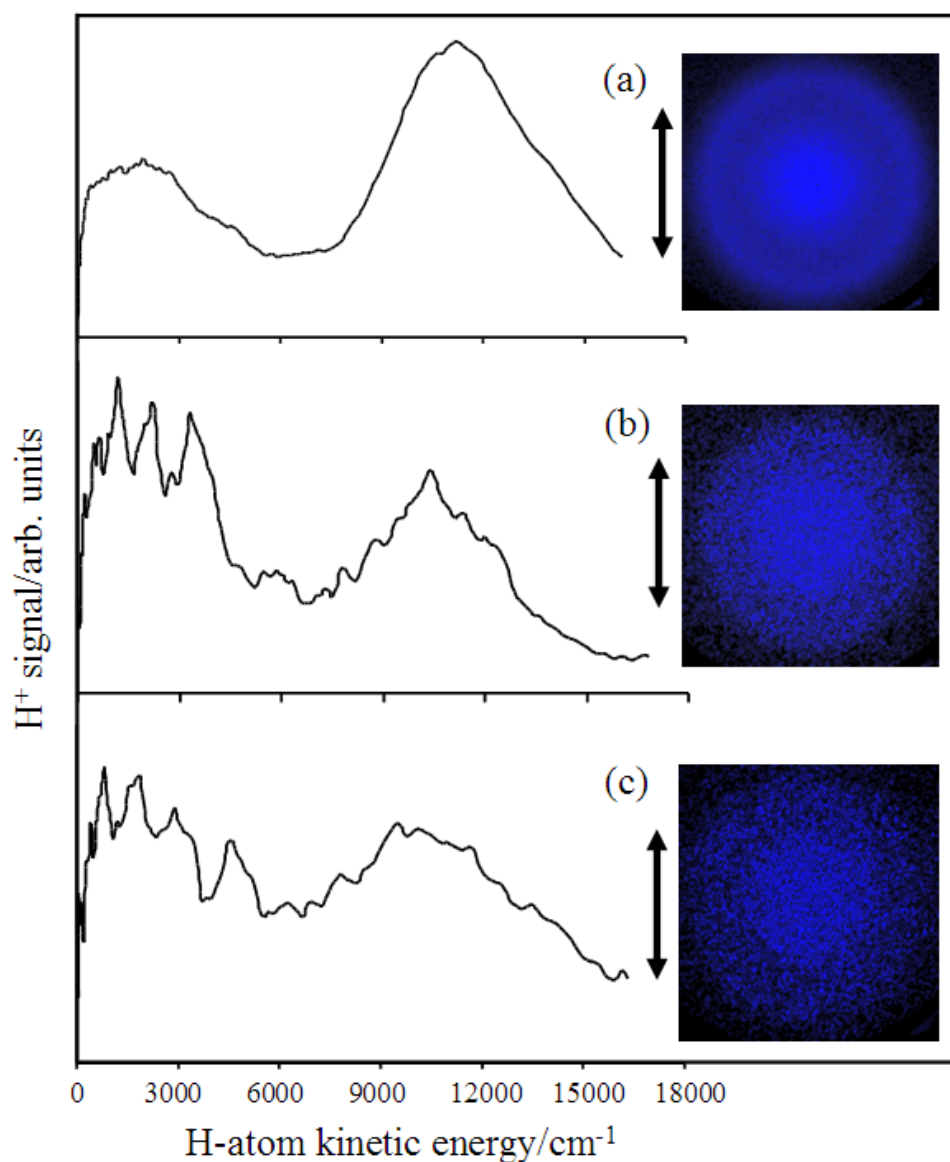


Figure 6.4 Raw H^+ images (right) and deconvoluted H^+ signal as a function of H -atom kinetic energy (left) after $O-H$ bond photolysis of (a) p -ethylphenol, (b) tyramine and (c) tyrosine. Each image and hence the corresponding kinetic energy spectrum is collected by setting the probe (243.1 nm) delay at 2 ps with respect to the pump (200 nm). For further details please see text.

The H^+ images following excitation of p-ethylphenol and tyramine were obtained in approximately 10 minutes by summing 60 individual images, the exposure time set on the CCD camera for each image was approximately 10 s (seconds). While the H^+ image following excitation of tyrosine is collected in approximately 28 minutes by summing 25 individual images; in these measurements the exposure time for each image was approximately 65 s. Owing to the different approaches used to bring these molecules into the vacuum (as described in section 6.2 and also in chapter 2) it is very hard to quantify and compare the H^+ signal intensity for all three compounds. The reason for the adoption of different methods of production of molecular beams of tyramine and tyrosine is the fragile nature of these compounds as they decompose in vacuum by heating. However, very qualitatively it can be said that the H^+ signal intensity reduces in the order p-ethylphenol > tyramine > tyrosine.

6.5.1. Timescales of H-atom Elimination from p-Ethylphenol

Figure 6.5 shows the H^+ transient as a function of pump (200 nm)-probe (243.1 nm) delay (t) in p-ethylphenol for the low (a) and high (b) kinetic energy features, respectively. H^+ transient signals are obtained by collecting a series of kinetic energy spectra at various pump-probe delays and integrating each kinetic energy spectrum at both the low and high kinetic energy features for p-ethylphenol. The integral widths are $\sim 1000\text{ cm}^{-1}$ at the centre of each kinetic energy peak. As one can see from this figure, the two-colour H^+ transient signal at $t < 0$ is minimal. However, at delays corresponding to $t > 0$, the H^+ signal rises sharply indicating fast

O-H bond dissociation is operative. The H^+ signal plateaus at 500 fs in the case of the high kinetic energy component as depicted by figure 6.5(b) and it plateaus at 800 fs for the low kinetic energy component as presented by figure 6.5(a).

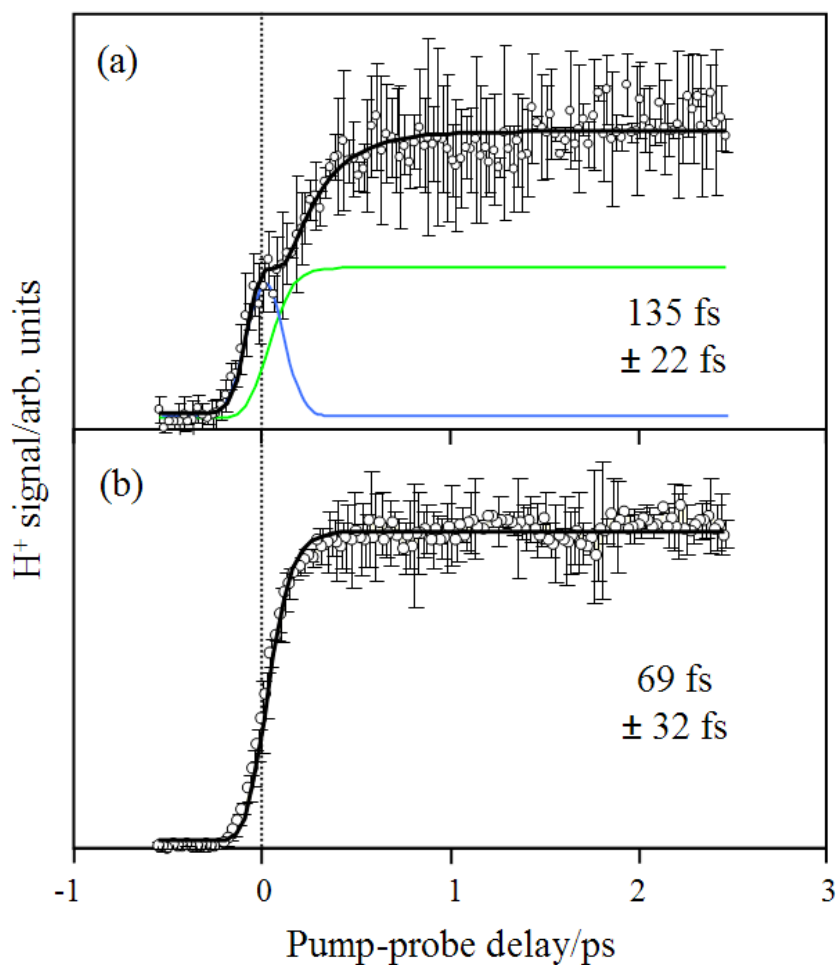


Figure 6.5 H^+ transient as a function of pump (200 nm)-probe (243.1 nm) delay for the low kinetic energy feature (a) and high kinetic energy (b) for *p*-ethylphenol. The error bars correspond to two standard deviation of the mean representing a 95 % confidence limit.

As it can be seen in figure 6.5(a) there is a small hump near time zero. This indicates some multiphoton effects that are contributing to H^+ transient at low kinetic energies. The H^+ transient data at low kinetic energies can not be fitted with a single step

function; rather it is fitted by addition of a step function and an exponential decay function, the step function is obtained by convolution of the instrument response function i.e., a Gaussian function of 160 fs FWHM and an exponential function. In figure 6.5(a), the blue trace represents the decay function, green trace represents a step function (scaled for clarity) and solid black trace is the combination of both and is the best fit to the experimental data (black circles) suggesting a time constant of O-H bond dissociation of $135 \text{ fs} \pm 22 \text{ fs}$ for low kinetic energy H-atoms. The high kinetic energy data can be fitted with only a step function and the black trace in figure 6.5(b) suggests that the high kinetic energy H-atoms appear with a time constant of $69 \text{ fs} \pm 32 \text{ fs}$.

6.5.2. Timescales of H-atom Elimination from Tyramine

Figure 6.6(a) and (b) gives the H^+ transient as a function of pump (200 nm)-probe (243.1 nm) delay (t) of tyramine for the low and high kinetic energy features, respectively. As in p-ethylphenol, the H^+ transient signals are also obtained by collecting a series of kinetic energy spectra at various pump-probe delays and integrating each kinetic energy spectrum at both the low and high kinetic energy features for tyramine. The integral widths are again $\sim 1000 \text{ cm}^{-1}$ at the centre of each kinetic energy peak. The H^+ signal intensity at $t < 0$ is once again minimal, but at delays corresponding to $t > 0$, the H^+ signal rises sharply. The H^+ signal plateaus at 500 fs in the case of the high kinetic energy components as shown by figures 6.6(b) and plateaus at 800 fs for the low kinetic energy component as seen in figure 6.6(a). Again in figure 6.6(a) multiphoton effects can be seen near time zero, as was seen in

p-ethylphenol. The H^+ transient is fitted with the models as described for p-ethylphenol and suggest O-H bond fission in tyramine occurs in $202 \text{ fs} \pm 22 \text{ fs}$ (solid black line, figure 6.6(a)) and $65 \text{ fs} \pm 22 \text{ fs}$ (solid black line, figure 6.6(b)) for the low and high kinetic energy features, respectively. The error bars correspond to two standard deviations of the mean representing a 95 % confidence limit.

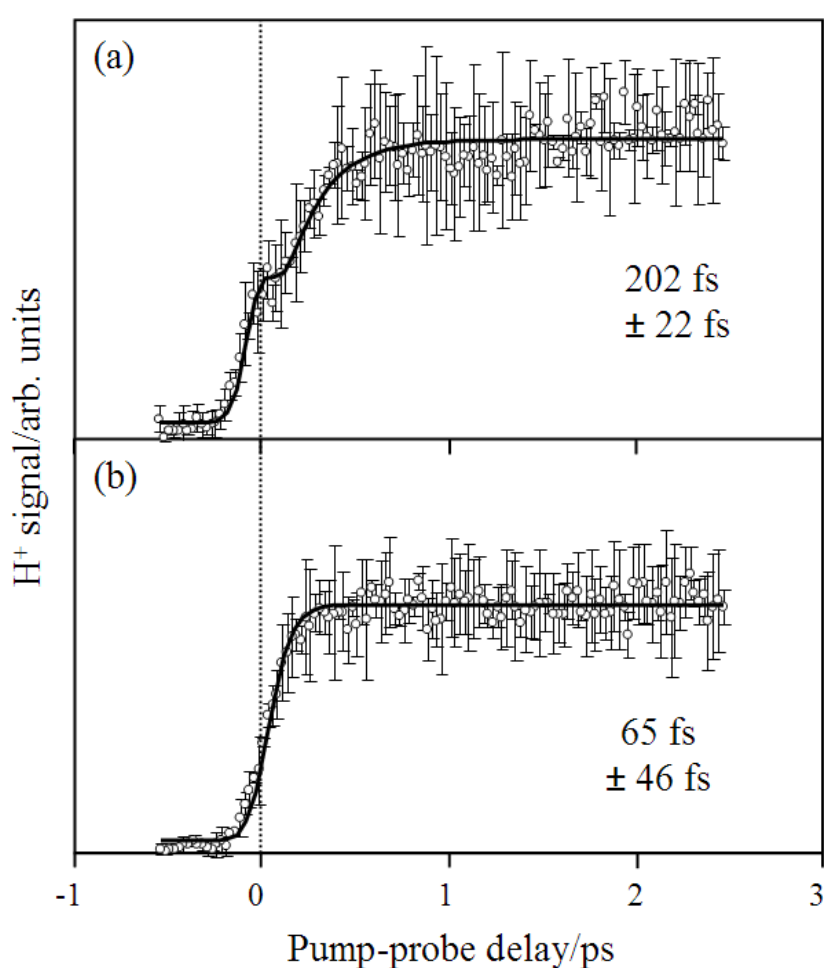


Figure 6.6 H^+ transient as a function of pump (200 nm)-probe (243.1 nm) delay for the low kinetic energy feature (a) and high kinetic energy (b) for tyramine.

6.5.3. Timescales of H-atom Elimination from Tyrosine

Figure 6.7(a) (and 6.4(c)) reports the first evidence of H-atom elimination driven through the repulsive $^1\pi\sigma^*$ state of the O-H coordinate in tyrosine in the gas-phase. The H^+ signal as a function of H-atom kinetic energy at pump (200 nm)-probe (243.1 nm) delays of 2 ps, 1 ps and at time zero, black, pink and red respectively is shown in figure 6.7(a). The two-colour H^+ signal at a delay of -1 ps, that is, when the probe precedes the pump, is very small and therefore not shown. It is immediately apparent from 6.7(a) that the H-atom kinetic energy spectra at delays of 2 ps and 1 ps pump-probe delay are almost identical, the ramifications of which are described below. The overall features of the H-atom kinetic energy spectra look very similar to those of p-ethylphenol, tyramine and unsubstituted phenol (as shown by figure 4.2 in chapter 4), thus strongly suggesting that the H-atom elimination is very likely occur by dissociation of O-H mediated by the $^1\pi\sigma^*$ state in the chromophore. The data were obtained with the help of an oven that was purposely designed to prevent tyrosine from decomposing when heated and brought to vacuum and provided sufficient sample densities of tyrosine for data collection up to 4 hours (see chapter 2 for details). Given that both the low and high kinetic energies features have already emerged by 1 ps and plateau, as evidenced by the similarities of the two spectra at 1 ps and 2 ps, and given the similarities of these spectra to those collected in p-ethylphenol and tyramine, it is very likely that H-atom elimination in tyrosine is also occurring on an ultrafast timescale. The O-H bond dissociation appears to be extremely fast in tyrosine and this idea is further strengthened by figure 6.7(b) which presents the parent tyrosine ion signal as a function of pump (200 nm)-probe (243.1

nm) delay. From this figure, it is evident that the parent transient is extremely short-lived, rising sharply at time zero and decaying in < 200 fs for both positive and negative pump-probe delays. The short-lived transient presumably decays through a number of routes, one of which is via the $^1\pi\sigma^*$ state leading to a kinetic energy profile similar to that of the chromophore. Unfortunately, reliable time constants can not be extracted for this process as in both cases (positive and negative time-delays) these timescales appear to be much faster than the instrument response function.

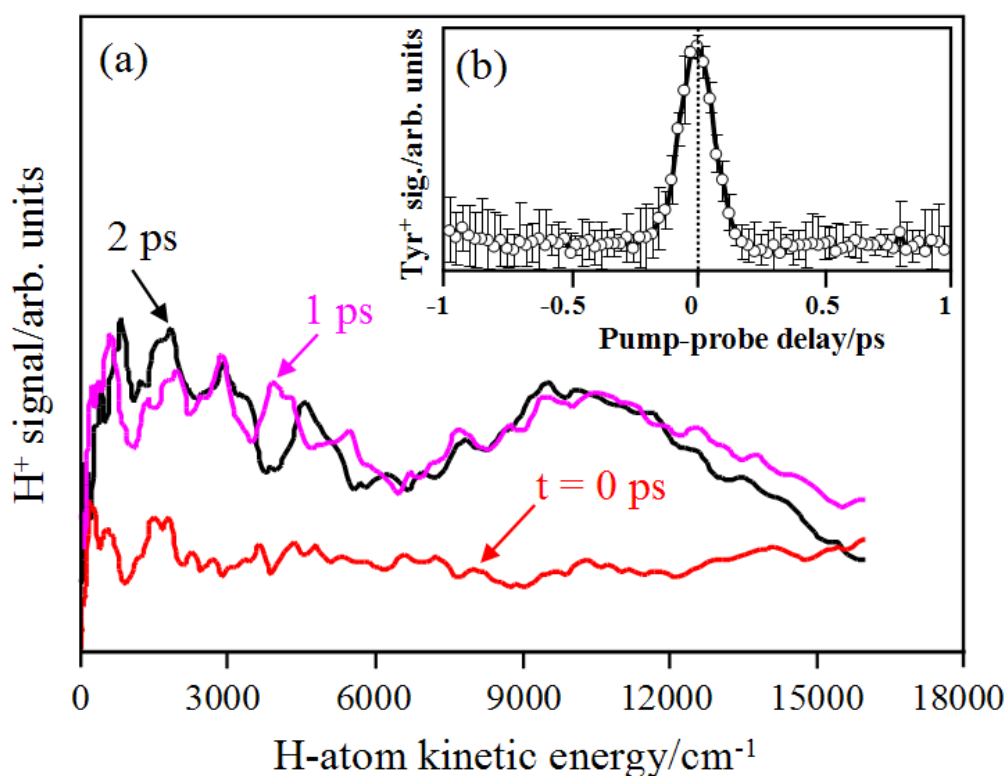


Figure 6.7 H^+ transient as a function of H -atom kinetic energy. The black, pink and red lines represent the kinetic energy of H -atoms at pump (200 nm)-probe (243.1 nm) delays of 2, 1 and 0 ps, respectively, (b) parent tyrosine ion signal as a function of pump (200 nm)-probe (243.1 nm) delay.

6.5.3.1. Discussion

In figure 6.4 all the three H⁺ images collected after photodissociation of p-ethylphenol, tyramine and tyrosine look qualitatively similar with an intense central region and a sharp outer part. The outer ring of all the three images is a result of ionization of energetic H-atoms that are eliminated directly through the $^1\pi\pi^*/^1\pi\sigma^*$ and $S_0/^1\pi\sigma^*$ CIs due to the repulsive character of $^1\pi\sigma^*$ state.^{13,14} The inner part of the image can be attributed to H-atoms that are generated as result of statistical unimolecular decay, multiphoton effects or due to the H-atoms whose partner fragment is left in the first electronically excited state.¹³⁻¹⁵ Another interesting feature displayed by all the images is the isotropic distribution of all the recoiling H-atom fragments. This peculiar behavior is in contrast to the unsubstituted phenol¹³ but agrees with the TKER measurements made in the substituted phenols by Ashfold et al.¹⁵

Whilst the anisotropy is lacking in these images, the kinetic energy spectrum displayed by H-atoms eliminated from p-ethylphenol, tyramine and tyrosine also presented in figure 6.4 agrees well with the previous measurements in phenol and show a bimodal distribution.¹³⁻¹⁵ The high kinetic energy peak in figure 6.4(a), (b) and (c) peaks at $\sim 11300\text{ cm}^{-1}$, 10500 cm^{-1} and 10200 cm^{-1} for p-ethylphenol, tyramine and tyrosine respectively, and is a clear manifestation of dissociation through the repulsive $^1\pi\sigma^*$ state.^{7-9,13-15} In unsubstituted phenol, as discussed in chapter 4 figure 4.2, the high kinetic energy feature peaks at 11600 cm^{-1} . The maxima of the peak heights at high kinetic energies in these systems seem to be setting a trend. The kinetic energy released by H-atoms at the high kinetic energy

feature decreases in the order p-ethylphenol < tyramine < tyrosine. This may be due to the slight shifts in electronic states along the O-H coordinate either of the parent molecules or the electronic states of the partner fragments.

The low kinetic energy feature peaks at 1800 cm^{-1} for p-ethylphenol and at 2000 cm^{-1} for both tyramine and tyrosine, this slight shift in kinetic energy in H-atoms at low kinetic energies again may be attributed to the shift in energy of participating states. However these arguments remain speculative until high level calculations relating to electronic structure of these systems are carried out. In addition, the intensity of the high kinetic energy feature of the H-atoms decreases while the low kinetic energy feature increases when moving from p-ethylphenol to tyrosine and this can be attributed to multiphoton effects that most likely increase with molecular complexity. It is important to note once again that detuning the probe wavelength from the H-atom $2s \leftarrow 1s$ resonance results in a considerable reduction of the H^+ signal, a clear indication that H-atoms are probed and this effect has been observed in all the three systems studied.

The results once again point to two distinct pathways of H-atom elimination from p-ethylphenol and tyramine being operative. The fast component can be fitted with a single step function suggesting a time constant of ~ 70 fs for O-H bond dissociation in both p-ethylphenol and tyramine. These findings strongly implicate direct dissociation mediated by the $^1\pi\sigma^*$ state through the $^1\pi\pi^*/^1\pi\sigma^*$ and $\text{S}_0/^1\pi\sigma^*$ CIs and agrees with previous findings in unsubstituted phenol reported in chapter 3 and 4 and also to the timescales of O-H bond cleavage proposed by Lan et al.⁵ in which they showed that the population and depopulation dynamics of the $^1\pi\sigma^*$ state in phenol occur within tens of femtoseconds (fs).

Another interesting feature can be seen in the H^+ transient of the low kinetic energy component that has not been observed in unsubstituted phenol and is the sudden rise in the signal in the vicinity of time zero ($t = 0$), as displayed in figures 6.5(a) and 6.6(a) for p-ethylphenol and tyramine, respectively. These H-atoms are most likely due to multiphoton processes which have recently been observed in other systems of comparable electronic structure.¹⁶ As mentioned above, in order to fit the low kinetic energy H^+ transient, a decay function with $t < 50$ fs *and* a step function is used, which suggest a time constant for H-atom elimination at these low kinetic energies of $135 \text{ fs} \pm 22 \text{ fs}$ and $202 \text{ fs} \pm 22 \text{ fs}$ for p-ethylphenol and tyramine, respectively.

This indicates that the low kinetic energy H-atoms are also appearing on an ultrafast timescale which seems to suggest the dissociation may be occurring adiabatically resulting in partner fragments in their first electronically excited state,^{14,17} rather than indirect dissociation involving internal conversion to the ground state followed by statistical unimolecular decay.⁹ Assuming this model is correct, the slower time constant for the low kinetic energy component measured in tyramine suggests that the velocity of the wavepacket following adiabatic dissociation is slower than in the p-ethylphenol counterpart. This may be attributed to a higher energy of the tyramine fragment (minus H). However until dynamics calculations are carried out on this system, this argument remains speculative.

6.6. Epilogue

The work described above for p-ethylphenol clearly shows that ultrafast H-atom elimination occurs following dissociation of the O-H bond after excitation at 200 nm. The dynamics of the H^+ transient in tyramine and the kinetic energy features of the H-atom spectra in tyrosine also demonstrate that following excitation at 200 nm, the H-atom elimination is occurring through the same coordinate i.e. O-H bond as exhibited by the chromophore phenol, thus confirming the active participation of $^1\pi\sigma^*$ states from the chromophore of the amino acid all the way to the amino acid itself.

The kinetic energy spectra of tyrosine at different time delays and the ultrafast decay dynamics of the parent tyrosine ion signal transient seem to suggest that O-H bond dissociation occurs on an ultrafast timescale, as in phenol. Currently, attempts are ongoing to develop an oven source that will deliver larger number densities of tyrosine into vacuum for longer periods of time (up to 12 hours) in order to be able to carry out time resolved VMI studies of H-atom elimination in this molecule.

In future, it would be interesting to address the photochemistry of tryptophan. However, from the work reported in chapter 5 on the chromophore of tryptophan, indole, where the participation of the $^1\pi\sigma^*$ state has been implicated and from the results of tyrosine and its sub-units reported in this chapter, it would be anticipated there is a high probability that the $^1\pi\sigma^*$ is likely to be a key player in tryptophan's photochemistry.

6.7. References

- (1) Creed, D. *Photochem. Photobiol.* **1984**, *39*, 563.
- (2) Crespo-Hernández, C. E.; Cohen, B.; Hare, P. M.; Kohler, B. *Chem. Rev.* **2004**, *104*, 1977.
- (3) Saigusa, H. *J. Photochem. Photobiol. C* **2006**, *7*, 197.
- (4) Sobolewski, A. L.; Domcke, W.; Dedonder-Lardeux, C.; Jouvet, C. *Phys. Chem. Chem. Phys.* **2002**, *4*, 1093.
- (5) Lan, Z.; Domcke, W.; Vallet, V.; Sobolewski, A. L.; Mahapatra, S. *J. Chem. Phys.* **2005**, *122*, 224315.
- (6) Abe, M.; Ohtsuki, Y.; Fujimura, Y.; Lan, Z.; Domcke, W. *J. Chem. Phys.* **2006**, *124*, 224316.
- (7) Tseng, C.-M.; Lee, Y. T.; Ni, C.-K. *J. Chem. Phys.* **2004**, *121*, 2459.
- (8) Tseng, C.-M.; Lee, Y. T.; Lin, M.-F.; Ni, C.-K.; Liu, S.-Y.; Lee, Y.-P.; Xu, Z. F.; Lin, M. C. *J. Phys. Chem. A* **2007**, *111*, 9463.
- (9) Tseng, C.-M.; Lee, Y.-T.; Ni, C.-K.; Chang, J.-L. *J. Phys. Chem. A* **2007**, *111*, 6674.
- (10) Even, U.; Jortner, J.; Noy, D.; Lavie, N.; Cossart-Magos, C. *J. Chem. Phys.* **2000**, *112*, 8068.
- (11) Eppink, A. T. J. B.; Parker, D. H. *Rev. Sci. Instrum.* **1997**, *68*, 3477.
- (12) Roberts, G. M.; Nixon, J. L.; Lecointre, J.; Wrede, E.; Verlet, J. R. R. *Rev. Sci. Instrum.* **2009**, *80*, 053104.
- (13) Hause, M. L.; Yoon, Y. H.; Case, A. S.; Crim, F. F. *J. Chem. Phys.* **2008**, *128*, 104307.

(14) Iqbal, A.; Cheung, M. S. Y.; Nix, M. G. D.; Stavros, V. G. *J. Phys. Chem. A* **2009**, *113*, 8157.

(15) Ashfold, M. N. R.; Devine, A. L.; Dixon, R. N.; King, G. A.; Nix, M. G. D.; Oliver, T. A. A. *PNAS* **2008**, *105*, 12701.

(16) Wells, K. L.; Hadden, D. J.; Nix, M. G. D.; Stavros, V. G. *J. Phys. Chem. Lett.* **2010**, *1*, 993.

(17) King, G. A.; Oliver, T. A. A.; Nix, M. G. D.; Ashfold, M. N. R. *J. Phys. Chem. A* **2009**, *113*, 7984.

Chapter 7

Conclusions

This thesis presented timescales of H-atom elimination of photoexcited phenol and indole molecules, the chromophores of the amino acids tyrosine and tryptophan, respectively. This has been achieved with the aid of ultrafast time-resolved spectroscopy, TOF-MS and VMI techniques. Time-resolved spectroscopy coupled with VMI enabled us to establish time-constants for the H-atoms eliminated through various channels. The experiments were then extended to tyrosine and its sub-units p-ethylphenol and tyramine in which, for the first time, time-constants for H-atom elimination revealed that this process occurred through the same channels as exhibited by the chromophore (phenol) i.e. O-H coordinate.

Chapter 1 described a brief history of reaction dynamics and how lasers can control, drive and monitor reactions following photoexcitation of gas phase molecules prepared in molecular beams. Chapter 2 dealt with the experimental methods i.e. generation of pump-probe pulses coupled with molecular beams generated with the aid of an Even-Lavie pulsed valve. This chapter also described the modifications to the valve that were necessary in order to generate molecular beams of tyramine and tyrosine molecules that are known to decompose upon heating. Chapter 2 ended with a description of the data acquisition and data analysis software used.

In chapter 3, a combination of femtosecond time-resolved spectroscopy and TOF-MS, in phenol following excitation at 200 nm and probing of the H-atoms via (2 + 1) REMPI at 243.1 nm showed that H-atom elimination along the dissociative $^1\pi\sigma^*$ state occurred within $103 \text{ fs} \pm 30 \text{ fs}$, indicating efficient coupling of the S_2 , S_1 and S_0 PESs mediated by the S_1/S_2 and S_0/S_2 CIs. This observation was consistent with the fast H-atoms observed in recent TKER measurements. Within the time window of these measurements however, there was no indication of a second pathway to H-atom elimination, as that observed in comparative time-resolved measurements made in pyrrole. This suggested that the slower H-atoms observed in the multimass ion imaging and TKER measurements are likely to occur on a much longer timescale ($> 200 \text{ ps}$). By monitoring the parent phenol ion (Ph^+) signal, the excited state dynamics of phenol indicated that the lifetime on the S_1 ($^1\pi\pi^*$) strongly depended upon the precise excitation energy on this PES, providing conflicting conclusions as to the location of the S_1/S_2 CI.

In chapter 4, using a combination of femtosecond pump-probe spectroscopy and VMI, this enabled to clock the real-time dissociation of the O-H bond in phenol- d_5 , occurring through various pathways, following excitation above the S_1/S_2 CI with 200 nm radiation. The extra dimension afforded by VMI helped to separate H-atoms with various amounts of kinetic energy. From these measurements, it was inferred that H-atoms with high kinetic energies formed with a time-constant of $88 \text{ fs} \pm 30 \text{ fs}$, indicating a direct decay route involving passage through or around three successive CIs (S_3/S_2 , S_1/S_2 and S_0/S_2) to form $\text{H} + \text{C}_6\text{D}_5\text{O}$ in its electronic ground state. The H-atoms with lower kinetic energy, gave a time-constant of $146 \text{ fs} \pm 25 \text{ fs}$ also suggesting that they were formed via a non-statistical decay route, involving the

same decay pathway, but leading to electronically excited phenoxy-d5 radicals induced by adiabatic dynamics in the region of the final (S_0/S_2) CI. Non-limiting, positive β_2 for low kinetic energy H-atoms brought into question the presence of indirect dynamics, thus ruling out the possibility of these H-atoms being associated with single photon unimolecular decay leading to ground state phenoxy radicals and suggest direct nature of their formation. It was also seen in this chapter that it seemed likely that the low kinetic energy component was multicomponent, comprised of a multiphoton statistical decay, occurring with a much longer time constant (longer than the experiment's time-window), in addition to 'direct channels' leading to excited state products. The combination of time *and* energy resolved VMI with selective deuteration of the aromatic ring made it possible to disentangle these contributions in phenol-d5 and confirmed the direct nature of the low kinetic energy channel in C_6D_5OH photolysis at 200 nm.

In chapter 5, the time-resolved VMI measurements performed on indole showed that ultrafast H-atom elimination also occurred throughout *all* kinetic energy ranges. Both the high *and* low kinetic energy H-atoms are formed with a time-constant of $100 \text{ fs} \pm 30 \text{ fs}$ and $195 \text{ fs} \pm 40 \text{ fs}$, respectively. The former was clearly attributed to dissociation involving the $^1\pi\sigma^*$ state. The latter is still opened to debate. However, this work clearly demonstrated that the low kinetic energy H-atoms observed in these measurements cannot be attributed to an indirect, statistical unimolecular decay pathway. Two explanations were offered for the low kinetic energy H-atoms observed in these measurements, the first based on multiphoton effects and in agreement with TKER measurements whilst the second related to adiabatic dissociation leading to electronically excited indolyl fragment. As in

phenol, the conclusion drawn was that it is very likely that these low kinetic energy H-atoms are multicomponent in nature.

In chapter 6, the work described the extension of the measurements on phenol towards identifying the active participation of the $^1\pi\sigma^*$ state in the photochemistry of the amino acid tyrosine. To achieve this feat, a step-wise approach was taken in which the complexity of the system was gradually increased towards the target molecule. For p-ethylphenol, the measurements showed that ultrafast H-atom elimination occurred following photoexcitation at 200 nm, the kinetic energy spectra obtained showing very similar characteristics to those obtained in phenol and therefore most likely indicative that these H-atoms are due to O-H bond dissociation. The timescales and kinetic energy of the H^+ transient in tyramine also strongly suggested the active participation of the $^1\pi\sigma^*$ state in the photochemistry of this molecule whilst the kinetic energy features of the H-atom spectra in tyrosine also implied that following excitation at 200 nm, the H-atom elimination occurred through the same coordinate i.e. O-H bond as exhibited by its phenol chromophore.

This body of work thus confirmed that in the case of the amino acid tyrosine, photoexcitation of the chromophore leads, in part, to subsequent dynamics at the chromophore site (O-H). This prompts the question of whether or not this observation can be extended to other amino acids (e.g. tryptophan) and di/tri peptides. The work described in this thesis therefore is a stepping stone towards extending these measurements from the micro (chromophore) towards the macro (polypeptides) and it remains to be seen whether or not trends in the electronic structure govern the photochemistry of much larger, realistic systems.